This Page Is Inserted by IFW Operations
and is not a part of the Official Record

BEST AVAILABLE IMAGES

Defective images within this document are accurate representations of the original documents submitted by the applicant.

Defects in the images may include (but are not limited to):

- BLACK BORDERS
- TEXT CUT OFF AT TOP, BOTTOM OR SIDES
- FADED TEXT
- ILLEGIBLE TEXT
- SKEWED/SLANTED IMAGES
- COLORED PHOTOS
- BLACK OR VERY BLACK AND WHITE DARK PHOTOS
- GRAY SCALE DOCUMENTS

IMAGES ARE BEST AVAILABLE COPY.

As rescanning documents *will not* correct images, please do not report the images to the Image Problem Mailbox.

(1) Image

SEMI Specification	SEMI Title	Iron Impurity Limits
C 44-0301	Specification and Guidelines for Sulfuric Acid	0,2 ppm max (Grade 1) 10 ppb max (Grade 2)
C 36-0301	Specification for Phosphoric Acid	2,0 ppm max (Grade 1) 700 ppb max (Grade 2) 100 ppb max (Grade 3)
C 18-0301	Specification for Acetic Acid	0,2 ppm (Grade 1)
C 20-1101	Specification and Guidelines for Ammonium Fluoride	0,2 ppm max (Grade 1)
C27-0301	Specification and Guidelines for Hydrochloric Acid	0,2 ppm max (Grade 1) 10 ppb max (Grade 2)
C28-0301	Specification and Guidelines for Hydrofluoric Acid	0,2 ppm max (Grade 1) 10 ppb max (Grade 2)
C 35-0301	Specification and Guideline for Nitric Acid	0,2 ppm max (Grade 1) 5 ppb max (Grade 2)

Attach 2

ITRS
Front End Process

Table 32a Starting Materials Technology Requirements—Near Term

YEAR / TECHNOLOGY NODE	1999 180 nm	2000	2001	2002 130 nm	2003	2004	2005 100 nm
DRAM ½ Pitch (nm)	180	165	150	130	120	110	100
MPU Gate Length (nm)	140	120	100	85	80	70	65
General Characteristics * [A,B]							
Wafer diameter (mm) **	200	300 ***	300	300	300	300	300
Edge exclusion (mm)	2	1	1	1	1	1	1
Front surface particle size (nm), latex sphere equivalent [C]	≥ 90	≥ 82.5	≥ 75	≥ 65	≥ 60	≥ 55	≥ 50
Particles (cm^{-2}) [D]	≤ 0.13	≤ 0.12	≤ 0.12	≤ 0.14	≤ 0.13	≤ 0.12	≤ 0.10
Particles (#/wf)	≤ 38	≤ 84	≤ 80	≤ 95	≤ 89	≤ 84	≤ 72
Critical surface metals (at/cm^2) [E]	$\leq 1.8\times10^{10}$	$\leq 1.4\times10^{10}$	$\leq 1.2\times10^{10}$	$\leq 8.6\times10^{9}$	$\leq 6.8\times10^{9}$	$\leq 5.8\times10^{9}$	$\leq 4.9\times10^{9}$
Site flatness (nm) [F]	≤ 180	≤ 165	≤ 150	≤ 130	≤ 120	≤ 110	≤ 100
Oxygen (center point value ± 2.0 ppma) (ASTM 79) [G]	19–31	18–31	18–31	18–31	18–31	18–31	18–31
Polished Wafer *							
Total Allowable Front Surface Light Scattering Defect Density is The Sum of Crystal Originated Pits (COPs) and Particles (see General Characteristics)							
Front surface COPs size (nm), latex sphere equivalent [C]	≥ 90	≥ 82.5	≥ 75	≥ 65	≥ 60	≥ 55	≥ 50
COPs (cm^{-2}) [H]	≤ 0.13	≤ 0.12	≤ 0.12	≤ 0.14	≤ 0.13	≤ 0.12	≤ 0.10
COPs (#/wf)	≤ 38	≤ 84	≤ 80	≤ 95	≤ 89	≤ 84	≤ 72
Back surface particle size (DRAM), latex sphere equivalent (nm) [I]	≥ 667	≥ 617	≥ 567	≥ 500	≥ 467	≥ 433	≥ 400
Particles (DRAM) (#/cm^2) [J]	≤ 0.63	≤ 0.61	≤ 0.58	≤ 0.55	≤ 0.53	≤ 0.50	≤ 0.48
Particles (DRAM) (#/wf)	≤ 191	≤ 423	≤ 403	≤ 384	≤ 367	≤ 352	≤ 336
Total bulk Fe (at/cm^3) [K]	$\leq 1\times10^{10}$	$<1\times10^{10}$	$<1\times10^{10}$	$<1\times10^{10}$	$<1\times10^{10}$	$<1\times10^{10}$	$<1\times10^{10}$
Oxidation stacking faults (OSF) (DRAM) (cm^{-2}) [L]	≤ 4.4	≤ 3.9	≤ 3.4	≤ 2.8	≤ 2.5	≤ 2.2	≤ 1.9
Oxidation stacking faults (OSF) (MPU) (cm^{-2}) [L]	≤ 3.1	≤ 2.5	≤ 1.9	≤ 1.5	≤ 1.4	≤ 1.1	≤ 1.0
Recombination lifetime (µs) [M], see also [N]	≥ 305	≥ 350	≥ 350	≥ 350	≥ 350	≥ 350	≥ 350

Solutions Exist *Solutions Being Pursued* *No Known Solutions*

Metrology

Table 82a Metrology Technology Requirements—Near Term

YEAR / TECHNOLOGY NODE	1999 180 nm	2000	2001	2002 130 nm	2003	2004	2005 100 nm
DRAM ½ Pitch	180	165	150	130	120	110	100
MPU Gate Length	140	120	100	85	80	70	65
Microscopy							
Inline, nondestructive microscopy resolution (nm) for P/T=0.1	1.4	1.2	1.0	0.85	0.8	0.7	0.65
Maximum aspect ratio / diameter (nm) (DRAM contacts) [A]	6.3 200	6.7 175	7.1 160	7.5 140	8.0 130	8.5 120	9 110
Materials and Contamination Characterization							
Real particle detection limit (nm) [B]	90	82	75	65	60	55	50
Minimum particle size for compositional analysis (on dense lines) (nm)	48	40	33	28	27	23	22
Specification limit of total surface contamination Ca, Co, Cu, Cr, Fe, K, Mo, Mn, Na, Ni (atoms/cm^2)	$\leq 9\times10^{9}$	$\leq 7\times10^{9}$	$\leq 6\times10^{9}$	$\leq 4.4\times10^{9}$	$\leq 3.4\times10^{9}$	$\leq 2.9\times10^{9}$	$\leq 2.5\times10^{9}$
Surface detection limits for individual elements Ca, Co, Cu, Cr, Fe, K, Mo, Nm, Na, Ni (atoms/cm^2) with signal to noise of 3:1 for each element	$\leq 9\times10^{8}$	$\leq 7\times10^{8}$	$\leq 6\times10^{8}$	$\leq 4.4\times10^{8}$	$\leq 3.4\times10^{8}$	$\leq 2.9\times10^{8}$	$\leq 2.5\times10^{8}$

Anlage 2

Defect Reduction

Table 80a Defect Prevention and Elimination Technology Requirements—Near Term

YEAR / *TECHNOLOGY NODE*	*1999* *180 nm*	*2000*	*2001*	*2002* *130 nm*	*2003*	*2004*	*2005* *100 nm*
Water Environment Control							
Critical particle size (nm) [A]	90	90	75	65	60	55	50
Particles ³ critical size ($/m^3$) [B]	12	10	8	5	4	3	2
Airborne Molecular Contaminants (ppbM) [C]							
Lithography—Bases (as amine, amide, or NH_4)	1000	1000	1000	750	750	750	750
Gate—Metals (as Cu, $E=2 \times 10^{10}$) [C]	0.3	0.3	0.25	0.2	0.2	0.15	0.1
Gate—Organics (as molecular weight greater than or equal to 250, $E=1 \times 10^{-3}$) [D]	200	170	130	100	90	80	70
—Organics(as CH_2)	3600	3000	2400	1800	1620	1440	1260
Salicidation contact—acids (as Cl-, $E=1 \times 10^{-3}$)	10	10	10	10	10	10	10
Salicidation contact—bases (as NH_3, $E=1 \times 10^{-5}$)	40	32	24	20	16	12	10
Dopants (P or B) [F]	< 10	< 10	< 10	< 10	< 10	< 10	< 10
Process Critical Materials							
Critical particle size (nm) [B]	90	90	75	65	60	55	50
Ultrapure Water							
Total oxidizable carbon (ppb)	2	2	2	1	1	< 1	< 1
Bacteria (CFU/ liter)	< 1	< 1	< 1	< 1	< 1	< 1	< 1
Total Silica (ppb)	0.1	0.1	0.05	0.05	0.05	0.05	0.05
Dissolved oxygen (ppb)	10	7	3	1	1	1	1
Particles ³ critical size (/ml)	< 0.2	< 0.2	< 0.2	< 0.2	< 0.2	< 0.2	< 0.2
Critical cation, anion, metals (ppt, each)	20	20	< 20	< 20	< 20	< 20	10
Liquid Chemicals [E]							
Particles ³ critical size (/ml)	< 0.5	< 0.5	< 0.5	< 0.5	< 0.5	< 0.5	< 0.5
HF-, H_2O_2, NH_4OH: Fe, Cu (ppt, each)	< 250	< 220	< 180	< 150	<135	< 110	< 100
Critical cation, anion, metals (ppt, each)	< 20	< 20	< 20	< 10	< 10	< 10	< 5
HF-only TOC (ppb)	< 60	< 50	< 40	< 30	< 30	< 25	< 20
HCl, H_2SO_4: All impurities (ppt)	< 1000	< 1000	< 1000	< 1000	< 1000	< 1000	< 1000
BEOL Solvents, Strippers K, Li, Na (ppt, each)	< 1000	< 1000	< 1000	< 1000	< 1000	< 1000	< 1000
Bulk Ambient Gases							
N_2,O_2,Ar,H_2; H_2O,O_2,CO_2,CH_4 (ppt, each)	<1000	< 1000	< 1000	< 1000	< 1000	< 1000	< 1000
Particles > critical size (liter)	< 0.1	< 0.1	< 0.1	< 0.1	< 0.1	< 0.1	< 0.1
Specialty Gases							
POU Particles ³ critical size (/liter) [D]	2	2	2	2	2	2	2
Corrosives—metal etchants							
O_2 (ppbv)	< 500	< 500	< 500	< 500	< 500	< 500	< 200
H_2O (ppbv)	< 500	< 500	< 500	< 500	< 500	< 500	< 200
Inerts—Oxide/PR Etchants/Strippers							
O_2 (ppbv)	< 1000	< 1000	< 1000	< 1000	< 1000	< 1000	< 500
H_2O (ppbv)	< 1000	< 1000	< 1000	< 1000	< 1000	< 1000	< 500
Total metallics (pptwt)	< 500	< 500	< 500	< 500	< 500	< 500	< 500

Solutions Exist *Solutions Being Pursued* *No Known Solutions*

Anlage 1

(2)

Jpn. J. Appl. Phys. Vol. 40 (2001) pp. L915–L917
Part 2, No. 9A/B, 15 September 2001
©2001 The Japan Society of Applied Physics

Latent Iron in Silicon

Byoung-Deog CHOI, Dieter K. SCHRODER, Sergei KOVESHNIKOV[1] and Subhash MAHAJAN[2]
Department of Electrical Engineering and Center for Solid State Electronics Research, Arizona State University, Tempe, AZ 85287-5706, U.S.A.
[1]*SEH America, Inc., 4111 NE 112th Ave., Vancouver, WA 98682-6776, U.S.A.*
[2]*Department of Chemical and Materials Engineering and Center for Solid State Electronics Research, Arizona State University, Tempe, AZ 85287-6006, U.S.A.*

(Received June 20, 2001; accepted for publication July 23, 2001)

It is usually assumed that the iron in iron-contaminated, boron-doped silicon exists as FeB pairs. The iron can be cycled between its interstitial (Fe_i) and paired (FeB) states with the total density Fe_i + FeB remaining constant. We have discovered that iron can also exist in other paired states, which we believe to be Fe-vacancy or Fe-implant damage pairs. When these pairs are destroyed and subsequently when FeB pairs form, we have observed an increased density. We refer to the excess iron (ΔFeB) after re-formation as "latent" iron.

KEYWORDS: silicon, iron, impurities, deep-level transient spectroscopy, Fe–B

Iron is one of the most technologically important impurities in silicon. Recent reviews detail many of the effects of Fe in Si and provide numerous references to previous publications.[1,2] The International Technology Roadmap for Semiconductors requires iron densities below 10^{10} cm^{-3} for future Si processing.[3] Detection of such low iron densities within the Si wafers is possible by several characterization techniques, *e.g.*, surface photovoltage (SPV), photoconductance decay (PCD), and deep-level transient spectroscopy (DLTS).[4] The former two rely on minority carrier diffusion length and recombination lifetime measurements using the kinetics of Fe–B dissociation in boron-doped silicon as a fingerprint,[5] while the latter is a direct measurement. Since Fe in boron-doped silicon exists as either Fe–B pairs or as interstitial iron, Fe_i, DLTS allows a direct measurement of iron in either one of these states. In this paper we show that these characterization techniques can underestimate the Fe density due to a third iron state—the latent iron. The error can be as high as 100%, which can be critical for today's silicon, since such device parameters as diode leakage current, gate oxide integrity, and carrier lifetime depend strongly on iron density.

We have discovered a new and previously unreported effect associated with interstitial iron. This is an increase of the iron density in the wafer after annealing, as illustrated in Fig. 1. This figure is a set of DLTS spectra of a Fe-contaminated Si wafer. Trace (a) is the original spectrum after wafer room temperature storage for two years. It clearly shows the well-known FeB peak at $T = 55.3$ K and essentially no interstitial iron at $T = 253$ K. After a FeB dissociation anneal at 180°C for 30 s, the FeB peak disappears and the Fe_i peak appears at $T = 253$ K, as shown by trace (b). The magnitude of the two peaks is approximately the same, as it should be since Fe–B pairs are changed into Fe_i and substitutional boron B_s. Holding the sample at 80°C for 15 h followed by room temperature storage for 5 days, causes Fe_i and B_s to change back into FeB pairs, shown by trace (c). The change from Fe_i into FeB pairs is well known. What has not been reported before is the significant increase of the FeB density from the initial 2×10^{12} cm^{-3} (trace (a)) to the final 4.5×10^{12} cm^{-3} (trace (c)). We call this excess iron "latent iron", because it was not originally detected as a FeB pair density. What is the source of this excess iron?

We used double side-polished float-zone (FZ), p-type silicon wafers doped with boron to 2.1×10^{14} cm^{-3}. Iron was introduced by thermal annealing at 900°C for 2 hours following iron implantation into the back surface with a dose of 10^{11} cm^{-2} and energy of 100 keV. DLTS measurements on the front wafer surface yielded an iron density of 2×10^{12} cm^{-3}. Schottky diodes were fabricated by aluminum-evaporated contacts on the front surface and a large-area silver paste contact on the back surface. The samples were characterized with current–voltage, capacitance–voltage, and DLTS measurements.

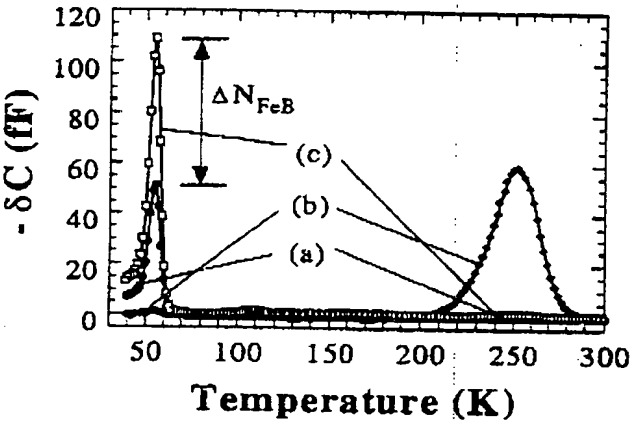

Fig. 1. DLTS spectra of (a) the original sample, (b) after 180°C, 30 s dissociation anneal, and (c) after 80°C/15 h and room temperature 5 day storage.

Capacitance–voltage data showed little change before and after dissociation anneal. This is expected since the effective doping density change, due to boron becoming inactive in the FeB state and active in the unpaired FeB state, is very small because the iron density ($\sim 10^{12}$ cm^{-3}) is much lower than the boron density ($\sim 10^{14}$ cm^{-3}). Schottky diode current–voltage measurements showed a substantial current and diode ideality factor change upon dissociation anneal, possibly associated with changes at the metal/Si interface.

The key DLTS results are shown in Figs. 2(a) and 2(b). The samples were initially measured after storage at room temperature for 2 years. This is the "As-is" curve in both figures. Then they were annealed at 180°C/30 s to dissociate the Fe–B pairs. The FeB peak vanished and the Fe_i peak

-14/04/2004 12:47
14-APR-2004 12:51 TECHNOLOGY-ATO BERLIN S.05/08

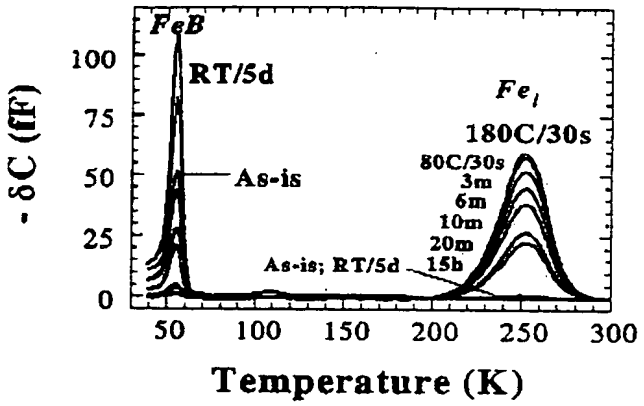

(a)

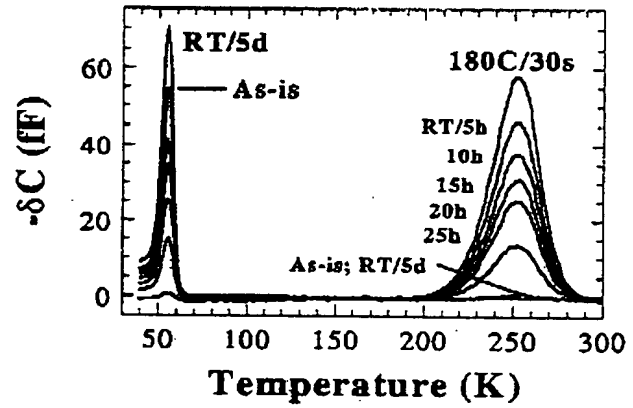

(b)

Fig. 2. DLTS spectra for "As-is", after 180°C/30 s dissociation anneal and (a) 80°C storage for various times followed by room temperature/5 days, (b) room temperature storage for various times.

appeared. The wafer in Fig. 2(a) was then annealed at 80°C for various times up to 15 h and DLTS spectra were recorded. Then the sample was held at room temperature for five days and a last DLTS spectrum was taken. The Fe_i peak has essentially disappeared and the FeB peak has reappeared, but it is significantly higher than the original. The sample in Fig. 2(b) underwent a dissociation anneal as that in 2(a), but was held at room temperature thereafter, instead of at 80°C, and DLTS spectra were recorded. The results are qualitatively similar to those in Fig. 2(a). Note that the magnitude of the "As-is" Fe–B peak and the Fe_i peak immediately after the dissociation anneal are about the same. It is only after an extended time at room temperature or 80°C that the latent iron appears in the new Fe–B peak. The initial 180°C/30 s dissociation anneal is insufficient to generate the latent iron.

In both cases we note the FeB density to be higher after this anneal sequence than at the start. This "latent" iron, denoted as ΔN_{FeB} in Fig. 1, is higher for the 80°C anneal than for the room temperature anneal case. We express this sequence as

$$(FeB)^0 \rightarrow (Fe_i)^+ + (B_s)^- \rightarrow \alpha(FeB)^0$$

with α between 1 and 3. For the $T = 80$°C anneal, $\alpha \approx 2$. The temporal behavior is shown in Fig. 3 for the 80°C anneal case. The FeB density starts out at 2×10^{12} cm^{-3}, drops to approximately zero after the 180°C/30 s anneal, then gradually increases and begins to saturate at 5.4×10^4 s (15 h), the limit of our measurement. After storing the sample at room temperature for 5 days, N_{FeB} increases further. ΔN_{FeB}, defined as the final density minus the initial density, is plotted versus anneal temperature in Fig. 4. It remains reasonably constant, then increases rapidly at around 70°C and appears to saturate around 80–90°C. For each datum point in Fig. 4, ΔN_{FeB} is defined as in Fig. 3. At this point we do not understand the rapid ΔN_{FeB} increase from 70°C to 80°C. From Fig. 3 it appears the additional 5 day room temperature anneal contributes significantly to this increase.

It is generally assumed that all of the iron in boron-doped Si is complexed with boron after storage at room temperature for a few days or longer.[6–8] However, in addition to boron, there may be other possible sinks for iron. Two of these are growth-induced thermal vacancies, and ion implantation-induced damage. Since vacancies can be negatively charged in silicon, they may have Coulombic interaction with positively charged Fe_i. Furthermore, Fe_i^+-V pairing may be facilitated by the difference in covalent tetrahedral radii of Fe and Si atoms. A simple calculation shows that the density of thermal vacancies after a 900°C anneal is sufficiently high to

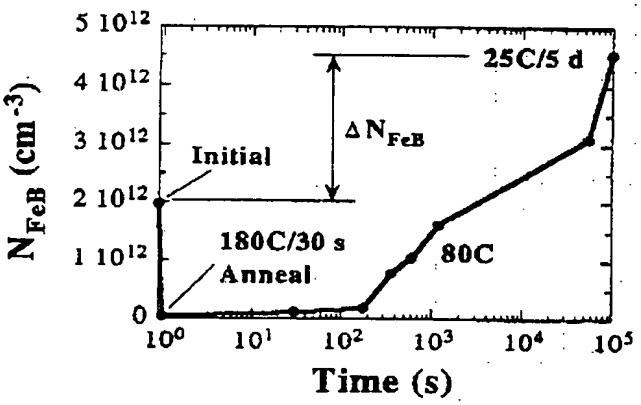

Fig. 3. N_{FeB} as a function of time following various anneals.

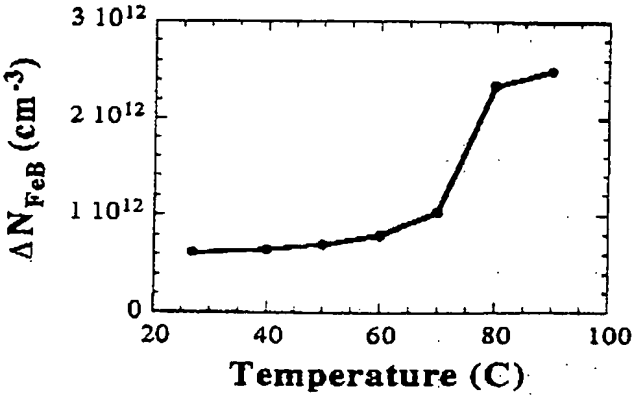

Fig. 4. ΔN_{FeB} as a function of anneal temperature. The time for each temperature was 15 h at each temperature + 5days at room temperature.

14/04/2004 12:48
14-APR-2004 12:51 TECHNOLOGY-ATO BERLIN S.06/08

bond with 2×10^{12} cm^{-3} iron atoms.

Since Fe was introduced in our samples by ion implantation at 100 keV, it is possible that implantation-induced damage occurred in the wafers. This damage could consist of silicon vacancies and interstitials. The majority of these point defects may be annihilated during the 900°C anneal, but some of them may cluster in the form of microdefects or dislocation loops to serve as sinks for iron. The implant created vacancies are generated at the side opposite to the DLTS measurements. The vacancy diffusion coefficient is difficult to determine, but has been given as 10^{-5} cm^2/s at 1100°C with an activation energy of 0.35 to 0.45 eV.[9,10] These values lead to a diffusion coefficient of about 5×10^{-6} cm^2/s at 900°C, giving a $(2Dt)^{1/2}$ diffusion length of 2700 μm, more than sufficient to diffuse through our 700 μm thick wafers. The iron was introduced by thermal annealing at 900°C for 2 hours following iron implantation.

We envisage that during the 180°C anneal, some of the iron atoms may be released from the two types of sinks and become available to form FeB pairs. Even though we are not able to distinguish between the two possible sinks, we feel that ion implantation-induced damage may dominate as a trap for iron atoms because it is more extensive. Interestingly, these pairs do not appear on the DLTS plots over the temperature range of 40–300 K, because they cannot be detected by DLTS or their energy level is such that it is not accessible in the temperature range scanned in the DLTS measurements.

To summarize, we have observed iron in boron-doped Si that we believe to be paired with defects rather than with boron. First, we determine the density of FeB pairs, then dissociate these pairs by a 180°C/30 s anneal and store the samples sufficiently long to reform FeB pairs. The reformed FeB pair density is higher by a factor of two or more than the initial density. We believe the Fe-defect pairs to be either Fe-vacancy or Fe-implant damage pairs.

The research leading to this paper was partially funded by the Silicon Wafer Engineering and Defect Science Consortium (SiWEDS) (Intel, Komatsu Electronic Metals, LG Siltron, MEMC Electronic Materials, Mitsubishi Silicon, Okmetic, Sumitomo Sitix Silicon, Texas Instruments, and Wacker Siltronic Corp.).

1) A. Istratov, H. Hieslmair and E. Weber: Appl. Phys. A **69** (1999) 13.
2) A. Istratov, H. Hieslmair and E. Weber: Appl. Phys. A **70** (2000) 489.
3) Semiconductor Industry Association (SIA), The International Technology Roadmap for Semiconductors, Semiconductor Industry Association, 1999.
4) D. K. Schroder: *Semiconductor Material & Device Characterization* (Wiley-Interscience, New York, 1998) 2nd ed.
5) G. Zoth and W. Bergholz: J. Appl. Phys. **67** (1990) 6764.
6) K. Graff and H. Pieper: J. Electrochem. Soc. **128** (1981) 669.
7) L. C. Kimerling and J. L. Benton: Physica B**116** (1983) 297.
8) W. Wijaranakula: J. Electrochem. Soc. **140** (1993) 275.
9) R. Falster and V. V. Voronkov: Mater. Sci. Eng. B**73** (2000) 87.
10) G. Watkins: Mater. Sci. Semicond. Proc. **3** (2000) 227.

Appl. Phys. A 69, 13–44 (1999) / Digital Object Identifier (DOI) 10.1007/s003399900059

Applied Physics A
Materials
Science & Processing
© Springer-Verlag 1999

(3)

Invited paper

Iron and its complexes in silicon

A.A. Istratov*, H. Hieslmair, E.R. Weber

Department of Materials Science and Engineering of the University of California at Berkeley and
Lawrence Berkeley National Laboratory, MS 62-203, 1 Cyclotron Road, Berkeley, CA 94720, USA
(E-mail: istratov@socrates.berkeley.edu; hhiesl@argon.eecs.berkeley.edu; weber@socrates.berkeley.edu)

Received: 14 December 1998/Accepted: 22 February 1999/Published online: 26 May 1999

Abstract. This article is the first in a series of two reviews on the properties of iron in silicon. It offers a comprehensive summary of the current state of understanding of fundamental physical properties of iron and its complexes in silicon. The first section of this review discusses the position of iron in the silicon lattice and the electrical properties of interstitial iron. Updated expressions for the solubility and the diffusivity of iron in silicon are presented, and possible explanations for conflicting experimental data obtained by different groups are discussed. The second section of the article considers the electrical and the structural properties of complexes of interstitial iron with shallow acceptors (boron, aluminum, indium, gallium, and thallium), shallow donors (phosphorus and arsenic) and other impurities (gold, silver, platinum, palladium, zinc, sulfur, oxygen, carbon, and hydrogen). Special attention is paid to the kinetics of iron pairing with shallow acceptors, the dissociation of these pairs, and the metastability of iron–acceptor pairs. The parameters of iron-related defects in silicon are summarized in tables that include more than 30 complexes of iron as detected by electron paramagnetic resonance (EPR) and almost 20 energy levels in the band gap associated with iron. The data presented in this review illustrate the enormous complexing activity of iron, which is attributed to the partial or complete (depending on the temperature and the conductivity type) ionization of iron as well as the high diffusivity of iron in silicon. It is shown that studies of iron in silicon require exceptional cleanliness of experimental facilities and highly reproducible diffusion and temperature ramping (quenching) procedures. Properties of iron that are not yet completely understood and need further research are outlined.

PACS: 71.55.Cn; 76.30.Fc; 76.80.+y; 66.75.+g; 78.30.Am; 66.30.Jt; 78.55.Ap; 81.05.Cy; 61.72.-y

Iron is one of the most ubiquitous and detrimental metal impurities in silicon. For example, in metal-on-insulator (MOS) structures, iron can precipitate at the Si–SiO_2 interface, thus locally thinning the oxide and increasing surface roughness. This causes premature electric field breakdown of oxides and degrades the gate oxide integrity (GOI) [1–7]. In the depletion regions of MOS devices, iron acts as an effective minority carrier generation site [7,8], increasing the dark current of charge-coupled devices (CCD) [9] and causing refresh failures in dynamic random access memory (DRAM) chips [6]. The generation–recombination centers associated with dissolved iron and its complexes increase leakage currents in any reverse-biased junction, thus increasing power consumption and heat production [10–15]. In crystalline and polycrystalline photovoltaic devices, iron contamination results in the creation of recombination centers which reduce the minority carrier diffusion length and consequently the solar cell efficiency [16]. As device dimensions continue to shrink, the device yield is becoming ever more sensitive to defects and impurities [17,18]. Since the ultrapure technology that enables one to reduce iron surface contamination to the level of below 10^{10} to 10^{11} cm^{-2} is extremely expensive, it has become increasingly important to understand the mechanisms of iron contamination, the detrimental role of iron in silicon devices, and the tolerable limits of iron contamination for each particular technological process. This demand has stimulated great interest in the physics of iron in silicon.

The major obstacle in establishing a coherent experimental picture of 3*d* transition metals in silicon, and of iron in particular, arises from the high diffusivity of these elements. Iron remains mobile at room temperature and can diffuse quickly at temperatures above 100 °C. Since interstitial iron is positively charged in *p*-Si at room and slightly elevated temperatures, it readily forms pairs with negatively charged defects, such as shallow acceptors. The high reactivity of iron was confirmed by electron paramagnetic resonance (EPR) studies, which detected more than 30 complexes of iron, and by electrical measurements, which revealed about 20 deep levels associated with iron (see the discussion below and tables in Appendices A, B).

Iron-related defects in silicon have been intensively studied for more than thirty years. Substantial progress has been made in the last ten to fifteen years. Unfortunately, no

*On leave of absence from the Institute of Physics of St.-Petersburg State University, 198904 St.-Petersburg, Russia

comprehensive review of the properties of iron in silicon has been published since the 1983 review of Weber [19] (and some authors even reference the early reviews of Milnes and Chen [20,21]). The recently published book by Graff [22] is the only exception, but since it covers the whole scope of metal impurities in silicon device fabrication, it is limited to a rather short discussion for each particular metal and does not offer an in-depth insight into the physics of iron in silicon.

Our review is intended to cover the gap between the 1983 review of Weber [19] and the current state of knowledge by giving a comprehensive up-to-date analysis of electrical properties of iron in silicon, its structure, complexing behavior, and recombination properties. We intentionally left out of the scope of this article such important issues as the degradation of devices due to iron contamination, the sources of iron contamination in modern silicon technology, methods of detection of trace concentrations of iron, and the gettering of iron. These will be covered in a separate review, which will be published in one of the forthcoming issues of this journal.

1 Isolated iron as a defect in silicon

1.1 Lattice site of iron in silicon

The donor behavior of iron (see Sect. 1.2.2), its high diffusion coefficient, and the agreement of the electron paramagnetic resonance (EPR) of iron with the model for EPR resonances of interstitial 3*d* metals enabled Woodbury and Ludwig [23] to conclude that Fe diffuses interstitially. The interstitial lattice site of iron was confirmed by Greulich-Weber et al. [24] based on the agreement between the experimentally determined parameters of superhyperfine interactions of iron with silicon ligands measured by electron nuclear double resonance (ENDOR) measurements, and theoretically calculated parameters for interstitial iron (Fe_i). The isomer shift and the broadening of the Mössbauer lines observed by Schwalbach [25] are also in line with the interstitial lattice site of iron in silicon.

There is much speculation in the literature as to what fraction of the total dissolved iron concentration is substitutional iron (Fe_S). For instance, Collins and Carlson [26] observed a "slow" and "fast" diffusing ^{59}Fe species, and assigned them to an interstitially and substitutionally (via vacancy or interstitial-assisted mechanism) diffusing iron, respectively. However, later Stojic et al. [27] demonstrated that the "slow-diffusing" component actually arises from iron that precipitated at the sample surface. To the best of our knowledge, there is no direct experimental evidence for the existence of substitutional iron in a non-distorted configuration. More than 30 iron-related complexes have been detected by EPR, but no iron-related resonance has been found with a *g*-tensor compatible with the model of Ludwig and Woodbury [28] for substitutional metals. The only complex that can be interpreted as substitutional iron in a distorted configuration was detected by Muller et al. [29] in irradiated iron-doped silicon samples. Hyperfine splitting of the spectrum due to ^{57}Fe clearly showed the presence of one iron nucleus in the center. Since the second component of the complex in irradiated silicon is most probably a vacancy, it was suggested that this is a singly positively charged interstitial iron–vacancy complex, $(Fe_iV)^+$. Because the center has ⟨111⟩ axial symmetry, the iron atom can not be exactly at the substitutional position but has to be shifted along a trigonal axis towards the tetrahedral interstitial position [29] (see Appendix A).

He et al. [30] reported that the co-diffusion of Fe and Cu in *p*-type silicon substantially decreases the concentration of interstitial iron detected after diffusion, although no new energy levels associated with FeCu pairs were found in the lower half of the band gap. It was suggested that the decrease of the concentration of Fe_i is due to the transformation of interstitial iron into substitutional iron, caused by the injection of vacancies by diffusing and precipitating copper [31]. While this model agrees with the observations of Woodbury and Ludwig [32] who reported that co-diffusion of Cu with manganese or chromium (or co-diffusion of silver with Mn) resulted in the transfer of interstitial Mn and Cr onto substitutional sites, it is not clear why diffusion of copper should generate vacancies since it is known that copper silicide creates a strong compressive lattice strain and is thus expected to generate interstitials [33,34].

Gilles et al. [35] found a substantial increase (by three orders of magnitude) of iron solubility in n^+-Si with a phosphorus concentration $1 \times 10^{20}\,cm^{-3}$ along with a decrease in the iron diffusivity by almost four orders of magnitude. This was interpreted as an increase of either the fraction of substitutional iron due to heavy *n*-type doping, or the fraction of iron paired with phosphorus [35]. A substantial increase of substitutional solubility in n^+-Si can indeed be expected if substitutional iron forms acceptor level(s) in the band gap. Hall and Racette [36], following Shockley and Moll [37], showed that the substitutional solubility, S_s, of transition metals in extrinsic silicon varies in the nondegenerate case as $S_s = S_{s0} \times (n/n_i)^r$, where S_{s0} is the substitutional solubility in intrinsic silicon, n and n_i are the free electron concentrations in doped and undoped samples, respectively, and r is the multiplicity of the acceptor level of the metal. However, there is no experimental evidence in favor of existence of an acceptor level of substitutional iron. In fact, theoretical calculations using spin-unrestricted density-functional theory with the linear muffin-tin-orbital Green's function method [38,39] as well as self-consistent local-density-functional calculations using ab initio nonlocal pseudopotentials [40,41] predicted that although neutral substitutional iron should be stable in the silicon lattice, it should not have any electrical levels levels in the band gap. A similar conclusion was made from the analysis of Mössbauer spectroscopy data (see, for example, [42–44] and references therein), which revealed one line in the spectra that was attributed to interstitial iron and another one attributed to substitutional iron. Weyer et al. [42] pointed out that the same isomer shift determined for the line attributed to substitutional iron in *p*, *n*, and n^+ silicon is consistent with the above mentioned ([38–41]) theoretical conclusion that Fe_S has no band gap state [38–41]. Note that Mössbauer studies have to use ion implantation to achieve a sufficiently high local concentration of iron, and a substitutional relocation due to a replacement collision with the lattice atoms was suggested as the source of substitutional fraction of iron [42].

Thus, there are no convincing experimental data that substitutional iron exists in detectable concentrations in moderately doped silicon, at least if no vacancies were generated by irradiation or implantation. There are also almost no data on the properties of iron in n^+-Si where the existence of high

concentrations of Fe_S is viable if substitutional iron forms an acceptor level. For this reason, we will confine ourselves in the following discussion only to the properties of interstitial iron and its complexes.

1.2 *Electrical level and microscopic structure of interstitial iron in silicon*

1.2.1 Microscopic structure of interstitial iron: EPR studies. A model for the electron structure of the $3d$ group impurities in silicon was developed by Ludwig and Woodbury [28, 45,46]. According to their model, illustrated in Fig. 1 for the case of iron, all $4s$-shell electrons are transferred to the $3d$ shell. Then, all N valence electrons (filled circles in Fig. 1) of the impurity (atomic configuration $3d^m4s^n$ with $N = m+n$) fill the levels (indicated by lines in Fig. 1) in such a way that a maximum electron spin S is achieved (Hund's rule). The tetrahedral symmetry of the crystal field splits the tenfold degenerate atomic $3d$ orbital into a sixfold degenerate t_2 orbital and a fourfold degenerate e orbital separated by the crystal-field energy (see Fig. 1). Finally, the model of Ludwig and Woodbury assumes a sizeable reduction in the spin–orbit interaction constant. Such "quenching" of the spin–orbit interaction is characteristic for all $3d$ metals. It is explained by either hybridization of the transition-metal orbitals with the surrounding ligands [47], or by the dynamic Jahn–Teller effect [48–50].

The EPR spectrum of neutral interstitial iron, Fe_i^0, was discovered by Ludwig and Woodbury [23,51] and Feher [52]. They reported that the spectrum of neutral interstitial iron of natural isotopic abundance consists of one broad line with a poorly resolved structure, spin $S = 1$, cubic symmetry, and $g = 2.07$ (see Appendix A). For higher microwave energy, a narrow peak appears in the center of the broad EPR spectrum. This spectrum was explained by attributing the broad line to the usual $\Delta M = \pm 1$ transition and the narrow line to the double quantum transition $\Delta M = 2$ (M being the projection of a total angular momentum of the Fe_i along the direction of the magnetic field). For magnetic field direction parallel to ⟨100⟩ and high microwave power levels, the central peak measured in the dispersion mode was found to show a pronounced structure of at least seven equidistant lines which were assigned to the hyperfine interaction with ^{29}Si nuclei in two shells of the nearest and next-nearest neighbors of the interstitial iron atom [53]. The broad line could be resolved into two components by applying a uniaxial stress to the sample [23,54]. This can be easily understood since the zero-field splitting of this $S = 1$ center is negligible in full tetrahedral symmetry and the $M = 1 \leftrightarrow 0$ and $M = -1 \leftrightarrow 0$ transitions coincide. This degeneracy is lifted by applying a uniaxial stress [54,55].

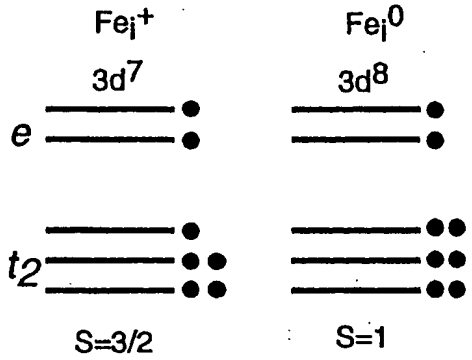

Fig. 1. The electronic structure of ionized and neutral interstitial iron in silicon according to the model of Ludwig and Woodbury (after [28,46])

The isotropic EPR line of Fe_i^+ was first observed in p-Si by Woodbury and Ludwig [23] and was identified in their next paper [56] (see Appendix A). According to the model of Ludwig and Woodbury [28] (see Fig. 1), the ionized interstitial iron should have three unpaired electrons and a spin of $S = 3/2$. However, the effective value of $S = 1/2$ is also frequently used in the literature (for example, [46,57]). Van Kooten et al. [58] showed that Fe_i^+ interacts strongly with the silicon lattice, as the electron spin distribution can be measured over a volume of 98 atoms. From the hyperfine interactions, they derived that the lower limit of the amount of transferred spin to these ligands is 26%. For neutral iron, it was found that from 5% to 25% of the spin density is delocalized on the first six shells of silicon neighbors [24,59].

1.2.2 Electrical properties of interstitial iron. Although numerous experimental data, obtained on intentionally and unintentionally iron-contaminated samples [60–74] suggested that the level at $E_T \approx E_V + (0.40 \pm 0.05)$ eV (for briefness, in the following we will use the notation $E_V + 0.40$ eV instead of $E_T \approx E_V + 0.40$ eV) is associated with iron, it took about 20 years of research starting from the pioneering work of Collins and Carlson [26] to prove that this level is indeed the level of interstitial iron. The ultimate evidence for this was obtained by Feichtinger et al. [75], who diffused iron in n- and p-type silicon with different resistivities and plotted the intensity of the EPR signal as a function of the calculated Fermi level position (Fig. 2). Clearly, the intensity of the EPR spectrum of Fe_i^0 depends on the fraction of iron that is neutral at a given temperature, and thus on the Fermi level position in the sample. As follows from Fig. 2, the charge state of Fe_i changes from Fe_i^+ to Fe_i^0 as the Fermi level crosses the interval from $E_V + 0.36$ eV to $E_V + 0.45$ eV. A more exact data evaluation, which took into account the temperature dependence of the intensity of the EPR lines, enabled Feichtinger et al. [75] to conclude that the position of the interstitial iron level is $E_V + (0.375 \pm 0.015)$ eV. Additional evidence supporting this conclusion include the identical annealing behavior of the Fe_i^0 center detected by EPR and that of the trap at about $E_V + 0.4$ eV [76], the observations that the concentration of this level is close to the total iron concentration measured by neutron activation analysis and EPR [77,78], and that only this level was detected after rapid quenching of samples contaminated with iron [79].

The donor nature of interstitial iron has already been established by the first Hall effect and resistivity measurements [26,80–82], which indicated a reduction in the density of free holes in quenched samples contaminated with iron. Collins and Calson [26] and Wunstel et al. [80] concluded from their Hall effect measurements that the contamination of n-Si with iron does not result in any substantial change in the concentration of free electrons, thus indicating that there is no acceptor level of iron, at least at concentrations above 10^{14} cm^{-3}. Feichtinger [75] provided experimental evidence that, within the limits from $E_C - 0.045$ eV to $E_V + 0.045$ eV, interstitial iron exists in only two charge states: Fe_i^0 and Fe_i^+.

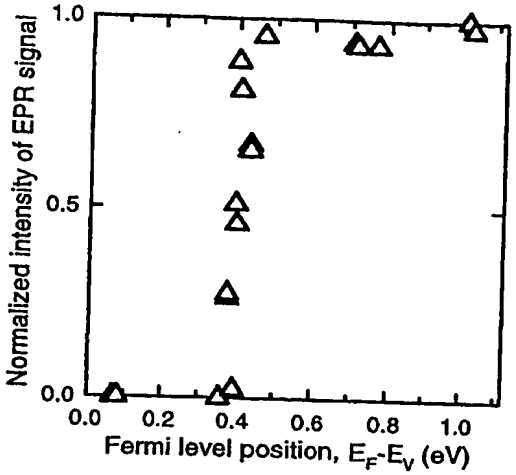

Fig.2. The intensity of the EPR signal associated with Fe_i^0 versus Fermi level position at 95 K (after Feichtinger et al. [75]). The data points were obtained using boron, aluminum, or phosphorus-doped silicon with different levels of doping which enabled the authors of [75] to identify the energy level of the interstitial iron

The temperature dependence of the position of iron level in silicon has received increasing attention in the last several years due to its importance for modelling of segregation-type gettering in p/p^+ epitaxial wafers. The available experimental data indicate that the energy levels of iron, as well as of manganese and cobalt are strongly temperature dependent at high temperatures. These data were inferred from the analysis of the solubility of these elements as a function of doping level [35,83,84]. McHugo et al. [83,84] and Gilles et al. [35] concluded from their neutron activation analysis (NAA) and Mössbauer spectroscopy studies, respectively, that the donor level of iron moves toward the valence band as the temperature increases. Their experimental data are presented in Fig. 3. Both McHugo et al. [83,84] and Gilles et al. [35] concluded that the position of the iron level at $T = 800\,°C$ coincides with that measured by DLTS and Hall effect, whereas at $T > 900\,°C$ the iron level dives towards the valence band and nearly merges with it at $T > 1100\,°C$. This trend follows from both sets of data. McHugo et al. [83,84] pointed out that the iron level shifts so closely to the valence band at 1100 °C that the Boltzmann approximation was no longer valid, so he could not calculate the position of the iron level at 1100 °C. The absence of experimental data between the temperatures where the DLTS and Hall effect data were obtained, and 1000 K, which was the lowest temperature of the solubility studies, makes the interpolation of the iron level position over the whole temperature range difficult. Since in the next sections we will repeatedly make estimates of the ionized fraction of iron at different temperatures and for various types of doping and doping level, it is important to make certain assumptions about the possible shape of the temperature dependence of the iron level despite the lack of experimental data. One can imagine three substantially different simple curves for a temperature dependence of the iron level in the intermediate temperature range, as indicated in Fig. 3: a parabolic fit to the experimental data (curve 1), a step-like function (curve 2) and a smooth curve given by $(E_{Fe}(T) - E_V)/E_g(T) = \text{const}$ (curve 3), where $E_g(T)$ is the temperature-dependent band gap width. In the first case, the depth of the iron level with respect to the valence band edge initially increases and then decreases at high temperatures. In the second case the iron level remains constant up to $T \cong 1000$ K and then dips rapidly toward the valence band. In the last case it drifts smoothly downwards in the whole temperature range. The proportional dependence (curve 3) agrees poorly with the experimentally observed trend in iron level position at high temperatures. A step-like function (curve 2) can describe the experimental data quite well. However, an abrupt change of slope in curve 2 would imply some sort of phase transition [85] in the Fe:Si system. There is clearly no evidence for such a transition. Thus, the parabolic dependence is the only curve of the three, which is smooth and fits well the experimental data. Although it would be premature and speculative to conclude that the temperature dependence of the iron level position in the band gap is described by this parabolic function, we want to attract attention of the scientific community to this possibility. Experimental studies at $T < 1000$ K are required to determine which of the three models provides a better description for the temperature dependence of iron in silicon.

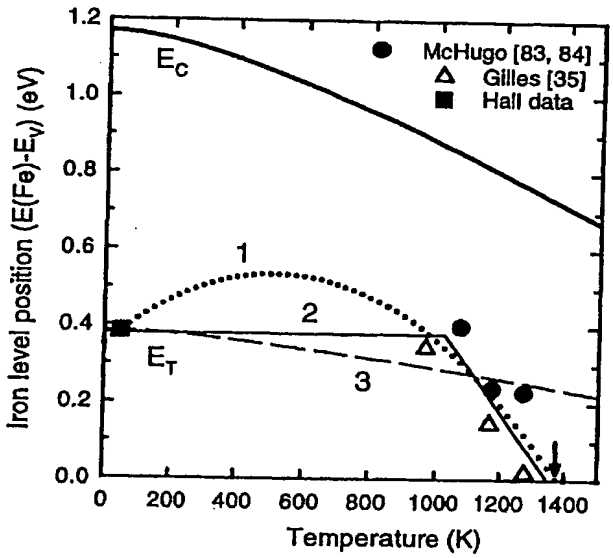

Fig.3. The temperature dependence of the position of the donor level of iron in the band gap with respect to the valence band edge. The symbols represent the experimental data for the iron level position obtained in numerous DLTS and Hall effect studies at low temperatures (*filled square*) and as reported by McHugo et al. [83,84] (*filled circles*) and Gilles et al. [35] (*open triangles*). A data point measured by McHugo et al. [83,84] at 1373 K corresponded to the iron level merging with the valence band and is shown in this figure by an arrow. The lines represent attempts to fit the temperature dependence of the iron level by three different functions: a parabolic fit (*curve 1, dotted line*), a step-like function (*curve 2, solid line*) and a proportional fit $E_{Fe}(T)/E_g(T) = \text{const}$ (*curve 3, dashed line*). The temperature dependence of the band gap width $E_g(T)$ is shown by the thick solid line "E_C". This dependence does not take into account an additional band-gap shrinkage due to heavy doping

The emission of holes from the level of Fe_i was found to be strictly exponential [86]. Despite this, the energy level of Fe_i as determined from deep level transient spectroscopy (DLTS) measurements [78,80,87–90] varied in different studies from $E_V + 0.39$ eV to $E_V + 0.45$ eV. This scatter of emission activation energies is caused by the thermally activated hole capture by Fe_i^0 with an activation energy from 0.04 eV to 0.05 eV, as reported by Brotherton et al. [91] ($\sigma_p = 5.6 \times 10^{-16} \exp(-0.048\,\text{eV}/k_BT)$, cm^2), Wunstel et al. [80] ($\sigma_p = 1.6 \times 10^{-16} \times \exp(-0.043\,\text{eV}/k_BT)$, cm^2), and In-

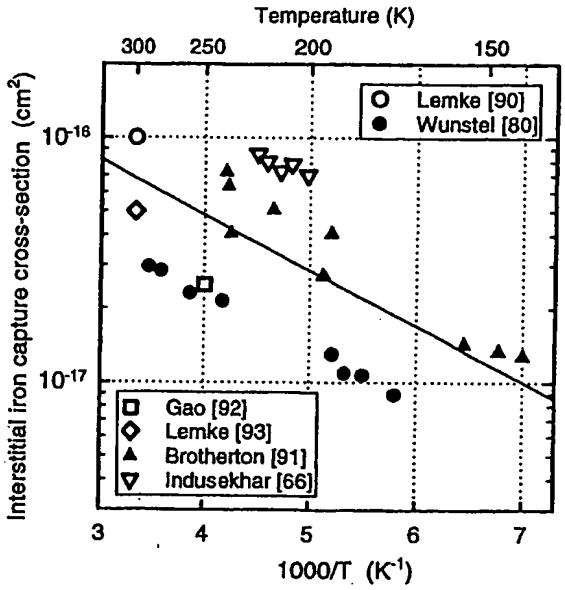

Fig. 4. Temperature dependence of the hole capture cross-section of interstitial iron in silicon according to [66,80,91,92]. The *solid line* represents a fit to all data points, as discussed in the text

dusekhar et al. [66] ($\sigma_p = 6.8 \times 10^{-16} \times \exp(-0.04\,\text{eV}/k_B T)$, cm^2). The data on the hole capture cross-section of Fe_i, including the data from [90,92,93], are summarized in Fig. 4. This figure does not include the data of Gerson et al. [60], who reported a hole capture cross-section of $\sigma_p = 4 \times 10^{-18}\,\text{cm}^2$ but did not explicitly specify the temperature at which it was measured. Graff et al. [78] pointed out that the hole capture cross-section of $\sigma_p = 3 \times 10^{-16}\,\text{cm}^2$ reported earlier by Schibli and Milnes [94] agrees with their data, again without specifying the temperature.

The data points in Fig. 4 are strongly scattered. However, the values for the capture barriers reported in [66,80,91] are similar, which suggests that the scatter is chiefly in the pre-exponential factor. Therefore, we averaged the capture barriers reported in [66,80,91] and then determined the pre-exponential factor by making a least-squares fit to all data points in Fig. 4. This gave us the following expression for the hole capture cross-section of interstitial iron:

$$\sigma_p(Fe_i) = (3.9 \pm 0.5) \times 10^{-16} \times \exp\left(-\frac{0.045 \pm 0.005\,\text{eV}}{k_B T}\right)(\text{cm}^2). \quad (1)$$

It is worth noting that the barrier for hole capture of 0.045 eV explains the discrepancy between the energy level of iron at $E_V + 0.38$, obtained from EPR [75] and Hall effect [21,80], and the average value of $E_V + 0.43$ eV, obtained from temperature dependence of majority carrier emission rate from the iron trap measured with DLTS [80,90,91]. This is because the evaluation of DLTS data by means of an Arrhenius plot does not enable one to distinguish the emission enthalpy and the barrier for capture, and instead yields the sum of both energies: 0.38 eV + 0.045 eV = 0.425 eV. To the best of our knowledge, the nature of this capture barrier was not discussed in the literature.

The optical ionization energy of the level of interstitial iron, as determined by optical methods such as photoconductivity, photocapacitance, and deep level optical spectroscopy, is close to the thermal ionization energy. The reported photoionization energies for the transitions between the impurity level and valence band are in good agreement with each other: 0.43 eV [95], 0.42 eV [66], 0.39 eV [87], and 0.38 eV [81] are close to the thermal ionization energy. The data for transitions from the defect level to the conduction band also show a relatively small scatter: $\Delta E_{opt} = 0.75$ eV [66,95–102]; 0.76 eV [78,87,103]; 0.78 eV [81,104,105].

The electron capture cross-section of Fe_i^+ is not studied as accurately as the hole capture cross-section. Collins and Carlson [26] studied the influence of iron on the minority carrier lifetime in *n*-Si and *p*-Si and found that $\sigma_n \geq 1.5 \times 10^{-15}\,\text{cm}^2$ at room temperature. Lagowski et al. [106] and Zoth et al. [107] reported an electron capture cross-section of Fe_i of $\sigma_n = 4 \times 10^{-14}\,\text{cm}^2$ at 300 K.

A number of theoretical calculations for the structure of electron orbitals and deep levels associated with interstitial iron in silicon have been reported. One of the first calculations was done by Roitsin and Firshtein [108], who used a LCAO molecular orbital method and predicted the position of the *t* level above the *e* level, in contradiction to the model of Ludwig and Woodbury (see Fig. 1). However, later calculations using the spin-restricted scattered-wave $X\alpha$ method reported by DeLeo et al. [109] and Watkins et al. [110], and the self-consistent local-density Green's-function calculations of Zunger et al. [40,111] confirmed that the $5t_2$ level of iron lies below the $2e$ level. It was shown that the $5t_2$ and $2e$ levels represent the antibonding states resulting from the interaction of the transition metal $3d$ state with silicon levels near the top of the valence band.

The positions of the Fe_i level in the bandgap predicted by the theoretical studies mentioned above show a fair agreement with the experimental data. DeLeo et al. [109,112] predicted the $Fe_i^{0/+}$ position at $E_V + 0.68$ eV; Zunger et al. [40] calculated the position of the $Fe_i^{0/+}$ level at about $E_V + 0.53$ eV; Beeler et al. [38,39] predicted the $Fe_i^{0/+}$ level at $E_V + 0.25$ eV. The agreement between experimental data and theoretical predictions became better as the theoretical models developed and the available computational power of the computers increased. Katayama-Yoshida and Zunger [47, 113–115] used the self-consistent all-electron spin-polarized Green's-function method in the framework of the local-spin-density (LSD) formalism and predicted the iron level at $E_V +$ 0.32 eV, whereas Weihrich and Overhof [116] predicted the iron level position at $E_V + 0.29$ eV from ab initio total energy calculations. However, reliable predictions of the energy levels with an accuracy better than 0.1 eV are still not available with today's theoretical approaches.

1.3 Diffusivity of interstitial iron in silicon

1.3.1 Charge state of diffusing iron. The diffusion coefficients of transition metals in silicon depend on the charge state of the metal since the ionic radii of the neutral and ionized species are different, and the degree of the electronic density overlap of the diffusing atoms with surrounding silicon matrix is different. Migration enthalpies and pre-exponential factors of the largest of $3d$ ions can be astonishingly accurately calculated as a difference in the elastic energies at the tetrahedral and the hexagonal interstitial sites using a hard-sphere model, as suggested by Utzig [117]. However,

this model fails for Cu, Ni, Co, and Fe, which have the smallest ionic radii from the 3*d* row. For instance, for neutral iron, Utzig [117] predicted a diffusion barrier of 0.46 eV and a pre-factor $D_0 = 1.34 \times 10^{-3}\,\mathrm{cm^2 s^{-1}}$. No prediction could be made for Fe_i^+ since the ionic radius of positively charged iron is too small to distort the lattice. Obviously, the diffusion barrier of interstitial iron is determined primarily by a strong interaction of iron valence electrons with up to a hundred of surrounding silicon atoms, which indeed was observed in EPR and ENDOR studies [24,58,59]. Theoretical calculations which would take into account such interactions for neutral and positive charge states of iron are lacking. In the following discussion we will show that even experimentalists do not agree if the positive or neutral iron diffuses faster.

The charge state of iron in *n*-Si and *p*-Si at different temperatures can be easily calculated from the position of the $Fe_i^{0/+}$ level with respect to the Fermi level. The temperature dependencies of the fraction of ionized iron in *p*-Si and *n*-Si for the temperatures from 300 K to 1400 K are presented in Fig. 5. The calculations took into account the temperature dependence of the band gap width and of the position of the iron level with respect to the valence band, as shown in Fig. 4 and discussed in Sect. 1.2.2. At room temperature, Fe_i is predominantly positive (and paired with boron) in *p*-type silicon and neutral in *n*-type silicon. At temperatures above approximately 100 to 200 °C the pairs dissociate, and the Fe_i^+ concentration increases. At sufficiently high temperatures (above 600 K) the Fermi level moves to the midgap position, and iron becomes mostly neutral in both *n*-type and *p*-type silicon. The fraction of ionized iron depends on the function chosen to describe the temperature dependence of the iron level position. Parabolic and step-like functions (curves 1 and 2 in Fig. 4, dotted and solid lines in Figs. 4, 5) result in the fraction of ionized iron decreasing with increasing temperature from 10% at 1000 K to 1.5% at 1400 K in both *p*-Si and *n*-Si. On the contrary, the proportional model (dashed lines in Figs. 4, 5) predicts a gradual increase of the fraction of ionized iron from 5% at 1000 K to 10% at 1400 K.

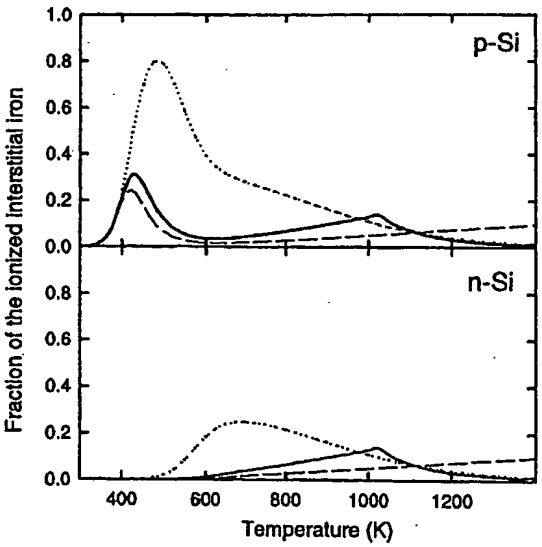

Fig. 5. The equilibrium fraction of ionized interstitial iron in *p*- and *n*-type silicon for different assumed temperature dependencies of the energy level of interstitial iron. The simulations were made for a doping level of $10^{15}\,\mathrm{cm^{-3}}$ and for an iron contamination level much lower than the boron (phosphorus) doping. The *dotted line* (see *curve 1* in Fig. 4), the *solid line* (*curve 2* in Fig. 4), and the *dashed line* (*curve 3* in Fig. 4) correspond to the parabolic, steplike, and proportional temperature dependencies of the interstitial iron energy level. The calculations for *p*-Si also take into account iron–boron pairing, although the concentration of FeB pairs is not shown in the figure. A peak in the Fe_i^+ plot at about 400 K in *p*-Si is due to the dissociation of FeB pairs (see Sect. 2.1, 2.6 for more details). Almost all the ionized iron is paired with boron in *p*-Si at temperatures below 350 K

The predominantly neutral charge state of iron at elevated temperatures agrees with the conclusion of Weber [118], based on the theoretical model of Van Vechten [119], who estimated effective formation enthalpies ΔH_f of metals in silicon of $\Delta H_f \approx 2.4$ eV for neutral interstitials and $\Delta H_f \approx 1.75$ eV for singly positively charged interstitials. Since these predicted values are close to the experimentally observed formation enthalpies of Cr, Mn, Fe, Co ($\Delta H_f \approx 2.1$ eV) and Ni and Cu ($\Delta H_f \approx 1.5$ eV), respectively, Weber [118] suggested that Cr, Mn, Fe, Co dissolve as predominantly neutral species, while Ni and Cu dissolve as positively charged ions. Although experimental data on the charge state of metals at the diffusion temperature are scarce, the available data confirm the model that most of the iron is neutral at the diffusion temperature of 1100 °C [120] while interstitial copper in silicon is positively charged [36,120].

However, this does not necessarily imply that the diffusion coefficient of iron at high temperatures is determined by the diffusivity of neutral iron. While about 95% of iron is neutral at $T > 1000$ K in moderately doped silicon (see Fig. 5), the small fraction of ionized iron may significantly change (or even determine) the apparent diffusivity of interstitial iron, if the diffusion coefficient of the ionized iron is much higher than that of the neutral iron. This will be discussed below.

At low temperatures, the charge state of iron is better defined. It is assumed that iron is neutral in *n*-Si and in the depletion region of reverse-biased Schottky diodes made on *p*-Si, and is positive (and paired with boron) in *p*-Si. However, generation of electron and holes by iron (see, for example, [9]) may make small fractions of iron ionized in the depletion regions of *p*-Si Schottky diodes, and neutral in the depletion regions of *n*-Si Schottky diodes, as pointed out by Heiser et al. [121].

1.3.2 Diffusivity of iron: experimental data. The first expression for the diffusivity of iron obtained by using data in a wide temperature range was reported by Weber [19,122]. He made a fit to the data of Struthers [123], Kimerling et al. [124], and Shepherd et al. [125] and derived a diffusion coefficient of $D(Fe_i) = 1.3 \times 10^{-3} \exp(-(0.68\,\mathrm{eV})/k_B T)\mathrm{cm^2/s}$. Since then, more than 10 research groups reported their results on iron diffusivity [25,35,65,77,90,96,103,106,121, 123,125–139]. Some of them tried to distinguish the diffusivity of the neutral and the positively charged iron. The diffusivity of iron at high temperatures was measured by studying the diffusion profile of Fe_i using radiotracer method [25,35, 123,126] or DLTS [127,128]. Iron diffusivity at low temperatures (below 300 °C) was measured using three techniques: (a) temperature-dependent kinetics of association of iron–acceptor pairs [77,90,125,130–132] in *p*-Si; (b) precipitation of iron at quenched-in and extended defects [103,131,133, 134] in *p*-Si and *n*-Si; (c) studies of iron diffusion across the space-charge region of a Schottky diode [121,135,136]. These data are plotted in Figs. 6, 7 and are discussed below.

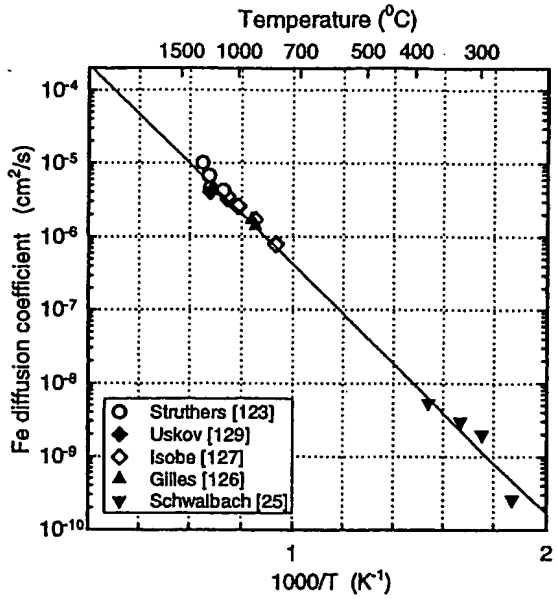

Fig.6. The diffusivity of iron in silicon at temperatures above 250 °C. The *solid line* represents the fit given by (2). The fit was made using data from both this figure and Fig. 7

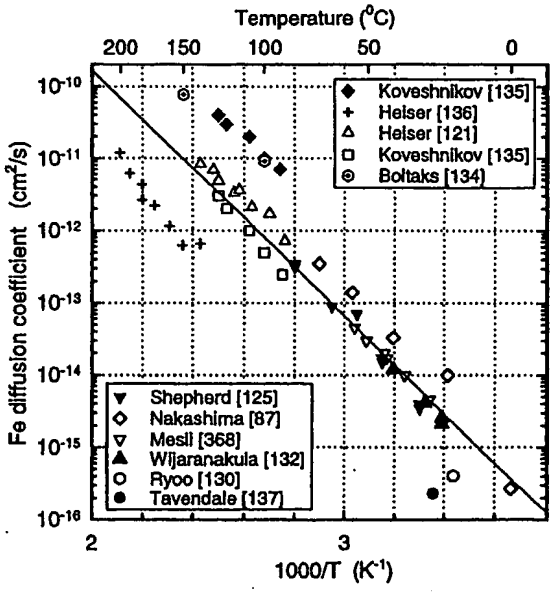

Fig.7. Diffusivity of iron in silicon at temperatures below 250 °C. *Solid line* represents the fit given by (2). The fit was made using data from both this figure and Fig. 6. The *filled diamonds* and *open squares* are the data obtained by Koveshikov et al. [135] for neutral and ionized iron, respectively

The diffusivity data were plotted separately for the high-temperature and the low-temperature range to make the plots more legible. We want to point out that the horizontal and vertical scales of Figs. 6, 7 are identical (so that the readers may combine them into a single oversized graph by cutting and pasting) and a single line is fitted through both graphs.

1.3.2.1 Diffusivity of iron at high and intermediate temperatures. The first four data points for iron diffusivity at high temperatures ($T > 700\,°C$) were obtained by Struthers [123], who reported the diffusion coefficient of $D = 6.2 \times 10^{-3} \times \exp(-0.87\,\text{eV}/k_B T)\text{cm}^2/\text{s}$. His measurements were done in a narrow temperature range (from 1100 °C to 1265 °C) and featured noticeable scatter (see Fig. 6). Uskov [129] evaluated iron diffusivity from the kinetics of iron out-diffusion from the sample at 1200 °C and obtained a value of $D = 4 \times 10^{-6}\,\text{cm}^2/\text{s}$. Antonova et al. [128] measured the depth profiles of Fe after annealing the samples at temperatures between 1000 °C and 1200 °C with short heat pulses and obtained a good agreement with the profiles simulated using the data of Struthers [123]. Isobe et al. [127] determined the diffusion coefficient of iron of $D = 9.5 \times 10^{-4} \times \exp(-(0.65\,\text{eV})/k_B T)\text{cm}^2/\text{s}$ in the temperature range from 800 to 1070 °C from the depth profiles of iron distribution measured by DLTS. Gilles obtained the diffusion coefficient of $D = 1.7 \times 10^{-6}\,\text{cm}^2/\text{s}$ at 920 °C [35,126] and $1.4 \times 10^{-6}\,\text{cm}^2/\text{s}$ at 900 °C [126] from iron out-diffusion experiments.

There is only one set of data points obtained in the intermediate temperature range (between 250 °C and 400 °C) by Schwalbach et al. [25], who evaluated the Fe_i diffusion coefficient from diffusion broadening of Mössbauer spectra of ^{57}Fe nuclei.

1.3.2.2 Diffusivity of iron at low temperatures. The experimental data obtained in the temperature range of 0 °C to 250 °C are plotted in Fig. 7. The experimental conditions of some of the studies were such that iron is expected to be predominantly in neutral charge state. For instance, Lebedev et al. [103] and Takahashi et al. [131] measured precipitation of Fe_i^0 in *n*-type silicon using the photocapacitance method and EPR, respectively, and reported that there was no appreciable Fe_i^0 precipitation at temperatures less than 130 °C. The temperature dependence of the precipitation time constant at $T > 130\,°C$ yielded a diffusion barrier for iron of 0.78 eV [103] and 0.80 eV [131]. However, since the density of precipitation sites was unknown, the pre-exponential factor in the expression for diffusion coefficient could not be determined. Heiser and Mesli [121] used a method originally suggested by Baruch [140] to study the diffusion of Fe_i in space-charge regions of Schottky diodes. The method consists of the application of a reverse bias to a Schottky diode for a long period of time (1 to 100 h) and monitoring the drift of the impurities out of the depletion region by measuring the decrease of the corresponding DLTS peak amplitude. They concluded that the diffusion coefficient of neutral iron is given by $D = 10^{-2} \exp(-0.84\,\text{eV}/k_B T)\text{cm}^2/\text{s}$ (crosses in Fig. 7). Tavendale et al. [137] used the same technique at a single temperature of 25 °C and obtained $D = 2.3 \times 10^{-16}\,\text{cm}^2/\text{s}$. Koveshinkov et al. [135] (filled diamonds in Fig. 7) monitored profiles of redistribution of iron in the depletion region of a Schottky diode during anneals and reported the diffusion barrier for Fe_i^0 of 0.56 eV. Szawelska et al. [96] monitored precipitation of neutral iron in *n*-Si and determined the diffusion activation energy of neutral iron of 0.66 ± 0.01 eV. Finally, Lee [133] derived the activation energy of Fe_i^0 diffusion of 0.69 ± 0.03 eV from kinetics of precipitation of Fe_i^0 by EPR in the temperature range from 400 K to 470 K.

Studies of the diffusivity of positively charged iron were done using predominantly *p*-type silicon. Heiser and Mesli [121] studied diffusion and drift of Fe_i^+ in the depletion region of a Schottky diode and determined the diffusion barrier of Fe_i^+ of 0.69 eV (open triangles in Fig. 7). Their experimental data suggested that the diffusivity of Fe_i^+ at 300 K

is higher than that of Fe_i^0 by a factor of 50. Koveshnikov et al. [135] studied redistribution of iron in the space-charge region of a Schottky diode and, in disagreement with Heiser et al. [121], reported that the diffusion barrier of Fe_i^+ was 0.92 eV (open squares in Fig. 7), i.e., higher than that of Fe_i^0, and that the absolute values of diffusivity of Fe_i^+ were lower than those of Fe_i^0. Boltaks et al. [134] studied precipitation of Fe_i^+ at dislocations and derived the diffusion coefficient $D(Fe_i^+) = 6.3 \times 10^{-4} \exp(-(0.58\,eV)/k_BT) cm^2/s$. Nakashima et al. [77] determined Fe_i^+ diffusivity from the reaction of association of FeB pairs and suggested the diffusion coefficient $D(Fe_i^+) = 3.3 \times 10^{-1} \exp(-0.81\,eV/k_BT) cm^2/s$. From similar studies, Shepherd and Turner [125] and Reiss et al. [141] concluded that the diffusion barrier was 0.75 eV, whereas Wijaranakula [132], Lagowski et al. [106], and Obermeier et al. [8] obtained a good agreement with the diffusion barrier of 0.68 eV suggested by Weber [19]. Kimerling et al. [138,139] and Lemke [90] concluded from association kinetics of the pairs that the diffusion barrier is 0.85 eV and 0.83 eV, respectively. Association studies of Kaniava et al. [142,143] resulted in activation energies of 0.49 eV and 0.55 eV for two different wafers. This unusually low value was explained by the high injection level used for the carrier lifetime measurements to determine the FeB pairing rate. They suggested that the high density of injected minority carriers might retard the pairing process by partial photo-dissociation of FeB pairs during the carrier lifetime measurement cycle [143]. Swanson [65] studied temperature dependence of decay of the quenched-in level at $E_V + 0.4$ eV (which was unambiguously iron) and found that the activation energy of this process was 0.81 ± 0.04 eV.

1.3.3 Diffusivity of iron: analysis of data. Thus, there is a significant scatter from 0.49 eV to 0.92 eV in diffusion barriers reported for interstitial iron. Additionally, there is no agreement whether ionized or neutral iron diffuses faster. While most of the authors that compared diffusivities of Fe_i^0 and Fe_i^+ agree that neutral iron has a higher diffusion barrier than Fe_i^+ [121,131,136,144], Koveshnikov et al. [135] came to the opposite conclusion. Heiser et al. [145] suggested that this contradiction can be partly explained as a consequence of FeB pairing, i.e., that Koveshikov et al. [135] measured the *effective* diffusion coefficient of the ionized iron, affected by pairing with boron. It is known that pairing may decrease the apparent diffusivity by orders of magnitude [146]. The importance of a correct evaluation of pairing with shallow acceptors can be illustrated by the example of copper in silicon. As we recently showed [147], the generally accepted expression for copper diffusivity [36] underestimated the copper diffusion barrier by more than a factor of two, and thus the room temperature intrinsic diffusivity by three orders of magnitude, due to an incorrect accounting for the pairing of copper with boron. As will be discussed below, the data on the pairing constants of iron with boron remain ambiguous, thus hampering accurate evaluations of the effect of pairing, as was the case of Cu in Si in [147].

It is clear that an accurate value for the diffusion barrier for neutral or ionized iron can be obtained only by using experimental data in a wide temperature range. Unfortunately, this is difficult if not impossible since iron usually co-exists in both neutral and ionized charge states. The apparent diffusion coefficient of iron diffusing in two charge states is given by $D_{app}(Fe_i) = fD(Fe_i^+) + (1-f)D(Fe_i^0)$, where f is the fraction of ionized iron, and $D(Fe_i^+)$ and $D(Fe_i^0)$ are the diffusion coefficients of ionized and neutral iron [35]. For example, if we assume that the diffusivity of Fe_i^+ at a temperature T is much higher than the diffusivity of Fe_i^0 ($D(Fe_i^+) \gg D(Fe_i^0)$), then the apparent diffusion coefficient $D_{app}(T)$ will be determined by the diffusion barrier of Fe_i^+, $E_m(Fe_i^+)$, despite the relatively low fraction, f, of the ionized iron. However, the pre-factor in the diffusion coefficient will be reduced by the value of coefficient f, which is, in turn, temperature dependent. The consequence of the temperature dependence of f is that neither the diffusion barrier of Fe_i^0 nor that of Fe_i^+ can be straightforwardly extracted from the temperature dependence of $D_{app}(Fe_i)$.

Despite the lack of understanding of the charge state of diffusing iron, the experimental data points for both Fe_i^0 and Fe_i^+, all plotted in the same plot, can be fitted by a single straight line (Figs. 6, 7) with a slope corresponding to the diffusion barrier of $E_m(Fe_i) = 0.67 \pm 0.02$ eV. The majority of experimental data points can thus be described by the equation

$$D(Fe_i) = (1.0^{+0.8}_{-0.4}) \times 10^{-3} \exp\left(-\frac{0.67\,eV}{k_BT}\right), \; cm^2/s. \qquad (2)$$

It is worth noting that this expression agrees within the error limits with the one previously reported by Weber [19,118], $D(Fe_i) = 1.3 \times 10^{-3} \exp(-(0.68\,eV)/k_BT) cm^2/s$. Although almost all data points in Figs. 6, 7 are fitted by (2), we would not conclude from this result that the diffusion barrier of iron does not depend on its charge state. We believe that this agreement actually confirms the difficulties with the analysis of iron diffusivity due to co-existence of iron in both charge states in all or almost all imaginable experiments. Since we can assign (2) to the diffusivity of neither ionized nor neutral iron, we will call it the "effective diffusion coefficient of iron". Equation (2) is sufficient for most technological purposes such as prediction of intrinsic gettering behavior of iron. Yet, the physics of iron diffusion can not be understood without further experimental and theoretical studies.

The discrepancy between the FeB pairs association experiments, which in most cases resulted in a Fe_i^+ diffusion barrier from 0.75 eV to 0.8 eV, and the overall fit of most experimental data to the diffusion barrier of 0.67 eV, deserves a separate discussion. We believe that this discrepancy is explained by at least two reasons.

First, the FeB association experiments could be made, at least partly, in a temperature range where the association rate of the pairs is close to the dissociation rate. In this case, the rate of the observed reaction is given by the sum of the association and dissociation rates of the pairs. An Arrhenius plot of the apparent reaction rate will then give an activation energy which lies somewhere between the barriers for association and dissociation of the pairs. This will be discussed in detail in Sect. 2.1.6.

Another possible explanation follows from the recent experimental studies by Takahashi et al. [148,149], who suggested that the height of the potential barrier for a jump of Fe_i^+ from the second-nearest interstitial position to the first nearest interstitial position to the acceptor depends on the chemical nature of the acceptor (0.75 ± 0.01 eV for Al, 0.72 ± 0.01 eV for Ga, and 0.69 ± 0.01 eV for In), and is *higher* than

the potential barrier for diffusion of Fe_i^+ ions from the bulk of the sample to the second-nearest position. This latter barrier was found to be 0.68 ± 0.01 eV [148], in a good agreement with the high-temperature studies. It is interesting to note that the reported height of the energy barrier for the last jump increases with decreasing atomic number of the acceptor. Extrapolating the dependence reported in [148] to boron, one obtains a value of about 0.78 eV, which in fact is very close to the barrier for association of FeB pairs reported by a number of researchers.

The diffusivity of Fe_i in heavily doped wafers is poorly investigated. We are aware of only one study, performed by Gilles et al. [35,126]. Using radioactive tracer techniques, they found that the diffusivity of iron at 700 °C is $D = 4 \times 10^{-11}$ cm^2/s for the phosphorus doping level of $N_P = 1 \times 10^{20}$ cm^{-3}, and $D = 2.4 \times 10^{-7}$ cm^2/s for the boron doping level of $N_B = 8 \times 10^{19}$ cm^{-3}. The intrinsic diffusivity of iron at the same temperature, given by (2), is $D = 3.4 \times 10^{-7}$ cm^2/s. The small decrease of the diffusion coefficient in p-Si was ascribed to the pairing reaction of Fe_i with B, and the pronounced decrease in n-Si was explained by the significant fraction of substitutional Fe in strongly n-doped Si or by possible pairing reactions with P [35,126]. An alternative explanation for a strong decrease of the Fe diffusivity, which follows from the discussion above, might be the diffusion of Fe_i exclusively in the neutral charge state in n^+-Si. This is plausible since the Fermi level remains in the upper half of the band gap in n^+-Si even at 700 °C, and the positively charged fraction of iron is negligible.

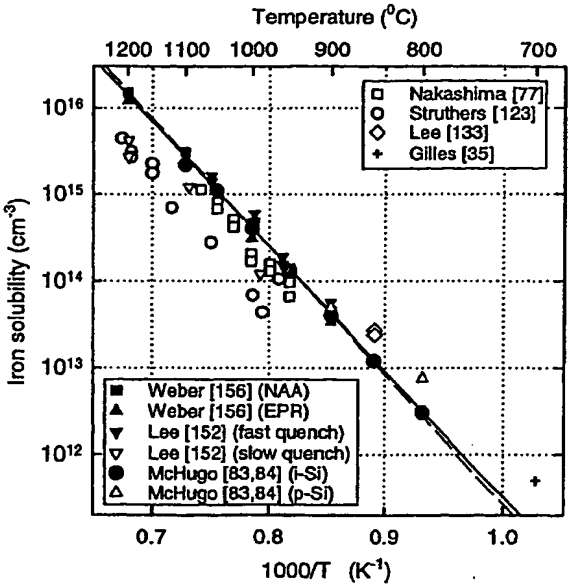

Fig.8. The solubility of iron in silicon below 1200 °C. The *dashed line* corresponds to the 1983 plot of Weber [19], (3), whereas the *solid line* is the new fit given by (4). The *solid line* was obtained by a nonlinear least-squares fit to solid symbols in the figure (see discussion in the text). The data points reported by Lee et al. [133] are represented by three different symbols depending on the temperature range where they were obtained, as well as the quenching rate used (see the graph legend and discussion in the text). The solubility data obtained on heavily doped silicon are not included in this plot and are presented in Fig. 9

1.4 Solubility of iron in silicon

The solubility of iron increases with temperature below the eutectic temperature, passes through a maximum, and finally decreases above the eutectic temperature, which is 1207 °C for the Si-rich $FeSi_2$ phase [150–152]. For other Fe-Si phases, the eutectic temperature varies from 1200 °C to 1250 °C [150]. The retrograde solubility of iron above the eutectic temperature was reported by Trumbore [153] and Feichtinger [154]. The solubility of iron below the eutectic temperature was studied by a number of groups [35,77,83, 84,123,133,155–157]. Their experimental data are plotted in Fig. 8. The data published before 1980 were reviewed by Weber [19,156], who suggested the following expression for the solubility of iron in silicon:

$$S = 1.8 \times 10^{26} \exp(-(2.94 \pm 0.05\,\text{eV})/k_B T),\ \text{cm}^{-3}. \quad (3)$$

This expression was derived using data points in a relatively narrow temperature range (from 950 °C to 1200 °C) and is shown by a dashed line in Fig. 8. Not all data points available at that time were used in the linear fit since Weber [156] found that the solubilities of iron obtained by EPR or DLTS (open symbols at temperatures above 950 °C K in Fig. 8) are in most cases 2 to 3 times lower than the values obtained by neutron activation analysis (NAA). At least four possible reasons for that were discussed in the literature. First, it was suggested that part of the iron may dissolve substitutionally and may not be detected by techniques sensitive only to the interstitial iron [157]. However, as discussed in Sect. 1.1, later studies failed to detect substitutional iron in quenched samples. Weber [19,156] pointed out that an insufficient concentration of iron on the silicon surface, or formation of a surface silicon oxide acting as a diffusion barrier for iron (see, for example, [158]) may decrease the dissolved concentration of iron below its equilibrium solubility. On the other hand, the concentration of iron may exceed the equilibrium solubility if the equilibrium with a surface silicide is not established. Such a peak in the concentration of dissolved iron, exceeding the equilibrium solubility by up to 50%, was observed during the first 20–30 min of diffusion [19]. The third possible reason for the disagreement of experimental data are traces of oxygen in argon or nitrogen gases, frequently used as the ambient for iron diffusion. The formation of an oxide layer at the silicon surface, acting as a diffusion barrier, or oxidation of the iron, may result in a lower concentration of iron in the bulk than its equilibrium solubility [78,156,159,160]. This problem is usually solved by using reducing gas, a mixture of hydrogen with nitrogen or argon. Finally, the most important reason for disagreement in iron solubility during the metal diffusion is, from our point of view, that the quenching rate used in some experiments might be insufficient to quench all iron interstitially and prevent the formation of complexes and agglomerates of iron (see discussion below in Sect. 4, 5), the gettering of iron by oxygen precipitates or extended defects (see [133]), or the outdiffusion of iron (see, for example, [121,136,161]). Colas et al. [162] even suggested that oxygen precipitates may reduce iron solubility in silicon. Later it was understood that they actually observed gettering of iron by the oxygen precipitates during cooling. Clearly, precipitated/agglomerated iron can not be detected by methods selective to Fe_i, and leads to an underestimation of the total iron concentration. Summarizing the discus-

sion above, reliable values for iron solubility can be obtained after anneals that are sufficiently long to establish the iron-silicide boundary phase (about 1 h), conducted in a reducing gas ambient, and terminated by a quench in a vertical furnace. Since a number of data points reported in the literature for $T > 950\,°C$ obviously did not comply with these requirements (for example, used slow cooling rates), they resulted in underestimated solubility values and were not used in the fit. These data points are indicated by open symbols in Fig. 8.

Lee et al. [133] and Gilles et al. [35] reported several data points between 700 °C and 950 °C that lie above the extrapolation done by Weber [155,156] (open diamonds and triangles at $T < 1100$ K in Fig. 8). The origin of this discrepancy became clear only after the recent studies by McHugo et al. [83,84], who measured solubility of iron in intrinsic, moderately p-doped (6.5×10^{14} B/cm^3), and heavily boron-doped (1.5×10^{19} B/cm^3) silicon in the temperature range from 800 °C to 1100 °C using NAA. In agreement with the previously reported data of Gilles [35], they found a significant increase in solubility in heavily doped substrates (Fig. 9). McHugo et al. [83,84] showed that this solubility enhancement in p^+ silicon is significant only at low temperatures $T < 1000\,°C$ (Fig. 8). Furthermore, the dependence on the doping level at $T < 1000\,°C$ is so strong that even a relatively low boron doping (6.5×10^{14} B/cm^3) results in a substantial increase in solubility, as shown by open circles in Fig. 9. Thus, the data obtained on intrinsic and doped silicon at temperatures below 1000 °C should be distinguished in the solubility plot shown in Fig. 8. We therefore excluded from the following analysis several data points which were obtained at $T < 1000\,°C$ on non-intrinsic silicon (open symbols at $T < 850\,°C$ in Fig. 8). A linear fit made using filled symbols in Figs. 8, 9 yielded the following updated expression for the solubility of iron in *intrinsic* silicon in the temperature range

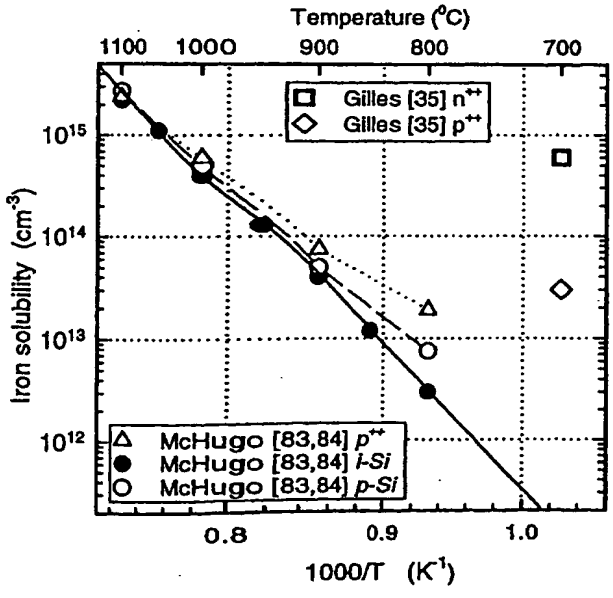

Fig.9. The solubility of iron in silicon as a function of the substrate doping level. The *solid line* is given by (4) (the same line as in Fig. 8) and corresponds to the intrinsic solubility of iron. The doping levels are: 1×10^{20} cm^{-3} (phosphorus), *open squares*; 8×10^{19} cm^{-3} (boron), *open diamonds*; 1.5×10^{19} cm^{-3} (boron), *open triangles*; 6×10^{14} cm^{-3} (boron), *open circles*. The *filled circles* correspond to intrinsic silicon

800 °C to 1200 °C:

$$S = (8.4^{+5.4}_{-3.4}) \times 10^{25} \exp\left(-\frac{2.86 \pm 0.05\,\text{eV}}{k_B T}\right),\ \text{cm}^{-3}. \qquad (4)$$

It is worth noting that (4) agrees within the error limits with the (3) reported by Weber in 1983 [19]. A discussion of the formation enthalpy of iron above the eutectic temperature can be found in the 1983 review of Weber [19]. Those data are not updated in this review since, to the best of our knowledge, no new data on solubility of iron at silicon above the eutectic temperature have been reported during the last 15 years.

The authors of this review are aware of only one theoretical calculation of the solubility of iron made by Fistul and Shmugurov [163]. They developed a model of potentials of the interaction of the impurity atom with the surrounding silicon lattice and then calculated the enthalpy of formation of Fe_i^0 of 2.02 eV, which is reasonably close to the experimental data.

2 Pairing of interstitial iron with shallow acceptors

2.1 Iron–boron pairing

2.1.1 EPR studies of FeB *pairs.* The possibility of pairing of iron with boron was suggested as early as in 1957 by Collins and Carlson [26]. They did not, however, detect the pairing since their experiments were done at temperatures too high for a significant iron–boron pairing to occur. Evidence that iron–boron pairs do form was obtained from the EPR studies by Ludwig and Woodbury [28,45] (see Appendix A). They detected the paramagnetic resonance associated with the ⟨111⟩-oriented FeB pairs and suggested that their paramagnetism arises from three unpaired electrons of the $3d^7$ iron impurity in the crystal field of the negative acceptor. According to their model, the spin density of the ionized acceptor is small and does not substantially contribute to the resonance of the pair. Although the real spin of the pair is $S = 3/2$ [164,165], the symmetry of the resonance can also be described using the effective spin $S = 1/2$. The superhyperfine splittings due to interstitial ^{57}Fe and ^{11}B, along with the very weak ^{29}Si ENDOR line, measurable only along the ⟨111⟩ direction, were reported by Spaeth et al. [166].

The resonance of the acceptor state of FeB pairs was detected by Gehlhoff and Rehse [167,168] using EPR under constant illumination (see Appendix A). They found that the spectrum is ⟨111⟩ axially symmetric and identified it as a FeB pair from the observed line splitting due to isotopes ^{10}B, ^{11}B, and ^{57}Fe.

2.1.2 Electrical, optical and recombination properties of FeB *pairs.* The identification of the energy level of $(FeB)^{0/+}$ at $E_V + (0.10 \pm 0.01)$ eV was made by Feichtinger [157] from Hall effect studies and confirmed by a number of Hall effect and DLTS studies of various research groups [80,91,92]. Graff and Pieper [78] and Kimerling et al. [124] corroborated the identification of this level as that of the iron–boron pairs by monitoring the dissociation and association kinetics of the pairs. Graff and Pieper [78] also showed by using infrared absorption spectroscopy that the sum of the concentrations

of the levels at $E_V + 0.38$ eV and $E_V + 0.1$ eV remains constant during the association/dissociation reactions, and that the concentration of the unpaired substitutional boron decreases during the association reaction and recovers during dissociation. The correlation between concentrations of Fe_i and FeB was confirmed by the EPR studies of Weber [169]. A decrease in the boron concentration and an equal increase in the concentration of FeB pairs was also observed in Hall effect studies [154]. The donor nature of the FeB pairs was inferred from the comparison of the resistivity data and the Hall effect data before and after the pairing reaction [78,154].

The hole capture cross-section of the FeB pairs was reported to be $\sigma_p = 1.5 \times 10^{-13}\,cm^2$ at $T = 55$ K [92], and $\sigma_p = 2 \times 10^{-14}\,cm^2$ as measured by DLTS between 50 K and 65 K [80] (see Appendix B). No thermal activation of the capture cross-section of holes by FeB pairs was reported [80]. Zoth and Bergholz [107] reported the electron capture cross-section of FeB pairs at room temperature to be $\sigma_n = 4 \times 10^{-13}\,cm^2$. However, this value may be somewhat inaccurate since they did not take into account the possibility of recombination through the acceptor level of the pairs (see discussion below).

Besides the well-known donor level at $E_V + 0.1$ eV, the FeB pair has also an acceptor level in the upper half of the band gap. Using a simple ionic model of the FeB pair, Feichtinger [154], Kimerling et al. [138] and Lemke [170] assigned the electrical level of FeB at $E_V + 0.1$ eV to the double-donor state of $Fe_i^{+/++}$, pulled up from the valence band into the band gap (Fig. 10) by the electrostatic interaction with the nearby charge of opposite sign (B_S^-). Assuming that the same interaction would raise the position of the level of interstitial iron $Fe_i^{0/+}$ in the negatively charged FeB pair by the electrostatic interaction energy of $E_{ionic} = q^2/(4\pi\varepsilon\varepsilon_0 r) = 0.52$ eV (where $r = 0.235$ nm, the distance between the closest substitutional and interstitial sites), one would expect [171] the acceptor state $(FeB)^-$ to have a level in the upper half of the band gap at about $E_C - 0.25$ eV (Fig. 10). This prediction was found to be in remarkably good agreement with the experimental findings of Brotherton et al. [91], $E_C - 0.29$ eV, Lemke [90], $E_C - 0.23$ eV, and Nakashima et al. [172], $E_C - 0.29$ eV, all obtained using p-type samples and capacitance spectroscopy techniques with minority carrier injection. Gehlhoff and Rehse [167,168] estimated the energy position of the $(FeB)^{-10}$ level in the band gap at $E_C - (0.25 \pm 0.05)$ eV from the observed onset of the spectral dependence of the photo-induced change of the EPR

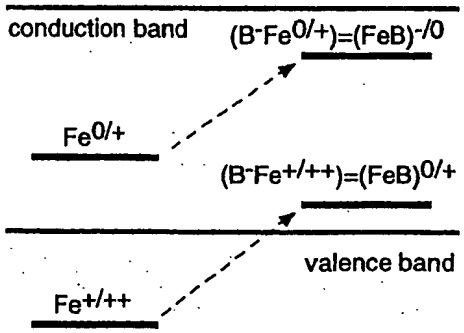

Fig. 10. A diagram of the energy levels of the interstitial iron in the electrical field of a shallow acceptor (after [138,154,170]). This diagram is based on the ionic model of iron–boron pairs

signal. As was mentioned above, this EPR spectrum was identified as that of the FeB pairs from the observed line splitting due to the isotopes ^{10}B, ^{11}B and ^{57}Fe. The identification of the level at $E_C - 0.29$ eV as $(FeB)^-$ was confirmed using Fourier transform spectroscopy (FTIR) by Ghatnekar–Nilsson [173,174]. They identified four sharp lines in the FTIR spectrum at 6969.6, 6978.4, 7008.3, and 8291.7 cm^{-1} as the absorption by trigonal FeB pairs and evaluated from their experimental data the positions of two levels of FeB pairs at $E_V + 0.11$ eV for the $(FeB)^{0/+}$ and at $E_C - 0.275$ eV for the $(FeB)^{-/0}$ pair.

Lemke [90] reported the capture cross-sections of $(FeB)^{-10}$ at $T = 90$ K of $\sigma_n \approx 10^{-15}\,cm^2$ and $\sigma_p \approx 3 \times 10^{-15}\,cm^2$ for electrons and holes, respectively. Waltz et al. [175,176] reported similar values of $\sigma_n \approx 2.5 \times 10^{-15}\,cm^2$ and $\sigma_p \approx 3 \times 10^{-14}\,cm^2$ at room temperature.

Both interstitial iron and FeB pairs are strong recombination centers. The recombination activity of FeB pairs at low injection levels is about 10 times lower than that of interstitial iron [106,107]. The minority carrier diffusion length measured by surface photovoltage (SPV) before (L_0) and after (L_1) dissociation of the pairs is quantitatively related to the concentration of interstitial iron, N_{Fe}, as follows [107]:

$$N_{Fe} = 1.06 \times 10^{16} \times \left(L_1^{-2} - L_0^{-2}\right)\,(cm^{-3}), \qquad (5)$$

where L_0 and L_1 are measured in microns. It is somewhat unexpected from the Shockley–Read–Hall (SRH) statistics [177,178] that the level of FeB pairs at $E_V + 0.1$ eV, being so shallow, is such a strong recombination center. This controversy was explained [91] by the suggestion that recombination, particularly at low injection levels, takes place via the acceptor state at $E_C - 0.29$ eV which is closer to the midgap than the donor level of the FeB pairs. This model was later confirmed by a number of studies of the temperature dependence of minority carrier lifetimes in iron-contaminated silicon [142,179] and the dependence of the effective lifetime on minority carrier injection level [142,175,176]. A complete model of recombination via the FeB pairs, valid for both high and low injection levels can be developed only taking into account both the donor and the acceptor levels of FeB [180,181]. As it can be shown from the SRH statistics (see [182]), the recombination activity of shallow levels increases as compared to that of deep levels with increasing injection level $\eta = \Delta n/p_0$, where p_0 is the equilibrium density of holes in the sample, and Δn is the density of injected electrons. A number of groups [142,143,181,183,184] showed that the recombination activity of FeB pairs actually becomes higher than that of Fe_i if the injection level is high. Thus, it is important to remember that (5) is valid only for low injection levels as used in the SPV technique. Furthermore, the coefficient 1.06×10^{16} in (5) is valid for typical 5 to 10 Ω cm silicon and may vary depending on the Fermi energy level, i.e., on resistivity of the wafers [185]

Only the trigonal ⟨111⟩ symmetry has been detected for FeB pairs, whereas orthorhombic ⟨100⟩ configurations have also been reported for the other donor–acceptor pairs (Sect. 2.2, 2.3). It is important to emphasize that the difference between the trigonal and the orthorhombic configurations of the iron–acceptor pair is not only in the symmetry, but also in the distance between the iron and the acceptor. This distance is $r = 0.235$ nm (the nearest-neighbor distance be-

tween Fe_i and B_S) for the trigonal symmetry of the pair and $r = 0.272$ nm (the second nearest-neighbor distance between Fe_i and B_S) for the orthorhombic symmetry of the pair. In some cases, we will also have to mention the second nearest position *along the* ⟨111⟩ *direction*. This actually corresponds to the *third* nearest-neighbor distance between Fe_i and B_S. $r = 0.450$ nm.

A number of researchers tried to detect the orthorhombic configuration of FeB pairs using capacitance spectroscopy methods. Dobaczewski et al. [86,186] applied the high-resolution Laplace-transform DLTS technique to the capacitance signal of FeB pairs and found a well-defined single peak in the Laplace spectrum, which corresponds to a monoexponential emission from the FeB level at $E_V + 0.1$ eV. They also found that another level with a hole emission activation energy of 0.074 eV appeared in the spectrum after dissociation of FeB pairs by minority carrier injection at 150 K. The level was found to be unstable at room temperature and annealed out after several hours. As with the pairs of levels associated with FeAl, FeIn, and FeGa complexes (see Sect. 2.2, 2.3, 2.4, 2.6 below), it was suggested that this level is an unstable donor level of the orthorhombic configuration of FeB pairs [86]. The position of this second level of FeB at $E_V + 0.07$ eV is in agreement with the general trend specific to iron–acceptor pairs that the level of the orthorhombic configuration of the pair is closer to the valence band edge than that of the trigonal configuration.

A whole set of deep levels associated with different configurations of FeB pairs has been reported by Nakashima et al. [172,187–189], who studied dissociation of FeB complexes under low level minority carrier injection (1 to 100 mA/cm^2) at $T = 150$ K. The idea of their experiment was that the minority carrier injection will assist iron to make a jump from the interstitial position nearest to boron to one of the next neighbor positions. If the temperature is low enough to prevent thermally activated diffusion of iron, these metastable configurations can be "frozen in" and will become detectable by electrical measurement techniques. Indeed, they found four unstable electron traps at $E_C - 0.43$ eV, $E_C - 0.46$ eV, $E_C - 0.52$ eV, $E_C - 0.54$ eV, and two hole traps at $E_V + 0.53$ eV and $E_V + 0.48$ eV. These levels annealed within 10 min at temperatures ranging from 200 K to 240 K. The annealing kinetics [187,189] revealed activation energies for each of the traps varying from 0.65 eV to 0.75 eV with pre-exponential factor close to 10^{12}–10^{13} s^{-1} as would be expected for a single-jump process (i.e., the lattice vibration frequency). The activation energy was explained [187,188] as the barrier to atomic motion of Fe_i^+ ion from one configuration to another. The concentration of the FeB acceptor level at $E_C - 0.29$ eV, which was the only level in the upper half of the band gap before the minority carrier injection, decreased in concentration after injection by a value equal to concentration of the emerging metastable levels. It was suggested [188] that the level at $E_C - 0.43$ eV is the acceptor level of the ⟨100⟩ orthorhombic configuration of FeB pairs.

2.1.3 Equilibrium binding energy of FeB *pairs.* The formation and dissociation reactions of FeB pairs are determined by three energies schematically presented in Fig. 11: the equilibrium binding energy E_b, the diffusion barrier of interstitial iron E_m, and the dissociation energy of the pairs E_{diss}.

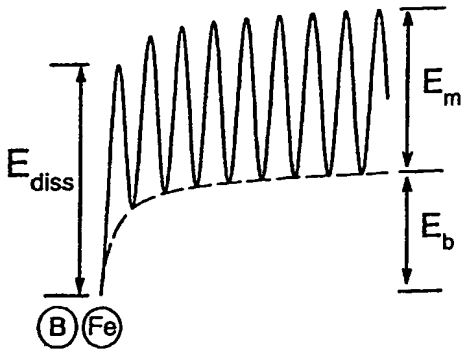

Fig. 11. An energy diagram of the FeB interaction in silicon (after Kimerling et al. [138]). E_{diss} is the dissociation energy of the pair, E_b is the equilibrium binding energy (a difference in equilibrium energy in the paired and unpaired states), and E_m is the diffusion barrier for iron. Note that $E_{diss} < E_b + E_m$, and that there is no straightforward manner to calculate one of the three parameters from the other two

The equilibrium binding energy E_b can be obtained from the analysis of the temperature dependence of the equilibrium fraction of Fe_i, paired with boron, as it follows from the law of mass-action:

$$\frac{N(\mathrm{FeB})}{N(\mathrm{Fe_i^+}) \times N(\mathrm{B_S^-})} = \frac{Z}{N_i} \exp\left(\frac{E_b}{k_B T}\right), \qquad (6)$$

where N_i is the density of interstitial sites in the silicon lattice (5×10^{22} cm^{-3}), and Z is the number of possible orientations of the pair with the same symmetry around one acceptor atom (4 for the tetrahedral symmetry). Note that (6) defines the equilibrium ratio of concentrations of FeB pairs, N(FeB), to the concentration of the ionized iron, $N(Fe_i^+)$, rather than to the total concentration of unpaired iron. The value of $N(Fe_i^+)$ is usually smaller than the total concentration of the unpaired iron, the ratio of the two being dependent on the doping level of the sample and the temperature. It is also important to keep in mind that the equilibrium binding energy determines the paired fraction of iron at equilibrium, i.e., after infinitely long equilibration time. The kinetics of the association/dissociation reactions are determined by E_m and E_{diss}.

The temperature dependence of the equilibrium fraction of paired iron was studied by Kimerling et al. [138,139], Lemke [90,170], Reiss et al. [141], and Wunstel et al. [80]. The reported binding energies vary from 0.45 eV [139] and 0.53 eV [80] to 0.6 eV [141,170] and 0.65 eV [90,138]. Wijaranakula [132] calculated a binding energy of 0.58 eV from the experimental data reported earlier by Nakashima et al. [77]. A scatter in binding energies reported by different groups can be partly ascribed to interaction of iron with other impurities, unintentionally introduced in silicon during studies. A careful re-examination of the pairing data using state-of-the-art silicon material and modern cleanroom facilities is required to obtain the binding energy with a better accuracy. Our own experience suggests that the true value of the binding energy lies in the range from 0.58 eV, as reported in [77,132,170], to 0.65 eV, as reported in [90,138]. That these values are close to the electrostatic binding energy $E_{ionic} = 0.52$ eV of a donor–acceptor pair is often used as an argument in favor of the model of ionic type binding of the FeB pair. However, a number of theoretical calculations

discussed in Sect. 2.6 strongly suggest that the binding between Fe_i and shallow acceptors, in particular boron, has not only ionic character, but also has either a covalent or a strain component.

2.1.4 Association kinetics of FeB *pairs.* The association kinetics of FeB pairs can be described [125,190] using the theories of diffusion-limited precipitation/trapping, developed by Ham [191], and of trapping of mobile donors by immobile acceptors, developed by Reiss et al. [146]. In the latter theory, a mobile ion is considered captured when the electrostatic attraction potential between the donor and the acceptor, $V(r)$, exceeds the average thermal energy, k_BT, i.e., $k_BT \leq V(R_C)$. Since in most cases R_C is as large as several nm, the interaction potential can be approximated by Coulombic attraction even for the mixed type of binding in the pair, and R_C is then obtained by solving the following equation:

$$k_BT = \frac{q^2}{4\pi\varepsilon\varepsilon_0 R_C} \exp\left[-R_C \Big/ \left(\frac{\varepsilon\varepsilon_0 k_BT}{q^2 p}\right)^{1/2}\right], \tag{7}$$

where p is the free hole density. For the doping levels $N_A \leq 10^{17}\,cm^{-3}$ and under extrinsic conditions, the screened Coulomb potential in (7) can be approximated by a simple Coulomb potential (i.e., the exponential term in (7) can be neglected), and the capture radius R_C can be obtained explicitly as $R_C = q^2/(4\pi\varepsilon\varepsilon_0 k_BT)$. Inserting this expression into the formula for the diffusion-limited precipitation time constant (Ham's law, [191]), which for the case of trapping of iron ions by boron has the form:

$$\tau_{ass} = (4\pi D(Fe_i) N_A R_C)^{-1}, \tag{8}$$

one can easily obtain [106,124,138,190]

$$\tau_{ass} = \frac{\varepsilon\varepsilon_0 k_BT}{q^2 N_A D(Fe_i)} \approx \frac{566.7 \times T}{D(Fe_i) \times N_A}, \tag{9}$$

where N_A is the concentration of shallow acceptors (in our case, boron) in cm^{-3}, T is the temperature in Kelvin, and $D(Fe_i)$ is the iron diffusivity in cm^2/s. Equations (8) and (9) assume that the interstitial iron concentration is much lower than that of the boron. Hieslmair et al. [190] showed that Ham's law [191] can be used to describe the association kinetics and obtained a capture radius of 5 to 6 nm at room temperature, in a good agreement with the theoretical prediction of approximately 4.5 nm from (7). Equation (9) was extensively used to determine the diffusion barrier of ionized iron at low temperatures. These studies were discussed in Sect. 1.3.2.2 and yielded strongly scattered values for the diffusion barrier from 0.58 eV to 0.81 eV.

2.1.5 Dissociation of FeB *pairs.* The dissociation kinetics of FeB are determined by the potential barrier E_{diss} for a jump of the Fe_i ion away from the first closest-neighbor position to the boron atom. The dissociation time constant is then given by:

$$\tau_{diss}^{-1} = \nu \exp\left(\frac{E_{diss}}{k_BT}\right), \tag{10}$$

where ν is the attempt frequency. Although it is quite straightforward to determine the dissociation barrier E_{diss} from the temperature dependence of dissociation reaction, we are aware of only two values reported in the literature: $E_{diss} = 1.17\,eV$ ($\nu = 1.8 \times 10^{10}\,s^{-1}$) [154], and 1.2 eV ($\nu = 5 \times 10^{10}\,s^{-1}$), reported by the same author in [157]. In the latter article, Feuchtinger studied "migration" of the FeB pairs, which clearly consists of dissociation of a pair, diffusion of iron to the next ionized boron, and re-association of the pair. The kinetics of the reaction is thus determined by the dissociation reaction. We want to emphasize that we did not find any indication that the process of re-association of iron–boron pairs (see Sect. 2.1.6) was properly taken into account during the dissociation studies in [154,157]. Thus, it can not be excluded that the dissociation energy may need to be re-evaluated.

Ostapenko and Bell [192,193] reported the dissociation of FeB pairs by using ultrasound. At 75 °C, about 25% of donor–acceptor pairs could be dissociated by ultrasonic treatment. It was suggested that the ultrasound vibrations can force a partial separation of Fe_i and B. This reduces the FeB pair binding energy and accelerates the process of complete pair dissociation.

The dissociation reaction of FeB pairs is also enhanced by minority carrier injection. Kimerling and Benton [138] reported that the dissociation reaction could be driven to greater than 95% completion by the injection of minority carriers at temperatures above 77 K. The dissociation rate of the pairs was reported to increase linearly with the injection current and was weakly temperature dependent with the activation energy of about 0.1 eV [139]. Minority carriers can be injected either by forward biasing p–n junctions (and even aluminum Schottky diodes), or by shining white light on the wafer. Light-stimulated dissociation of FeB pairs was first reported by Graff et al. [78] and is now routinely used in SPV systems [106]. The dissociation was carried out by focusing the light of a 50 W halogen lamp onto a 0.5-cm-diameter spot on the surface of the wafer [78]. The minority carrier injection-stimulated enhancement of dissociation of the pairs is explained as a recombination-enhanced defect reaction [194]. Examples of recombination-enhanced diffusion in silicon are enhancement of diffusion of interstitial aluminum in silicon [195] and the decrease of the barrier for migration of iron from the first-neighbor position in FeAl, FeIn, and FeB pairs to the second one [196–198]. Reaction rates that have been increased by 6 orders of magnitude using light were observed in other systems such as GaAs [199–201], GaP [202,203], and $GaAs_{1-x}P_x$ [204]. Weeks et al. [205] suggested that the energy released during the capture of a minority carrier at the defect and the recombination with trapped majority carrier is entirely converted to vibrations of the defect, reducing the apparent activation energy of the purely thermal annealing behavior or the diffusion of the defect. The attempt frequency of the reaction would correspond to the electron–hole recombination rate. The observed reduction of the activation energy of dissociation of about 0.8 eV would fit to a model of converting the electron capture energy of 0.77 eV on Fe_i^+ to defect vibrational modes. Further theoretical studies of nonradiative capture and multiphonon emission [206,207] (see also [208] for a review of non-radiative transitions in semiconductors) enabled Sumi [209,210] to develop a model of recombination-enhanced defect reactions that takes into account energy dissipation to the surrounding lattice.

2.1.6 FeB *pairing: analysis.* An important factor which is frequently neglected in analysis of reactions of FeB pairing and dissociation is that the rate of the observed reactions is determined by both the association rate $r_{ass} = \tau_{ass}^{-1}$ and the dissociation rate $r_{diss} = \tau_{diss}^{-1}$. In most studies the association or dissociation energies of the pairs were calculated from the temperature dependence of the reaction rate assuming that the reaction is either purely dissociation or purely association. This assumption is in most cases incorrect and may lead to substantial errors. This point can be illustrated by the analysis of a simple differential equation, describing the reaction kinetics. If we neglect the precipitation of iron, assume that most of the interstitial iron is ionized ($N(Fe_i) = N(Fe_i^+)$) and that the concentration of iron is much less than the concentration of boron, then the iron–boron pairing reaction is given by the following differential equation:

$$\frac{dN(FeB)}{dt} = r_{ass} \times (N(Fe_i) - N(FeB)) - r_{diss} \times N(FeB), \tag{11}$$

where $N(FeB)$ is the concentration of iron–boron pairs, and $N(Fe_i)$ is the concentration of ionized interstitial iron. The solution of this equation is given in the general case by

$$N(FeB) = \frac{r_{ass}}{r_{ass}+r_{diss}} N(Fe_i) - \left\{ \frac{r_{ass}}{r_{ass}+r_{diss}} N(Fe_i) - N_0(FeB) \right\} \times \exp(-(r_{ass}+r_{diss})t), \tag{12}$$

where $N_0(FeB)$ is the initial concentration of FeB pairs at the beginning of the measurement ($t = 0$). It is important that the reaction rate is always given by the sum of association and dissociation rates. Thus, the temperature dependence of the reaction rate is not necessarily determined by only the dissociation energy or only the diffusion barrier. The apparent activation energy of the reaction as reported in the literature may actually come out to be between the true dissociation and diffusion barriers. In this case, the apparent energy would depend on the doping level of the samples and the temperature range used in the studies. A complete description of the reaction kinetics should include the temperature dependence of the ionized fraction of iron [132,170,211,212] and the precipitation (agglomeration) rate of iron.

2.2 *Iron–aluminum pairing*

2.2.1 EPR studies of FeAl *pairs.* Unlike iron–boron pairs, which are stable only in ⟨111⟩ configuration, iron–aluminum pairs co-exist in two configurations. One of the first EPR studies of FeAl pairs was that of van Kooten et al. [213], who detected resonances associated with the trigonal and orthorhombic configurations of $(FeAl)^0$ pairs. Both spectra (see Appendix A) showed a sixfold splitting caused by the hyperfine interactions of iron with one Al nucleus. An additional twofold splitting appeared in the resonance of the orthorhombic $(FeAl)^0$ pair in the samples doped with iron enriched to 90% in the magnetic isotope ^{57}Fe. This clearly indicated the involvement of one iron and one aluminum atom in the paramagnetic center. The association and annealing behavior of the center is qualitatively similar to FeB pairs. After keeping the samples for one night at room temperature, the resonance of Fe_i disappeared and resonances of $(FeAl)^0$ pairs increased in intensity by about a factor of 3. Annealing at $T = 90\,°C$ for 1 h was found to be sufficient to dissociate the pairs [213]. Gehlhoff et al. [214] reported that there are actually two sets of EPR lines associated with the orthorhombic $(FeAl)^0$ pairs. They showed that these lines are caused by the spin transitions within an isolated quartet ground state with a zero-field splitting very large compared to the microwave quantum, and suggested to describe the lines using a single Hamiltonian with a spin $S = 3/2$ [214,215] (see Appendix A).

The initial EPR studies of van Kooten et al. [213] and Gehlhoff et al. [214] discussed above revealed only the resonance of the neutral charge state of ⟨111⟩ FeAl pairs. EPR resonances of negative, $(FeAl)^-$, and positive, $(FeAl)^+$, pairs with a trigonal symmetry have been found only recently by Gehlhoff and Irmscher [168,215,216] (see Appendix A). Whereas the spectrum of a neutral pair $(FeAl)^0$ could be easily observed in all samples containing Fe and Al, the appearance and intensity of the other two spectra were much more dependent on the sample preparation and illumination. The resonances associated with $(FeAl)^0$ and $(FeAl)^+$ were identified from the observed isotope splitting [166,215]. For the $(FeAl)^-$ pair such a straightforward proof was not possible because line broadening prevented the resolution of the hyperfine structures. It should also be noticed that Irmscher et al. [215] suggested that the trigonal (FeAl)-related spectrum reported earlier by Greulich-Weber et al. [217,218] and tentatively identified as $(FeAl)^0$ complex with the Fe_i^+ ion at the second nearest position from the Al atom along the ⟨111⟩ direction, is identical to the resonance, interpreted as $(FeAl)^+$ in [215]. Therefore, we listed both resonances in the same row in the table in Appendix A.

2.2.2 Electrical levels of FeAl *pairs.* The electrical levels of the ⟨111⟩ and ⟨100⟩ configurations of FeAl pairs were detected in electrical measurements even before they were observed by EPR. Feichtinger [154] and later Lemke [170] and Nakashima et al. [219] found from Hall effect and DLTS measurements that the concentrations of the electrically active Fe_i^+ and Al_S^- decreases within several hours after diffusion and quench of Fe_i in Al-doped silicon. Additionally, a level of FeAl pairs at $E_V + (0.20 \pm 0.01)$ eV appears in the band gap. The second energy level of FeAl pairs at $E_V + (0.13 \pm 0.01)$ eV was reported in [78,80,144,170,219,220]. It was shown that the pairing of interstitial iron with aluminum results in an increase of the concentration of the levels of FeAl and in a decrease of the concentration of the level of Fe_i, such that the sum of concentrations of all three levels remained constant [78]. Optical measurements using the photocapacitance method were in good agreement with the optical and thermal ionization energies of the level $E_V + 0.20$ eV [81]. Hole capture cross-sections were reported to be $\sigma_p = 2 \times 10^{-14}\,cm^2$ [220] and $\sigma_p = 4 \times 10^{-15}\,cm^2$ [80] for the level at $E_V + 0.20$ eV, and $\sigma_p = 6 \times 10^{-14}\,cm^2$ [220] for the level at $E_V + 0.13$ eV. The equilibrium binding energy of the FeAl center with $E_V + 0.20$ eV was reported to be 0.70 eV [170]. An analysis of the dependence of the hole emission rate on electric field in the depletion region of a Schottky diode revealed no significant shift in the position of the FeAl DLTS peaks [144] (as compared to the shift of 14 K, predicted by the Pool–Frenkel law for an acceptor level

in p-type silicon [221]), confirming that both configurations of FeAl pairs are donors.

Theoretical calculations for FeAl pairs are sparse. Weihrich and Overhof [222] predicted from ab initio calculations that the pair with orthorhombic symmetry should be stable in the negative and in the neutral charge states. Trigonal pairs were found stable in negative, neutral, and positive charge states and in two structural configurations: with Fe_i on the nearest and with Fe_i on the second-nearest interstitial position.

2.2.3 Metastability of FeAl *pairs.* The metastability of FeAl pairs was discovered in 1985, when Chantre et al. [144] associated the FeAl energy levels at $E_V + 0.20\,eV$ and $E_V + 0.13\,eV$ with the trigonal and orthorhombic configurations of FeAl pairs, respectively. They also showed that the pairs can rearrange from trigonal to orthorhombic configuration and back under the influence of an applied bias or light. This was explained as a single diffusion jump of Fe_i from a nearest neighbor position to substitutional aluminum (that corresponds to the trigonal symmetry of the pair) to a second-nearest neighbor position (that corresponds to the orthorhombic symmetry of the pair). They found that the relative amplitude of the two DLTS peaks of the FeAl pair depends on the cooling conditions of the sample before the DLTS scan, as shown in Fig. 12. Both DLTS peaks were present when the sample was cooled with a reverse bias. Cooling with a zero bias was found to eliminate the signal of the trap at $E_V + 0.13\,eV$, whereas the signal from the trap at $E_V + 0.20\,eV$ grew correspondingly. The kinetics of transitions between the two defect states revealed that the rate of transition from the metastable ($E_V + 0.13\,eV$) to the stable ($E_V + 0.20\,eV$) state is given by $1 \times 10^{11} \exp(-(0.50\,eV)/k_B T)$ (s^{-1}), whereas the rate of the reverse reaction is given by $5 \times 10^{12} \exp(-(0.64\,eV)/k_B T)$ (s^{-1}).

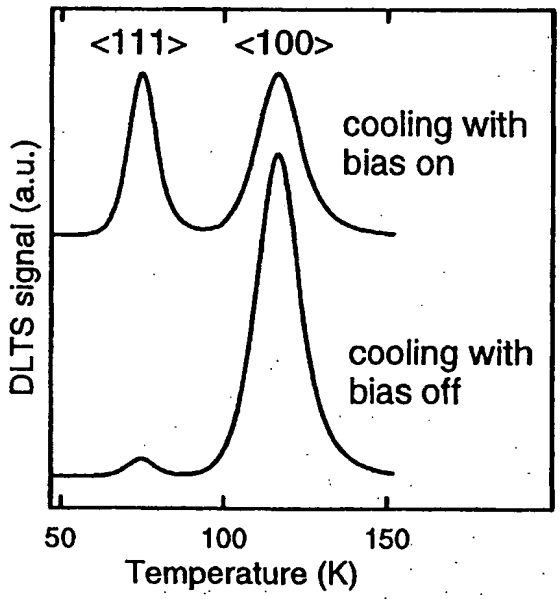

Fig. 12. The DLTS spectra of FeAl pairs in silicon. The amplitudes of the DLTS peak are associated with the stable and metastable states of the FeAl pair, and depend on the cooling conditions of the sample (after Chantre et al. [144]). The DLTS rate window is $1000\,s^{-1}$

Chantre and Bois [144] obtained a good quantitative agreement with the experimental data assuming that the interaction between iron and aluminum is fully described by the electrostatic attraction between them. Gehlhoff et al. [223] established unambiguous correlation between the deep levels detected by DLTS and EPR resonances. They showed that the metastable state can be populated not only by cooling down the sample with bias, but also by illuminating it during cooldown with above-band-gap light. This was explained as recombination-enhanced conversion from one to the other configuration of the pair.

More details of the metastable properties of iron–acceptor pairs can be found in Sect. 2.6.

2.3 Iron–gallium pairing

The EPR resonance parameters of the neutral $(FeGa)^0$ pair with a trigonal symmetry were reported by Ludwig and Woodbury [28,56]. The orthorhombic configuration of the FeGa pairs was detected by Gehlhoff et al. [214]. They detected two sets of EPR lines and proved that they are associated with the spin transitions within an isolated quartet ground state of the same center with a zero-field splitting very large compared to the microwave energy. The resonance was correlated with FeGa pairs from the well-resolved hyperfine structures [214]. Even the hyperfine splitting caused by the isotopes ^{69}Ga and ^{71}Ga could be distinguished both for the orthorhombic and the trigonal pair [214,224].

DLTS studies of electrical levels associated with iron in gallium-doped silicon initially revealed only one FeGa level at $E_V + 0.24\,eV$ [80,170] (see Appendix B). The equilibrium binding energy of this pair was reported to be 0.47 eV [170]. Optical measurements using the photocapacitance method revealed a level at $E_V + 0.24\,eV$ [81], in good agreement with the DLTS measurements. The hole capture cross-section of the FeGa center with a $E_V + 0.24\,eV$ level was reported to be $\sigma_p = 2 \times 10^{-14}\,cm^2$ by Wünstel et al. [80] and $\sigma_p = 3 \times 10^{-15}$ (at 120 K) by Lemke [170].

The bistability of iron–gallium pairs, similar to that of FeAl pairs, and the second energy level of FeGa pairs, was reported by Chantre and Kimerling [225]. In addition to the previously reported level of FeGa pairs at $E_V + (0.23 \pm 0.01)\,eV$ [80,170], they reported a metastable level at $E_V + 0.14\,eV$ [225]. The elastic energy barriers for the transformation from the metastable to the stable position and back were found to be about 0.5 eV and 0.6 eV, respectively.

2.4 Iron–indium pairing

2.4.1 EPR identification of FeIn *pairs.* The EPR signal of FeIn pairs in silicon with a ⟨100⟩ symmetry was reported in 1962 by Ludwig and Woodbury [28] (see Appendix A). Later experiments by Gehlhoff et al. [226,227] using isotope splitting confirmed the assignment of this spectrum to FeIn pairs. In contrast to FeB, FeAl, and FeGa pairs, the stable configuration of FeIn pairs was found to be orthorhombic. EPR identification of the metastable trigonal configuration of FeIn pairs was made by Omling [228,229] (see Appendix A). The metastable trigonal FeIn signal was shown to appear in the EPR spectrum of p-type samples only if they were illuminated with photons of $h\nu > 0.5\,eV$. Later, one more resonance associated with the trigonal FeIn complex was found by

Gehlhoff et al. [226,230,231]. From the temperature dependence of the intensity of the EPR signals, they concluded that the spectrum originally detected by Ludwig and Woodbury originated from an excited state, while the newly discovered resonance is consistent with the ground state of the pair.

An EPR resonance tentatively assigned to the positive charge state of the orthorhombic FeIn center was found by Gehlhoff et al. [227,232] (see Appendix A). The negative charge states of the FeIn complexes have not yet been found by EPR, but have already been detected by FTIR, as discussed below.

2.4.2 Electrical and optical properties of FeIn *pairs.* The electrical levels of the stable orthorhombic and metastable trigonal configurations of FeIn pairs were detected using DLTS by Chantre and Kimerling [225], who reported FeIn-related levels at $E_V + 0.15$ eV and $E_V + 0.27$ eV. The elastic energy barrier for the transformation from metastable state to the stable configuration and back were found to be about 0.5 eV and 0.6 eV, respectively.

Tidlund et al. [233–235] studied excitation spectra of FeIn pairs using FTIR and found a FeIn-related set of two lines at about 6100 cm^{-1} ($\approx$ 760 meV) and a considerably weaker set of 6 lines at about 6600 cm^{-1} ($\approx$ 820 meV). They associated these sets of lines with the orthorhombic and trigonal configurations of FeIn pairs, and estimated the positions of the $(FeIn)^{-/0}$ acceptor levels to be $E_C - 0.39$ eV and $E_C - 0.32$ eV.

Reislohner [236] applied perturbed angular correlation spectroscopy (PAC, see [237]) to FeIn complexes and found three different configurations of FeIn pairs. One of the configurations corresponded to the ⟨111⟩ orientation of the pair; the second one was tentatively assigned to the ⟨100⟩ orientation. The third configuration did not show any definite orientation dependence and was assigned to a complex with a large number of equivalent orientations, such as a pair in a ⟨311⟩ orientation. All pairs annealed out at $T > 200$ °C. The upper limit of the dissociation barrier of the complex was estimated to be $E_D(FeIn) < 1.4$ eV [236].

In contrast to other Fe–acceptor pairs, calculations for the FeIn pairs based on simulations of the potential energy profiles using Lennard–Jones potentials and electrostatic interactions, suggested that the second-nearest to In interstitial position of Fe_i in the ⟨111⟩ direction is more stable than the nearest-neighbor position for the neutral and positive charge state of the pair [238]. Since the interaction with the ^{29}Si ligands could not be resolved by EPR measurements [229] and since both interstitial sites are consistent with the observed trigonal symmetry, it is not possible to distinguish these two arrangements by EPR. However, Gehlhoff et al. [224] argued that since the trigonal crystal fields estimated from the measured g-values [239] are approximately the same for FeAl and FeIn, the assumption that Fe ion can be in the second interstitial position in ⟨111⟩ direction seems to be very improbable.

2.5 Iron–thallium pairing

Thallium is one of the possible p-type dopants in silicon. However, to the best of our knowledge, there are no data on electrical levels or binding energies of FeTl pairs, primarily due to the scarcity of thallium-doped silicon samples. The data on iron–thallium complexes are limited to a few photoluminescence (PL) studies [240–242]. The position of the PL lines associated with FeTl was reported to be around 1.086 eV, measured at liquid helium temperature. The Si:Tl luminescence at 1.086 eV was found to vanish completely above 12 K, being replaced by a similar set of lines at 1.049 eV. This led the authors of [242,243] to suggest that the complex can exist in two different configurations. The trigonal structure of the Si:Tl luminescent center, suggested by Sauer and Weber [244], was later confirmed by means of detailed stress and Zeeman studies by Watkins et al. [245] and Conzelmann et al. [246]. They also showed that the high-temperature center shows a reduction in symmetry, possibly to an orthorhombic configuration with ⟨100⟩ symmetry.

The intensity of the PL lines in Si:Tl spectrum was greatly enhanced if the samples were heated to at least 800 °C and then quenched. Even a short anneal for several seconds was sufficient to activate the centers [241,242,247]. Schlesinger and McGill [248] reported that the intensity of the PL lines in Si:Tl samples increases with increasing Fe_i concentration, which can be considered an indication that iron is a part of this complex.

Despite the apparent agreement on the identification of the FeTl PL signal in the above-mentioned references, we would exercise caution with respect to these data since the identification of the PL spectra initially attributed to the other, better investigated iron–acceptor pairs remains highly controversial and even contradictory, as it will be discussed in Sect. 6.

2.6 General trends in iron – shallow acceptor pairing

2.6.1 General picture of pairing and dissociation of iron–acceptor pairs. Although there is a wide disagreement between different research groups about the binding energies of the iron–acceptor pairs, the qualitative picture of their association and dissociation kinetics is well established. After a fast quench, iron is predominantly interstitial and is strongly supersaturated since its equilibrium solubility at room temperature is vanishingly small. Shallow acceptors are effective trapping sites for iron around room temperature in p-Si due to electrostatic attraction between the negatively charged acceptors and the positively charged iron ions. Thus, iron–acceptor pairs are formed within several hours to several days at room temperature depending on the average distance between the ionized iron and the acceptor atoms. Annealing of the sample at temperatures above 200 °C dissociates the pairs. As observed from EPR and DLTS measurements, complexing of iron in p-type silicon exhibits three phases. The temperatures of the transition between phases are similar for all p-type dopants [81,91,132,148,149,174,211,249]. In phase I, at temperatures below 80 °C to 100 °C, the concentration of interstitial iron either decreases as the pairs are formed, or remains at a very low level. In phase II, at temperatures between 100 °C and 200 °C, a recovery of the Fe_i species and a reduction in the concentration of the Fe–acceptor pairs is observed [250] (see Fig. 5). The temperature at which the maximum concentration of ionized interstitial iron is achieved depends on the doping level [249]. The pairing and dissociation processes in phases I and II are reversible. In phase III, at temperatures above 200 °C, acceptors can not provide stable traps for iron and iron diffuses towards more stable sinks such as surface defects or dislocations where it

precipitates/agglomerates [52]. The concentrations of both Fe_i and Fe–acceptor pairs decrease as the isochronal annealing temperature increases and do not recover after the end of the anneal [142].

2.6.2 Type of binding in the pairs. The role of electrostatic and covalent bonding in iron–acceptor pairs is one of the most intensely discussed iron-related fundamental topics. There is extensive experimental evidence that the electrostatic attraction between Fe_i^+ and negatively charged substitutional shallow acceptors is a driving force for the formation of iron–acceptor pairs. This was confirmed by the comparison of the pairing rate of iron in p-Si and in n-Si partly compensated with boron. No pairing was reportedly observed in bulk of n-Si even after a year [90,103,138]. Similarly, no pairing was observed in the space-charge region of a reverse-biased Schottky diode on p-Si where interstitial iron is neutral even after 15 days [90]. These observations are frequently used as an argument in support of the ionic type of binding in the pairs. Ludwig and Woodbury [28] applied the ionic model to explain the EPR resonances of iron–acceptor pairs. They suggested that the resonance of the metal–acceptor pair is associated with the $3d$ shell of the metal in the electrostatic field due to the negatively charged acceptor. Although this model was quite successful in explaining EPR spectra of the pairs, the assumption that the complex stabilizes as an ionic pair was questioned by Assali, Leite et al. [251–257]. In theoretical calculations of the electron structure of iron–acceptor pairs made using a $25Si + B_S Fe_i$ cluster and based on the multiple-scattering $X\alpha$ formalism within the framework of the Watson-sphere-terminated molecular-cluster model, they concluded that the covalent bonding effects play a basic role in determining the physical properties of iron–acceptor pairs and include, besides Fe and B, the silicon atoms nearest to the pair. In agreement with Assali et al. [252–255], Sugimoto and Seki [258] showed from ab initio molecular orbital model calculations that iron loses 0.37 electrons during formation of FeB pairs. However, this charge is transferred to the surrounding silicon atoms rather than to the substitutional acceptor, which implies that there is no direct covalent bond between iron and boron. Instead, Fe is weakly bound to the silicon atoms next to boron. In contrast to the above mentioned studies, recent ab initio total-energy computations of Overhof and Weihrich [259,260] did not reveal any covalent bonding between Fe_i and B_S. In the framework of their model Weihrich and Overhof [260,261] also calculated parameters of the hyperfine interactions for iron–acceptor pairs, and obtained a good agreement with the experimental data. It is not yet clear what the reason is for this major disagreement in the theoretical calculations discussed above.

2.6.3 Two configurations of the pairs and their bistability. EPR studies discussed in Sects. 2.1.1, 2.2.1, 2.3, 2.4 revealed that Fe–acceptor pairs have two structural configurations, with trigonal and orthorhombic symmetry. Each of these configurations may exist in negative, neutral, and positive charge states. This results in up to 6 different EPR resonances (which may each consist of two groups of lines corresponding to upper and lower Kramers doublets) and up to 4 deep levels for each Fe–acceptor pair. Interstitial iron occupies the first nearest-neighbor interstitial sites adjacent to acceptors along the ⟨111⟩ direction in the pairs with trigonal symmetry, and the second nearest-neighbor interstitial sites adjacent to acceptors along the ⟨100⟩ direction in pairs with orthorhombic symmetry. Both orientations of the pairs were observed at room temperature in Al, Ga, and In-doped samples, whereas the orthorhombic configuration of the FeB pair was only tentatively identified by capacitance spectroscopy methods after minority carrier injection at $T = 150$ K [86,172,187–189]. The experimental observation that FeB, FeAl, and FeGa pairs are stable in the trigonal configuration, whereas FeIn prefers orthorhombic configuration is in agreement with the calculations of Kimerling [238], who explained the instability of ⟨111⟩ configuration for FeIn as a result of competition between repulsive (elastic) and attractive (electrostatic) energy terms, and with the ab initio molecular orbital method calculations of Sugimoto and Seki [258].

The co-existence of two possible structures of the pairs results in the bistability of the Fe–acceptor complexes. The metastability and bistability of defects is a well-known phenomenon in semiconductor physics [262–265]. The two configurations of the Fe–acceptor pairs can be viewed as two energy wells separated in a configuration space by a potential barrier (Fig. 13). While this model can be applied to all iron–acceptor pairs, the energies are different for different acceptors. The experimentally determined potential barriers separating the stable and metastable configurations of FeB, FeAl, FeGa, and FeIn pairs in both neutral and positive charge states (see Fig. 13), and the barriers calculated using the electrostatic model of the pairs, are presented in Table 1. The configuration with the lowest total energy will have the highest population at equilibrium. Relative populations of the states with the ⟨111⟩ and ⟨100⟩ symmetries are given by $N(\langle 111\rangle)/N(\langle 100\rangle) = \exp(\Delta E(0)/k_B T)$ for the neutral charge state of the pairs, and $N(\langle 111\rangle)/N(\langle 100\rangle) = \exp(\Delta E(+)/k_B T)$ for the positive charge state. Since $\Delta E(0) \neq \Delta E(+)$, the relative population

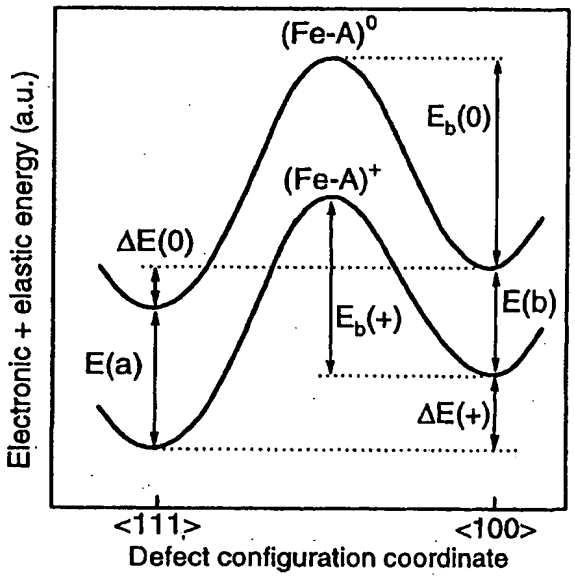

Fig.13. A configuration-coordinate diagram of the bistable iron–acceptor pairs in silicon. The FeB, FeAl, and FeGa pairs have a lower sum of the electronic and elastic energies in ⟨111⟩ configuration than in ⟨100⟩ configuration (as shown in the figure), whereas FeIn pairs have a lower equilibrium energy in the ⟨100⟩ configuration than in the ⟨111⟩ configuration. The notations in the figure are explained in the text and in the caption to Table 1

Table1. The parameters of the bistable states of complexes of iron with shallow acceptors, calculated using the ionic model, and determined experimentally. The notation follows that of the configuration coordinate diagram Fig. 13 and is as follows: E_b is the binding energy of the pairs; $E(a)$ and $E(b)$ are the hole emission activation energy in two states of the defect (⟨111⟩ and ⟨100⟩ orientation, respectively); $\Delta E(0)$ and $\Delta E(+)$ are the differences in equilibrium energies of the ⟨100⟩ and ⟨111⟩ configurations of the iron–acceptor pair in neutral $(Fe-A)^0$ and positive $(Fe-A)^+$ charge states, respectively; $E_b(0)$ and $E_b(+)$ are the potential barriers for the jump of a positively charged Fe_i^+ (total charge state of the pair $Fe_i^+A_S^-$ is neutral) and doubly positively charged Fe_i^{2+} (total charge state of the pair $Fe_i^{2+}A_S^-$ is positive) ions from the metastable to the stable position. The value of $E_b(0) = 0.62$ eV, predicted from the ionic model, was calculated as $E_b(0) \approx E_m - \Delta E(+)/2$, where E_m is the migration barrier of Fe_i^+. $E_b(+)$ can not be predicted from the ionic model since the diffusion coefficient of doubly positively charged iron is unknown

Pair	E_b/eV	$E(a)$/eV (⟨111⟩)	$E(b)$/eV (⟨100⟩)	$\Delta E(0)$/eV	$\Delta E(+)$/eV	$E_b(+)$/eV	$E_b(0)$/eV
Ionic model	0.52 [144]	N/A	N/A	0.071 [144]	0.142 [144]	N/A	N/A
FeB	0.45 [139] 0.53 [80] 0.58 [132] 0.60 [141,170] 0.65 [90,138]	0.10 [78,80,91,92,124,157]	0.07 (?), [86,186]	?	?	?	?
FeAl	0.70 [170]	0.20 [144,225] 0.20 [223]	0.13 [144,225] 0.13 [223]	0.07 [144,225] 0.02 [223] 0.07 [148,149]	0.14 [144,225] 0.09 [223]	0.50 [144,225] 0.51 [223]	0.64 [144,225] 0.64 [223] 0.75 [148,149]
FeGa	0.47 [170]	0.23 [80,170,225]	0.14 [225]	0.04 [225] 0.03 [148,149]	0.13 [225]	0.5 [225]	0.6 [225] 0.72 [148,149]
FeIn	?	0.27 [225]	0.15 [225]	−0.13 [225] −0.09 [148,149]	−0.01 [225]	0.5 [225]	0.6 [225] 0.69 [148,149]

of the stable and metastable configurations can be altered by controlling the charge state of the pairs. This is done in DLTS experiments by changing the bias applied to the sample during cool down. The relative concentration of the pairs in each of the two configurations, and the values of $\Delta E(0)$ and $\Delta E(+)$ can be evaluated from the height of DLTS peaks. Assuming a purely electrostatic interaction between Fe_i and acceptors, one easily calculates the characteristic energies $\Delta E(0)$ and $\Delta E(+)$ of the pair [144] as 0.071 and 0.142 eV, respectively. These values are in relatively good agreement with the parameters of FeAl and FeGa pairs (Table 1). In contrast, the simple ionic model fails completely in describing the energetics of the FeIn and FeB systems [225]. Apparently, in these cases either the strain associated with the oversized In_S or the undersized B_S, or covalent bonding, play a significant role in determining the defect properties.

2.6.4 Energy levels of iron–acceptor pairs. The donor energy levels of iron–acceptor pairs were discussed in Sect. 2.1–2.3 and are summarized in Table 1 and in Appendix B. Two trends are observable. First, the ⟨111⟩ configuration of the pair always has a deeper level in the band gap than the ⟨100⟩ configuration. The second trend is that the levels become deeper with the increasing tetrahedrally coordinated covalent radius of the acceptors (88 pm for B, 126 pm for Al, 126 pm for Ga, and 144 pm for In, [266]), the ionic radius of the acceptors (35 pm for B, 39 pm for Al, 47 pm for Ga, and 62 pm for In, [267]), and the increasing ionization energies of the shallow acceptors (B (44.3 meV) to Al (68.5 meV), Ga (72.7 meV), In (156 meV), [81]). The dependence of the energy levels of the pairs on the acceptor ionization energy was fitted by a straight line by Lemke [170], who also pointed out that a similar dependence was observed for Mn–acceptor and Cr–acceptor pairs. We found, however, that a much better linear fit can be achieved if the donor energy levels of iron–acceptor pairs are plotted versus covalent radius of the acceptors, as presented in Fig. 14. Recent theoretical calculations, which took into account the lattice relaxation due to the difference in size of shallow acceptors and that of the silicon atoms, enabled Zhao et al. [268] to obtain a fair agreement of the calculated energy levels with the experimental data. The importance of lattice strain, particularly with respect to the pairs of Fe_i with the largest of acceptors, In, was also pointed out earlier by Benton [263]. She suggested that the stability of the FeIn complex in the configuration with iron in the second nearest position can be explained as a competition between the attractive electrostatic forces and the repulsive strain effects.

Theoretical calculations of the energy position of the acceptor levels of Fe–acceptor pairs [257], using multiple-scattering $X\alpha$ formalism predicted the values of $E_C - 0.20$, $E_C - 0.14$, and $E_C - 0.10$ eV for FeB, FeAl, and FeGa pairs in the ⟨100⟩ symmetry, respectively. The values of $E_C - 0.32$ and $E_C - 0.31$ eV were predicted for the ⟨100⟩ configura-

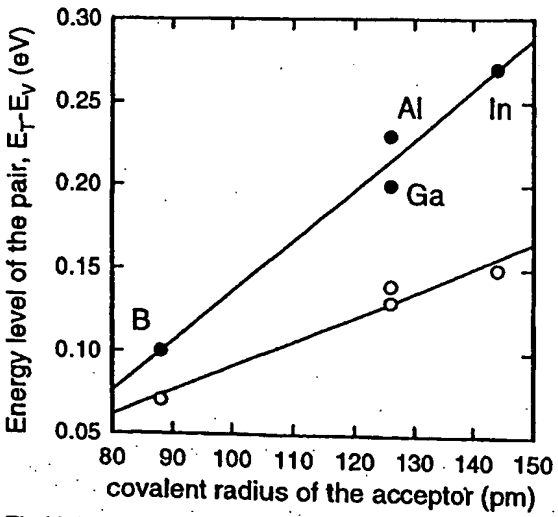

Fig.14. The dependence of the hole ionization energy on the covalent radii of shallow acceptor impurities. The *filled* and *open circles* correspond to the upper and the lower donor levels of the iron–acceptor pairs, respectively

tions of the FeAl and FeGa pairs, respectively [257]. These values agree quite well with the experimental data presented in Appendix B.

3 Pairing of interstitial iron with shallow donors

Phosphorus is the most common n-type dopant, and its reactions with iron, if they exist, are very important in order to understand the behavior of iron in n-type silicon and phosphorus diffusion gettering of iron [269]. The literature data on iron–phosphorus pairing are contradictory and inconclusive. Overhof and Weihrich [259] inferred from ab initio total energy calculations that the trigonal Fe_iP_S pair is stable in n-type samples in the negatively charged state $Fe_i^{2-}P_S^+$. They found that the pairs should be diamagnetic and therefore EPR inactive. However, there is no convincing experimental evidence for the existence of such pairs. Takahashi et al. [270,271] reported that the concentration of the interstitial iron detected in n-Si after diffusion and slow cool decreased with increasing phosphorus doping level. This was interpreted as formation of stable FeP pairs with the binding energy of 0.9 eV [270,271]. Conversely, Lee et al. [272] reported that isochronal annealing for 30 min at temperatures of up to 500 °C did not change the intensity of the EPR line of the P donor even after Fe_i^0 disappeared completely at 200 °C. Therefore, they argued that Fe_i^0 does not have a high probability of forming pairs with phosphorus. Höhne et al. [273] noted that in samples containing a sufficiently high concentration of phosphorus or arsenic (more than roughly 10^{15} cm^{-3}), the Fe_i^0 EPR line exhibited a satellite structure of four lines. The structure of the satellites was found to be isotropic, and their intensities were found to increase with increasing P concentration. Doping of the same samples with ^{57}Fe isotope resulted in the splitting of both the central Fe_i^0 line and the satellites. A spin–spin interaction between iron and phosphorus (or arsenic) could explain the positions of the satellites. However, the spin–spin interaction was not as large as usually observed for close partners. To explain this phenomenon, Höhne et al. [273] suggested that they observed a local random or almost random distribution of Fe_i^0 with respect to shallow donors, which implies that close pairs of Fe_i^0 and shallow donors do not form [273].

It is appropriate to emphasize that no electrostatic attraction, which is the main driving force for the formation of iron–acceptor pairs, can arise between iron and phosphorus. This is because phosphorus is positively charged whereas iron is either neutral or positive. Studies of phosphorus diffusion gettering also do not provide indications of the existence of stable FeB pairs. While the formation of phosphorus–impurity pairs is considered one of the physical processes involved in phosphorus diffusion gettering, evidence that such a pairing does exist was obtained primarily for gold [274–277], which is known to form both donor and acceptor levels in the band gap.

4 Complexes of iron with other impurities

4.1 FeAu *complexes*

The first reports on the formation of FeAu pairs were made by Feichtinger [157] and Lee et al. [272] in 1979. Feichtinger [157] concluded from his EPR studies that the resonances of both Fe_i^0 atoms and FeB complexes are strongly suppressed in Au-diffused samples. Lee et al. [272] found a new EPR spectrum with a trigonal symmetry which appeared after a 30-min anneal at 200 °C of Fe and Au co-diffused samples. The same resonance was also detected in a sample left at room temperature for a month. The spectrum was an order of magnitude stronger in p-type samples than in n-type samples and appeared only after cross-contamination of samples with iron and gold. The detailed EPR studies of Kleinhenz et al. [278] and Sieverts et al. [279] confirmed the existence of hyperfine interactions with the Au nucleus and revealed an additional twofold splitting of each line due to the hyperfine interaction with ^{57}Fe nuclei [278]. The FeAu center could be annealed out at $T = 300$ °C [250,272,278]. Since gold is known to dissolve in silicon substitutionally, the FeAu pair is thought to consist of a substitutional gold atom and an interstitial iron atom.

Studies of n- and p-type silicon samples co-diffused with Fe and Au using conductivity and Hall effect techniques revealed a level at about $E_V + (0.4$ to $0.5)$ eV, which was tentatively assigned to the FeAu complex [157]. The same level at $E_V + 0.434$ eV was observed in n-Si by Brotherton et al. [280], who used photocurrent DLTS, a modification of the minority-carrier spectroscopy, described in [281]. This level could also be detected in p-Si. Measurements using a combination of DLTS and EPR [280], and DLTS alone [282], confirmed that the changes in the concentration of FeAu pairs during anneals anticorrelate with the concentration of gold. DLTS studies confirmed that the intensity of the FeAu DLTS peak could be substantially increased by a 30-min anneal at $T = 200$ °C to 250 °C, whereas anneals at $T > 350$ °C dissociated the pairs [272,280].

Photo-EPR of n-Si:Fe:Au proved the existence of an acceptor level of these pairs in the upper half of the band gap [283]. DLTS investigations of the same sample revealed a level of FeAu pairs at $E_C - 0.33$ eV. The annealing kinetics of the DLTS line matched that of the EPR resonance. Lemke [284] also observed the FeAu related level at $E_C - 0.35$ eV ($\sigma_n = 3 \times 10^{-15}$ cm^2 at $T = 160$ K). Brotherton [280] reported very close values of $E_C - 0.354$ eV, $\sigma_n = 2 \times 10^{-15}$ cm^2, measured at $T = 80$ K to 160 K. A Fe-related level with the same activation energy in n-Si was reported by Kimerling [124], although no connection to gold was established.

The first theoretical model of the FeAu center, suggested by Kleinhenz et al. [278] and Sieverts et al. [279], was based on the ionic model of Ludwig and Woodbury [28]. According to this model, the observed EPR signal comes from a magnetic coupling between the angular momenta of gold and iron. It was speculated [278] that a much higher electronegativity of gold compared to that of iron makes the transfer of one electron from the iron to the gold likely, making the center $Fe_i^+Au_S^-$. Strong antiferromagnetic coupling between Au_S^- ($S = 1$) and Fe_i^+ ($S = 3/2$) should result in a total effective spin of $S = 1/2$, in agreement with experimental data. However, a theoretical analysis by Assali et al. [285,286] suggested that the FeAu pairs are formed by a covalent mechanism that includes the silicon neighbors in addition to Au_S and Fe_i. According to their model, the $S = 1/2$ spin of the center is related to a molecular orbital spread out over the entire cluster rather than being derived from the interactions between two localized magnetic centers.

The experimentally observed energy levels are in a very good agreement with the energy levels at $E_V + 0.45$ eV and $E_C - 0.35$ eV, predicted by Overhof and Weihrich [287] for the trigonal $(FeAu)^{0/+}$ and $(FeAu)^{-/0}$, respectively, from self-consistent ab initio total energy calculations. The same authors [259,287] predicted a covalent binding energy of the $(FeAu)^{0/+}$ pair of about 1.2 eV, and about 1.0 eV for the negatively charged pair. Theoretical calculations for a hypothetical FeAu pair with orthorhombic symmetry resulted in a binding energy lower than that of the trigonal pair by 0.3 eV. This difference in energy would result in about 1000 times lower equilibrium concentration of the orthorhombic pairs at room temperature.

The dissociation energy (E_{diss} in Fig. 11) of FeAu pairs was determined in the temperature range $T = 350\,°C$ to 400 °C by Weber and Wiehl [283], who found that $\tau_{diss} = 4.7 \times 10^{-3} \exp((0.73\,eV)/k_B T)$.

Experimental evaluations of the equilibrium binding energy of FeAu pairs proved to depend drastically on the model used for the pairing reaction. Lemke [284] studied equilibrium concentrations of unpaired Fe_i, Au_S, and complexes FeAu in the temperature range between 250 °C and 400 °C in n-type Si and obtained the dependence

$$\frac{N(\mathrm{AuFe}) \times N_i}{N(\mathrm{Au_S}) \times N(\mathrm{Fe_i})} = \exp\left(\frac{0.75\,\mathrm{eV}}{k_B T}\right). \tag{13}$$

His calculations were based on a formulation of the mass-action law (13) that does not account for the different charge states of iron and gold, i.e., assumes that the pairing reaction is charge-state independent. Brotherton et al. [288] argued that since the driving force for formation of FeAu pairs is the electrostatic attraction between Fe_i^+ and Au_S^-, the product of the total concentrations of gold and iron $N(\mathrm{Au_S}) \times N(\mathrm{Fe_i})$ in the mass-action law (13) should be substituted by the concentrations of the ionized impurities $N(\mathrm{Au_S}^-(T)) \times N(\mathrm{Fe_i}^+(T))$, where T is the temperature. This treatment resulted in a binding energy of 1.22 ± 0.02 eV. We want to emphasize that the difference in the binding energies reported by Lemke [284] (0.75 eV) and Brotherton et al. [288] (1.22 eV) stems from the different interpretation of the experimental data rather than from a difference in the data points themselves, as can be seen in Fig. 15. In this figure, we plotted the ratio $N(\mathrm{AuFe})/N(\mathrm{Au_{total}})N(\mathrm{Fe_{total}})$ from the work of Lemke [284] and the same ratio calculated using the data of Brotherton et al. [288]. There is a reasonably good agreement between both authors, with the exception of three data points obtained by Brotherton et al. [288] at low temperatures, where the kinetics of the reaction are so slow that the equilibrium concentration of FeAu pairs might not be achieved. Since the acceptor level of Au ($E_C - 0.55$ eV) lies above the donor level of Fe ($E_V + 0.385$ eV), for any position of Fermi level either Fe or Au or both of them will be neutral. It is easy to calculate that only a small fraction of either gold or iron (less than 20% at 650 K, and less than 1% at 400 K, [288]) will be ionized at any temperature. Low fractions of Fe_i^+ and Au_S^- will not negate the pairing reaction between iron and gold. As long as some percentage of gold and iron is ionized, the reaction will go to equilibrium, albeit slowly.

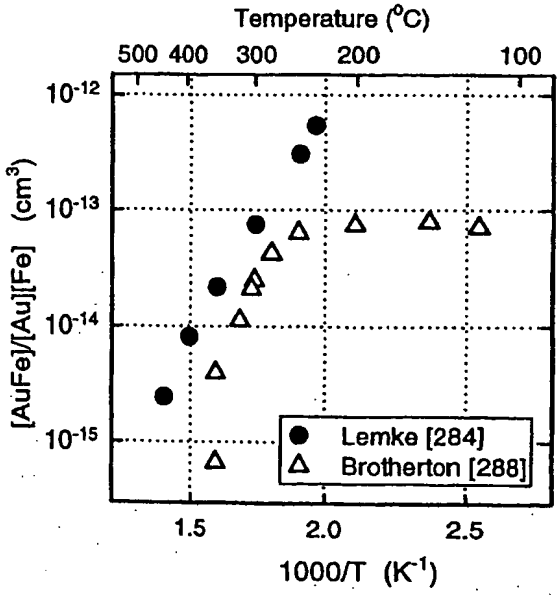

Fig. 15. The temperature dependence of the ratio of the equilibrium concentration of the iron–gold pairs to the product of the concentrations of unpaired iron and gold (after Lemke [284] and Brotherton et al. [288])

A question remains whether a pairing reaction between neutral iron and neutral gold is viable. Such a reaction is only possible if the binding in the pairs is covalent, as suggested in [259,287]. Although the capture radius of neutral Fe by a trapping site (for example, by gold) (about 0.235 nm, the nearest distance between interstitial and substitutional atoms in Si) is about 20 times less than that of the Fe_i^+ (about 5 nm, see [190]), the density of neutral iron and gold are much higher than that of the ionized ones. Thus, reactions between both charged and uncharged impurities may eventually need to be taken into account in a complete model.

4.2 FeAg, FePd, FePt, *and* FeZn *complexes*

Iron–silver complexes are very poorly investigated. To the best of our knowledge, there are no experimental data on electrical levels or on the microscopic structure of FeAg pairs, although theoretical calculations predict that these pairs should be stable. Overhof et al. [287] predicted two electrical levels for FeAg pairs in the band gap, at $E_V + 0.19$ eV for $(FeAg)^{0/+}$, and $E_C - 0.27$ eV for $(FeAg)^{-/0}$ from ab initio calculations. They also found that the positive, neutral, and negative charge state of the pair should have a spin $S = 0$, $S = 1/2$, and $S = 1$, respectively. In the following paper, Overhof et al. [259] concluded that the type of binding in FeAg pairs is predominantly covalent.

The electronic structures of FePd and FePt complexes were studied by EPR by van Oosten et al. [289] (see Appendix A). After diffusion of iron into platinum-doped silicon, the EPR signal of platinum was no longer observed, but a strong signal of trigonal FePt centers appeared. The FePt resonance exhibited large hyperfine satellites due to the ^{195}Pt isotopes. After co-diffusion of Pt and ^{57}Fe, a well-resolved hyperfine splitting was observed. A similar trigonal spectrum with hyperfine splitting due to ^{57}Fe was observed in palladium-diffused samples. Alves et al. [290] have recently reported that an intensive 777 meV luminescence line was observed in n-type samples known to have some Fe contamination and speculated that this line may be due to FePt complexes.

Czaputa [291,292] studied DLTS spectra of Si samples after Pd and Fe diffusion and established a correlation of Fe and Pd concentrations with the level at $E_C - 0.32$ eV, which he attributed to Fe_iPd_S pairs. He found that anneals at $T = 110$ °C could convert the palladium-related peak at $E_C - 0.22$ eV into the peak at $E_C - 0.32$ eV, whereas anneals at around 300 °C stimulated the reverse reaction. The activation energy for dissociation of this FePd complex was found to be about 1.5 eV. Co-diffusion of Fe and Pd in *p*-type silicon resulted in a new DLTS peak at $E_V + 0.52$ eV, which has similar formation and annealing kinetics as the FePd complex detected in *n*-Si. No detailed studies of this defect were reported; it was only suggested that this defect may be due to a different charge state of the same defect [292]. Höhne and Juda [293] reported that the co-diffusion of iron and platinum in silicon suppressed the formation of platinum complexes consisting of 6 platinum atoms [294], although they could not provide any explanation for this phenomenon.

FeZn complexes were reported, to the best of our knowledge, only in [295] by Lemke, who found two new energy levels with $E_V + 0.17$ eV and $E_C - 0.47$ eV in DLTS spectra obtained after diffusion of iron in *n*- and *p*-type silicon co-doped with zinc. He also reported that the level at $E_C - 0.47$ eV did not dissociate after annealing at 200 °C for 5 min and suggested that it is formed by doubly negatively charged zinc and singly positively charged iron: Fe^+Zn^{2-}.

4.3 FeS *complexes*

Three EPR resonances attributed to FeS pairs were reported by Ludwig [296] in 1965. The resonances observed in phosphorus-doped, undoped, and boron-doped silicon starting material were labeled FeS(I), FeS(II), and FeS(III), respectively. From the dependence of their intensity on the doping level of the samples, Ludwig [296] suggested that FeS(I), FeS(II), and FeS(III) are associated with the negative, neutral, and positive charged states of the same FeS complex. The presence of Fe was proven by doping with ^{57}Fe, whereas the participation of S was inferred from the fact that the FeS pairs did not appear in crystals not contaminated with sulfur. Later, Schirmer [297] reported one more FeS-related EPR signal, FeS(IV). They found that after a fast quench, only the EPR resonances of Fe_i^0, P^0, S^+, and $(S-S)^+$ were observed. After several days of storage at room temperature, the Fe_i^0 intensity decreased by about a factor of 100 and the FeS (IV) lines appeared in the spectrum. Also the $(S-S)^+$ intensity decreased, pointing out that the signal FeS(IV) may be due to S–Fe–S complexes. The center could be dissociated by above-band gap light. To the best of our knowledge, there are no data on the energy levels of these centers in the literature.

4.4 *Interaction of iron with oxygen and carbon*

Czochralski-grown (CZ) silicon contains oxygen and carbon in very high concentrations (between approximately 5×10^{16} cm^{-3} and 10^{18} cm^{-3}). Although the understanding of the interaction of iron with carbon and oxygen is of major importance for the characterization of iron in silicon, there are only a few experimental studies on this subject which are contradictory. For example, there is evidence that iron influences oxygen precipitation. However, there is a contradiction on whether iron enhances or retards precipitation. The studies of Hackl et al. [298] showed that iron prevents the nucleation of oxygen precipitates even if the iron concentration is as low as 10^{11} cm^{-3}, whereas Zhang et al. [299], Shen et al. [300] and Jablonski et al. [301] found that the precipitation of oxygen is significantly enhanced in the presence of iron, which could be a result of stress relaxation around the oxide by the formation of $FeSi_2$. Miyazaki et al. [4] showed that grown-in iron enhances the formation of oxygen-induced stacking faults (OSF) and, following the conclusions of Hourai et al. [302] and Sadamitsu et al. [303], who observed similar effects on wafers contaminated with iron from the surface, suggested that iron precipitates serve as nucleation sites for OSF.

You et al. [304] reported an electron trap level at $E_C - 0.36$ eV due to the iron–vacancy–oxygen complex (FeOV) in irradiated samples contaminated with iron. The identification of this level was based on the fact that the anneals of the samples at 80 °C resulted in an increase in the concentration of the level at $E_C - 0.36$ eV, accompanied by an equal decrease in the concentration of the *A*-center at $E_C - 0.17$ eV. The latter level is known to be associated with V–O complex [305–307]. The total concentration of the *A* center and the center at $E_C - 0.36$ eV remained constant within 10% during the whole anneal, thus indicating that the first center is converted into the second one [304]. No reduction in the *A*-center concentration was detected during similar anneals in samples containing no interstitial iron, thus confirming that iron is a part of the $E_C - 0.36$ eV center. A decrease in the concentration of the *A*-center during iron precipitation was also observed in the EPR studies of Kustov et al. [308]. Ammerlaan [57], with a reference to a private communication with J.W. Corbett, reported *g*-values of the EPR signal of FeOV center (see Appendix A).

Mchedlidze and Matsumoto [309] studied the electrically detected magnetic resonance (EDMR) of iron in Czochralski-grown (CZ) silicon. They found a new signal with an amplitude correlating with the iron contamination level in the samples. Since the signal was only observed in iron-contaminated oxygen-rich CZ-Si, and was not detected in low-oxygen-content float zone (FZ) Si, it was proposed that the signal originates from complexes containing both iron and oxygen, for example, iron-decorated oxygen precipitates. This signal could not be detected in the EPR measurement mode, probably due to the lower sensitivity of EPR as compared to EDMR. They also reported that the trigonal EDMR signal (see Appendix A), detected after the contamination of CZ samples with iron, changed to that of the orthorhombic symmetry (see Appendix A) after annealing the samples at 450 °C for 60 h.

Wünstel and Wagner [79] reported a defect level at $E_V + 0.33$ eV, which appeared only after a slow cool (air cool or furnace cool) of the samples after the iron diffusion. They assigned this level to an iron–oxygen complex because it appeared in higher concentrations in CZ-grown silicon with a higher oxygen concentration than in FZ-grown silicon.

These few experimental results comprise the current information on the interaction of Fe_i with oxygen, and is by no means complete or self-consistent. The understanding of the interaction of iron with carbon in silicon is even poorer. The only article we are aware of that establishes a correlation between iron and carbon in silicon is the paper of

Kustov et al. [308], who studied the complexing of iron in electron-irradiated silicon with different carbon concentrations. They found that the concentration of interstitial iron decreases after irradiation and reaches a constant value of about 1/3 of the starting concentration for a low carbon density $N_C = 5 \times 10^{16}\,cm^{-3}$, and 2/3 of the starting iron concentration for high carbon density $N_C = 4 \times 10^{17}\,cm^{-3}$. However, they did not infer complexing of iron with carbon from these experiments. The experimental findings were explained by the formation of Fe–I and Fe–V complexes in concentrations depending on the reaction rate of the vacancies (V) and the silicon self-interstitials (I) with carbon [308].

4.5 Interaction of iron and its complexes with hydrogen

The ability of hydrogen to passivate electrically active defects is well known (see, for example, a review of Pearton et al. [310]). Hydrogen passivation of grown-in defects is commonly used in solar cell technology to increase the minority carrier diffusion length (see, for example, [311,312]). Passivation is usually implemented by a relatively low-temperature hydrogen plasma treatment. Substantial concentrations of hydrogen are also introduced into the near-surface region of silicon during routine chemical etching (see, for example, [313–316]). Recent experimental data showed that interaction of hydrogen with impurities is more complicated than just passivation. Complexes of transition metals with hydrogen often introduce new levels in the band gap (see, for example, recently published data on Pt–H complexes [315], Ag–H complexes [317], and Co–H complexes [318]).

Despite the importance of the problem of interaction of iron with hydrogen and passivation of iron-related defects, the data in the literature are inconclusive. Tavendale and Pearton [137,319] studied the influence of hydrogen plasma treatment on Fe-related deep levels and reported that the levels $E_V + 0.32\,eV$ and $E_V + 0.39\,eV$ (note that the latter level is not the level of Fe_i, since interstitial iron had in [137,319] a DLTS peak at higher temperatures with the energy $E_V + 0.40\,eV$), which appeared in DLTS spectra after diffusion of Fe and were thus suggested to be complexes of Fe with an unknown structure. These levels were neutralized by hydrogen to the depth of the hydrogen penetration. They also found that the level of interstitial iron was not affected by the plasma treatment. The latter result has recently been confirmed by Weber [320]. Data of Kouketsu et al. [321,322] indicate that the FeB peak at $E_V + 0.1\,eV$ is effectively neutralized by hydrogen. Yakimov et al. [323] suggested that the introduction of hydrogen during the wet chemical etching stimulates the dissociation of FeB pairs in the near-surface layer and increases the local concentration of unpaired interstitial iron. However, the mechanism of such a dissociation process remains unclear. Kaniewska et al. [324] reported a change in the shape of the DLTS spectra of n-type Fe-contaminated silicon samples with dislocations and stacking faults after hydrogenation. However, the complex nature of the spectra made it impossible to identify the passivated centers.

Several authors suggested that the levels at $E_V + 0.23\,eV$, $E_V + 0.38\,eV$ [321,322], and $E_V + 0.31\,eV$ [325] appear in the band gap after hydrogenation of iron-contaminated samples and argued that they are levels of iron–hydrogen complexes. It was shown that these levels are unstable at elevated temperatures and dissociate after anneals at 175 °C for 30 min [325]. Unfortunately, the experiments described in [321,322,325] lacked a systematic analysis of the interaction of hydrogen with the impurity levels, such as that recently developed in [313,317]. This approach includes the comparison of DLTS spectra of cleaved (no hydrogen) and etched (hydrogen in the near-surface region) samples, and a comparison of the depth profiles of the traps with the predicted distribution of hydrogen. This enables one to even determine the number of hydrogen atoms in a complex. To the best of our knowledge, applications of this method to iron have not yet been reported in the literature.

5 Complexes that include several iron atoms

In the text above we discussed complexes of one iron atom with other impurities. In this section we will give a review of another class of iron-related defects, which consist of several (two to four) iron atoms. These defects were found by EPR and can be considered as the first stage of iron precipitation.

The first report on such defects was published by Muller et al. [29], who studied complexes of iron in electron-irradiated silicon. Since irradiation of iron-doped silicon created a number of new iron-related EPR resonances, it was concluded that these defects contain iron and irradiation-induced defects, most probably, vacancies. We want to emphasize that whereas the number of iron atoms was established from the hyperfine splitting, the number of vacancies in these complexes is somewhat speculative [29]. Spectrum NL20 (see Appendix A) consisted of two iron atoms and was tentatively identified as $(Fe_iFe_iV)^-$ complex. Spectrum NL21 was only observed in n-type silicon and was assigned to a $(Fe_iFe_iV_2)$ complex [29]. Spectrum NL25 also contained two iron atoms and was tentatively identified as another charge state of the defect NL20, namely $(Fe_iFe_iV)^+$. However, one year later Ammerlaan [57] changed the designation of the NL25 spectrum to belong to the Fe_iFe_i complex.

The EPR spectrum of Fe_iFe_i pairs (NL24) was identified by Muller et al. [29] and further studied by van Kooten et al. [326] and Gehlhoff et al. [223]. It was found [326] that this complex can be observed in quenched non-irradiated samples, thus indicating that the complex does not contain irradiation-induced defects (vacancies or self-interstitials). The maximum amplitude of the EPR resonances was after the quench and disappeared after a storage at room temperature for 12 h, or after an anneal at 75 °C for 1 h [326]. The disappearance of this center at or just above room temperature indicates that there is a strong preference for the further aggregation of iron at this center. Since the EPR spectrum could only be fitted using a spin-Hamiltonian with a half-integer spin, the possibility of two neutral Fe_i^0 atoms was ruled out. Since the spectrum was observed in high resistivity n- and p-type silicon and in low-resistivity p-Si, it was suggested that the resonance corresponds to the positively charged complex $(Fe_iFe_i)^+$. This fits well with the assumption that the real spin of the system is $S = 5/2$ [326]. Unfortunately, the authors of [326] did not succeed in finding a unique least-squares fit to their experimental data for $S = 5/2$ and had to restrict their analysis to an effective spin $S = 1/2$.

Gehlhoff et al. [223,224] found a resonance of a defect with a monoclinic symmetry, that was identified as another configuration of the Fe_iFe_i center. Although the authors

of [223] used an effective spin $S = 1/2$ to determine the g-tensor, they reported that $S = 5/2$ corresponded to the more realistic value of $g \approx 2.05$; yet they did not report a complete analysis with this spin. The Fe_iFe_i center was found to be unstable at room temperature. According to the data of [223], the disappearance of the EPR resonance of the Fe_iFe_i pairs could be enhanced by the illumination of the sample with above-band-gap light.

The next intermediate state of the agglomeration of iron, which was observed by EPR, is the $(Fe_i)_4$ cluster. Muller et al. [29] reported that the trigonal EPR spectrum NL22 (see Appendix A), observed in both irradiated and non-irradiated samples, could be modeled only with an unusually high effective spin $S = 4$. To explain this spin, they suggested a model of four ferromagnetically coupled spins $S = 1$ of neutral interstitial iron atoms Fe_i^0. The complex is thus neutral. Studies of the dependence of the concentration of this center on the temperature of isochronal anneals revealed that the concentration of the complex reaches its maximum at temperatures around 140 °C. If the sample is annealed at a higher temperature (above 150 °C), the intensity of NL22 decreases. This can be explained as a growth of $(Fe_i)_4$ clusters to larger agglomerates of iron. Finally, the remaining NL22 centers dissociate at $T > 250$ °C [29]. Note that iron is not the first metal in silicon that was found to form clusters of four atoms. As early as in 1959, Ludwig and Woodbury [327] reported a cluster of four manganese atoms in silicon and observed a hyperfine interaction of the Mn atoms in the cluster. Unfortunately, such an interaction could not be observed in [29] due to the approximately ten times smaller nuclear g-factor of iron compared to manganese.

Ezhevskii et al. [57,328,329], Gehlhoff et al. [223,224], and Irmscher et al. [215] reported complexes with monoclinic and orthorhombic symmetries consisting of two iron atoms and a shallow acceptor such as boron or aluminum (see Appendix A). The centers exhibited quadropole splitting due to the ^{11}B isotope, confirming the involvement of one boron atom. When the iron impurity was enriched with the ^{57}Fe isotope, an additional splitting was observed. The low symmetry of the complexes and the high value of the real spin $S = 5/2$ (note that the complete analysis of the symmetry of these spectra was made for the effective spin $S = 1/2$, see Appendix A) suggested that the complexes consist of two iron atoms [328]. The reaction producing the complexes of FeFeB took place during storage at room temperature, and the intensities of the spectra were found to be a function of the storage time [328].

In Al-doped silicon, Ezhevskii et al. [329] found two EPR spectra with monoclinic-I symmetry (NL40 and NL41, see Appendix A). A resolved hyperfine structure due to ^{27}Al was observed for some EPR orientations. Although the identification of the centers by using the ^{57}Fe isotope has not been done, the low symmetry of the center and the high value of the spin $S = 5/2$ enabled Ezhevskii et al. [329] to identify the centers as $(Fe_i^+Fe_i^0Al^-)$ in two different configurations. The hyperfine splitting due to two ^{57}Fe iron atoms was later reported by Irmscher et al. [215], who also showed that the FeFeAl defect produces two groups of EPR lines corresponding to the ground and the excited states of the same defect. They reported that storage of the samples at room temperature led to the disappearance of the EPR signal, which could be restored by shining above-band-gap light on the samples.

Thus, the EPR studies revealed at least 8 complexes (see Appendix A) consisting of two or four iron atoms. To the best of our knowledge, there are no experimental data on electrical and recombination properties of these centers.

6 Summarizing discussion

Research on properties of iron in silicon has almost as long a history as the studies of silicon itself. Iron was a common unintentional contaminant in the first investigations conducted in the 1960s/1970s. Many experimentalists reported the electrical levels of "quenched-in defects" that were actually the electrical levels of iron and its complexes. In the beginning of the 1980s it was understood that there are three major sources of unintentional iron contamination: iron contamination during silicon growth (see, for example, [160,330]), surface contamination of wafers during chemical cleaning and handling (see, for example, [331]), and introduction of iron from the quartz tubes and ambient during high-temperature anneals (see, for example, [154,156, 332,333]). Unintentional iron contamination levels after heat treatment were reported to be as high as 5×10^{15} cm^{-3} [73, 96,157,160,334]. Later research showed that these contamination levels can be easily avoided by using clean room facilities, high purity chemicals, and state-of-the-art silicon wafers.

A number of studies of iron intentionally introduced in silicon were done between 1980 and approximately 1990. However, the cleanliness of the sample preparation and the quality of the as-grown material was not yet sufficient to exclude the possibility of cross-contamination with other impurities (possibly grown-in to the wafers) which can form complexes with iron. In the beginning of 1990s it has become possible to keep the level of undesired impurities at the level of 10^{11} cm^{-3} and below, which makes it possible to refine the data on iron in silicon accumulated during the past 30 years, and to perform new experiments that were not feasible in the past.

Investigations of iron-related defects provide a perfect example of how different experimental techniques, sensitive to structural, recombination, electrical and optical properties of defects, can be combined to identify the nature of each defect. These techniques include studying samples with different types and levels of doping (variation of the Fermi level position and charge state of the defect), establishing correlations between the amplitude of the signals and the annealing behavior, correlating ionization energies, illuminating the samples (kinetics of dissociation of pairs or switch to another metastable state), comparing experimental results with theoretical calculations, and doping silicon with isotopes of iron and other impurities under investigation.

Research over the years showed that the quenching rate of the samples is enormously important and often determines the type of complexes which are formed in the sample [79,335, 336]. For example, Wünstel and Wagner [79] showed that after a quench of a p-Si sample in silicon oil, only two iron-related peaks were observed ($E_V + 0.1$ eV and $E_V + 0.43$ eV). A slower cool (air cool) resulted in the appearance of three new peaks at $E_V + 0.33$ eV, $E_V + 0.4$ eV, and at $E_V + 0.52$ eV. Finally, after a furnace cool, only a peak corresponding to $E_V + 0.33$ eV was detected. Many iron-related defects require special activation or treatment of the sample before they can

be detected. For instance, some of the defects appear only in irradiated silicon or require illumination to become activated, some increase in density during anneals at slightly elevated temperatures, whereas the others are unstable and dissociate (or grow into larger agglomerates) within hours after diffusion of iron and quench to room temperature.

This review was intended as a summary of the past fundamental research of iron in silicon and as a starting point for future investigations. We showed that significant progress has been made since the 1983 review of one of the authors [19]. Appendices A and B provide a comprehensive list of EPR resonances and deep levels associated with iron and its complexes. However, many problems are still unresolved. The current knowledge of iron in silicon can be summarized as follows. The electrical properties of interstitial iron are well understood. The donor level of iron at $E_V + 0.38$ eV as measured by Hall effect and DLTS is well established, and capture cross-sections for holes and electrons are available (see Appendix B). However, the temperature behavior of the iron level in the band gap requires further investigations, particularly at temperatures below 800 °C. Since the energy position of iron at elevated temperatures determines its solubility and effective diffusivity in p^+ substrates, and thus the segregation coefficient in p/p^+ gettering, the temperature dependence of the position of the iron level in the band gap is not only of fundamental interest, but is also highly relevant for industrial processes.

The photoluminescence signal at a photon energy of 735 meV ($\approx 1.7\,\mu$m) [337–339] and initially identified as that of interstitial iron needs verification. Singh et al. [337] and Weber et al. [118] estimated the energy position of the ground state of the defect responsible for the 735 meV luminescence band at $E_V + (0.39$ to $0.44)$ eV, which coincides with the position of the energy level of the interstitial iron. However, Schlesinger et al. [340] pointed out that there is no detectable isotope shift in the previously identified "phonon replicas", which they expected for interstitial iron.

The solubility of iron in intrinsic silicon is well established. However, the data on iron solubility in moderately and heavily doped n-type silicon are limited to a few doping levels and temperatures, and need further investigations. The experimental data on iron solubility in p-Si and p^+-Si are also limited. The existing theory of solubility enhancement due to the Fermi level effects and pairing with shallow acceptors can in principle be used to calculate the solubility for any given temperature or doping, provided the temperature dependence of the iron level in the band gap is well established.

The data on the diffusion coefficient of iron are numerous and, with a few exceptions, agree with each other. However, the existing expression for the diffusivity of iron does not distinguish the diffusivity of iron in ionized or neutral charge states, and represents the "apparent", or "effective" diffusion coefficient. There are experimental indications and theoretical predictions that the diffusion coefficient of iron does depend on the charge state. However, the data where the charge state is explicitly specified are obtained in narrow temperature intervals, are strongly scattered, and often contradict each other, as discussed in Sect. 1.3.2. Thus, no conclusion on diffusivity of iron in ionized and neutral charge state can be done at the present state of knowledge. Furthermore, the dependence of the iron diffusivity on the doping level of the substrates has never been systematically studied.

Substitutional iron has never been detected by EPR or electrical measurement techniques such as Hall effect or DLTS. There are numerous hypothetical assignments of particular electrical levels to Fe_S, but none of them is convincingly supported by experimental data. It is well known from theoretical considerations [36] that the equilibrium concentration of Fe_S should increase with increasing n-type doping, if Fe_S forms acceptor levels (S) in the band gap. It was suggested that the experimentally observed enhancement of iron solubility in n^+-Si is due to the substitutional fraction of iron [35]. However, there are not enough studies of n^+ silicon to make any definite conclusions. The only experimental technique that claims to detect Fe_S is Mössbauer spectroscopy (see Sect. 1.1), which uses ion implantation that may be subsequently responsible for an enhanced substitutional fraction of iron.

Pairing of iron with shallow acceptors, particularly with boron, was addressed in many publications and substantial progress has been made in both experimental and theoretical areas of the studies. The process of formation and dissociation of pairs is well understood qualitatively. However, a quantitative description of the pairing kinetics is hindered by significant disagreement between various studies in the activation energies for the rate of pairing and dissociation (see Sect. 2). The donor energy levels of the pairs in the lower half of the band gap are well established, with the exception of the level of the orthorhombic configuration of the FeB pair which still needs to be confirmed. The acceptor levels of the iron–acceptor pairs in the upper half of the band gap are only tentatively assigned.

An important issue that has already been addressed by several theoreticians is the type of bonding in the pairs. Although there is no doubt that the electrostatic interaction determines the pairing kinetics, there are indications that covalent or mixed type of bonds are established once a pair is formed. However, the exact role of the covalency is uncertain since conclusions of different groups contradict each other. The scope of the models ranges from purely ionic bonding, covalent bonding via the surrounding silicon atoms, to direct covalent bonding between the iron and the acceptor. Apparently, more detailed theoretical studies using better models and larger clusters are required. The requirement of larger clusters follows from the ENDOR studies which indicated that the iron interacts with up to 100 of the surrounding silicon atoms [24,53,58].

There was an intensive discussion in the literature about the identification of the photoluminescence signal at 1067 meV ($\approx 1.16\,\mu$m) as originating from iron and boron [341]. Since this spectrum was found exclusively in boron-doped silicon, which was intentionally or unintentionally doped with iron, it was initially interpreted as the signal of FeB pairs. However, a number of experimental results obtained later contradict this simple interpretation. First, there is no definite correlation of the intensity of the PL signal with the concentration of iron or boron [341]. Further, Zeeman splitting was nearly isotropic and exhibited no indication of an axial nature, characteristic for FeB pairs [341]. Schlesinger and McGill [342] reported that there was no isotopic shift in the no-phonon line or in the phonon replicas after diffusion of the isotopes ^{54}Fe and ^{56}Fe. A shift would be expected if the phonon mode was a local vibration mode of iron as was suggested by Sauer and We-

ber [244]. In accordance, Kluge et al. [343] reported that anneals of the quenched boron-doped samples at 60 °C and at 90 °C resulted in an increase in the intensity of the FeB-related EPR signal, whereas the intensity of the PL signal at 1.16 μm decreased by more than an order of magnitude. They suggested that the 1.16 μm PL signal is not due to FeB pairs, but rather due to complexes which include several iron or boron atoms. This discussion was recently resolved by Henry et al. [344], who convincingly showed that this PL line is in fact related to gold. Thus, it is possible that this line is not related to iron at all and the whole entirety of the FeB-related photoluminescence studies is just a lesson in the importance of controlling unintentional contamination.

The same ambiguities apply to the identification of the PL signal at around 1.118 eV, tentatively associated with iron and indium [240–242,247,345–348]. Weber et al. [244,347] concluded from Zeeman measurements that the PL center in In-doped silicon consists of at least two different atoms and has ⟨100⟩ symmetry, consistent with the symmetry of FeIn pair. Schlesinger et al. [248] reported that the PL signal in Si:In increases with increasing Fe concentration. In contrast, Watkins et al. [243] failed to find any correlation of the PL intensity with the iron concentration.

The viability of the pairing of iron with phosphorus, and with shallow donors in general, remains a puzzle. There are data that, on one hand, suggest that such pairs do form and are stable, and on the other hand, indications that there is no pairing whatsoever. This problem will be probably addressed more carefully in the near future since the pairing of transition metals with shallow donors is an important mechanism in the explanation and modeling of phosphorus diffusion gettering of iron [349–353], one of the most efficient and least understood gettering techniques.

The high reactivity of iron results in the formation of complexes with other impurities as well. However, only complexes of iron with gold have been sufficiently studied experimentally, while the feasibility of pairing of iron with platinum has been studied only theoretically. Considering the importance of iron and oxygen in silicon, it is surprizing how little research has been done on the interaction between iron and oxygen. It seems that both the complexing of iron with interstitial oxygen and the influence of iron on the nucleation and growth of oxygen precipitates are feasible. However, there exist only preliminary experiments and hypotheses rather than a clear understanding of these processes. The interaction of iron with carbon, the second major impurity in CZ silicon, has never been systematically studied at all (we are aware of only one paper, discussed in Sect. 4.4).

Hydrogen passivation of grown-in defects is used in the industry to improve the quality of solar-grade silicon and is of significant importance for fundamental research. Complexing of metals with hydrogen may result in either the disappearance of existing levels, or in the formation of new defect levels associated with the metal–hydrogen complexes. The length of the list of iron-related defect levels in Appendix B suggests that a complete study of the interaction of hydrogen with each of the iron-related complexes will be a complicated and a time-consuming task. Currently, only few experiments have been reported. There are indications that hydrogen does not passivate interstitial iron, but passivates complexes of iron (see Sect. 4.5).

EPR studies discussed in Sect. 5 demonstrated that iron forms complexes consisting of several iron atoms, such as Fe_iFe_iV, Fe_iFe_iB, Fe_iFe_iAl, Fe_iFe_i, and $(Fe_i)_4$. One can expect that at least a substantial part of iron agglomerates listed in Appendix A form deep levels in the silicon band gap. Studies of the electrical activity of these levels have not yet been done. Some of these complexes, as well as pairs of iron with other impurities may have already been detected in electrical measurements, although are not yet identified. They are primarily deep levels in the upper half and in the middle of the band gap. A number of researches reported a level in iron-contaminated samples at the middle of the bandgap, around $E_V + (0.55 \pm 0.05)$ eV, or $E_C - (0.55 \pm 0.05)$ eV. This level was originally reported by Collins and Carlson [26] and then discussed in [52,79,82,87,88,124,335,354–361]. The concentration of the level was about 1% of the iron concentration determined by the diffusion temperature [87,355]. Since the energy position of the mid-gap iron-related level reported in different references scatter by up to 0.1 eV, it is difficult to say whether the same level was observed in all reports. It is interesting to note that Wünstel and Wagner [79] detected this peak only after a relatively slow air cool of the sample, but failed to detect it after both fast cool (oil quench) or very slow cool (cool in the furnace). Furthermore, they observed the level at $E_V + 0.52$ eV only in boron-doped silicon and not in gallium-doped silicon. This led them to conclude that boron was involved in the formation of the $E_V + 0.52$ eV level. Thus a possible candidate for this center is one of the FeFeB complexes, detected by EPR (see Appendix A). Muller et al. [29] speculated that the mid-gap level may be due to clusters of several iron atoms, i.e., $(Fe_i)_2$ or $(Fe_i)_4$. Several other unidentified levels that are reportedly associated with iron are located in the upper half of the band gap (see [95,161,362–367]).

Thus, while very much is already known about iron in silicon, it will definitely remain an exciting topic for fundamental and applied physical studies for the years to come.

Acknowledgements. The authors are grateful to H. Feick, S. Koveshnikov, W. Seifert, and N. Yaryuin for critical reading of the manuscript. The content of this review was influenced by valuable discussions with A. Buczkowski, S. Estreicher, R. Falster, W. Gehlhoff, D. Gilles, T. Heiser, H. Huff, L. Jastrzebski, L.C. Kimerling, F.G. Kirscht, S. Koveshnikov, S.A. McHugo, A.R. Peaker, K.V. Ravi, G. Rozgonyi, W. Schröter, M. Seibt, M.B. Shabani, B.L. Sopori, T.Y. Tan, O.F. Vyvenko, and J.Weber. The authors gratefully acknowledge the financial support from Mitsubishi Silicon America through the UC MICRO program, the Silicon Wafer Engineering and Defect Science consortium (SiWEDS) that is supported by the National Science Foundation and seven silicon wafer suppliers, and the National Renewable Energy Laboratory (NREL) under subcontract number XAF-8-17607-04.

Appendix A

A Table of EPR parameters of iron-related defects in silicon. The orientation of the principal axes of the g-tensor is as follows: g_1 is parallel to the ⟨100⟩ axis, g_2 and g_3 are parallel to ⟨011⟩ and ⟨0$\bar{1}$1⟩ axes, respectively. An additional angle, θ, determining the angle of rotation of the coordinate system around ⟨0$\bar{1}$1⟩ axis is given for the complexes with monoclinic symmetry.

Defect	Symmetry	Spin S	Principal g values g_1 ($g_\parallel$)	g_2 ($g_\perp$)	g_3 ($g_\perp$)	Reference
Fe_i^0	cubic	1	2.0702	2.0702	2.0702	[52]
(a)			2.0699	2.0699	2.0699	[28,51,56]
Fe_i^+	cubic	3/2	3.524	3.524	3.524	[28,56]
(b)						
$(Fe_iV)^+$	trigonal	3/2	2.1163	2.0935	2.0935	[29]
(NL19)						
(d)						
$(Fe_iB_S)^0$	trigonal	1/2	2.0676	4.0904	4.0904	[168,239]
(c)	($D = 2.7\,cm^{-1}$)	3/2	2.0676	2.0452	2.0452	[164,168]
		3/2	2.068	2.0	2.0	[28]
$(Fe_iB_S)^-$	trigonal	1	2.1345	2.1345	2.1345	[167]
(c,e)	($D = 1.38\,cm^{-1}$)	1	2.080	2.070	2.070	[168,216]
		1/2	4.090	2.068	2.068	[166]
$(Fe_iAl_S)^+$	trigonal	1	4.205	2.3	2.3	[168,215,216]
(c)	($D = -23\,cm^{-1}$)	1/2	8.395	1.076	1.076	[217,218]
$(Fe_iAl_S)^0$	trigonal	1/2	6.389	1.138	1.138	[213]
(NL27)		1/2	6.366	1.144	1.144	[168,215]
(c, e)		1/2	6.389	1.138	1.138	[239]
		1/2	6.370	1.142	1.142	[166]
$(Fe_iAl_S)^-$	trigonal	1	2.075	2.075	2.075	[168,215]
(c,e)	($D = 1.46\,cm^{-1}$)					
$(Fe_iAl_S)^0$	orthorhombic-I:					
(c)	ground state (NL28)	1/2	5.885	1.236	1.612	[213,214,239]
	excited state	1/2	5.877	1.242	1.614	[166]
	description of both lines ($D = -6.5\,cm^{-1}$, $E/D = -0.2540$)	1/2	1.73	2.51	5.36	[214,239]
		3/2	2.080	2.059	2.043	[214,215]
$(Fe_iGa_S)^0$	trigonal	1/2	5.087	2.530	2.530	[28,239]
(c)		1/2	5.089	2.530	2.530	[56,214]
$(Fe_iGa_S)^0$	orthorhombic-I:					
(c)	ground state	1/2	6.19	0.59	0.69	[214,239]
	excited state	1/2	2.02	4.65	3.37	[214,239]
	description of both lines: ($E/D = -0.09$, $D \approx -6\,cm^{-1}$)	3/2	2.07	1.97	2.05	[214]
$(Fe_iIn_S)^0$	trigonal	1/2	6.38	1.08	1.08	[227–230]
(c, f)						
(Lu2)						
$(Fe_iIn_S)^0$	orthorhombic I:					
(c)	ground state:	1/2	6.26	0.36	0.35	[226,230]
	excited state:	1/2	2.070	3.78	4.40	[28,239]
		1/2	2.070	3.80	4.42	[214,226,230]
	description of both lines ($D = -4.9\,cm^{-1}$, $E/D = 0.052$)	3/2	2.09	2.07	2.05	[227]
$(Fe_iIn_S)^+$	orthorhombic	1/2	< 0.3	14.1	< 0.3	[227,232]
(c)						
tentatively						
Fe_iAu_S	trigonal	1/2	2.0993	2.1165	2.1165	[278]
		1/2	2.1001	2.1178	2.1178	[272]
Fe_iS_S (I)	tentatively	1/2	2.010	2.126	2.046	[296]
(tentatively	monoclinic-I					
$(FeS)^-$)	$\theta = 15°$					
Fe_iS_S (II)	tentatively	1/2	1.938	2.015	2.962	[296]
(tentatively	monoclinic-I					
$(FeS)^0$)	$\theta = 28.5°$					
(a)						
Fe_iS_S (III)	tentatively	1/2	1.991	2.042	2.503	[296]
(tentatively	monoclinic-I					
$(FeS)^+$)	$\theta = 46°$					
(b)						

Defect	Symmetry	Spin S	Principal g values g_1 ($g_\parallel$)	g_2 ($g_\perp$)	g_3 ($g_\perp$)	Reference
Fe_iS_S(IV), possibly Fe_i(S–S) (c)	tentatively orthorhombic	1/2	1.939	1.956	2.691	[297]
FePd	trigonal	1/2	2.0407	2.0887	2.0887	[57,289]
FePt	trigonal	1/2	2.0124	2.1264	2.1264	[57,289]
Fe–oxygen (g)	trigonal	1/2	1.9962	1.9956	1.9956	[309]
Fe–oxygen (g)	orthorhombic-I	?	1.9928	1.9962	1.9926	[309]
FeOV	monoclinic-I θ is not reported	1/2	4.20	2.15	4.10	[57]
$(Fe_iFe_iV)^-$ (d) (NL20)	trigonal	1/2 3/2	2.059 2.059	6.235 2.078	6.235 2.078	[29] [29]
$(Fe_iFe_iV)^+$ (d) (NL25)	orthorhombic II	5/2	2.51	1.47	0.57	[29]
$Fe_iFe_iV_2$ (a, d) (NL21)	monoclinic-I $\theta = 33.8°$	1/2 5/2	7.38 2.100	1.961 2.030	4.90 2.006	[29] [29]
$(Fe_iFe_i)^+$ (h) (NL24)	monoclinic-I ground state: excited state: $\theta = 36.4°$ description of both lines: ($E/D \approx 0.20$)	1/2 1/2 5/2	1.15 3.90 ≈ 2.05	9.44 3.50 ≈ 2.05	2.06 5.07 ≈ 2.05	[29,223,224,326] [223,224] [223]
$(Fe_i)_4$ (NL22)	trigonal	4	2.075	2.068	2.068	[29]
FeFeB (c) (NL33)	monoclinic-I ground state (?) excited state (?) $\theta = 36.7°$ both lines: ($E/D \approx 0.15$)	1/2 1/2 1/2 5/2	1.49 1.472 2.96 ≈ 2.07	2.91 2.895 3.05 ≈ 2.07	8.97 8.899 5.46 ≈ 2.07	[223,224] [328] [223,224] [223,224]
FeFeB (c) (NL32)	orthorhombic-I: ground state (?) excited state (?) description of both lines: ($E/D \approx 0.08$)	1/2 1/2 5/2	7.55 7.902 1.73 ≈ 2.05	4.18 4.184 1.94 ≈ 2.05	1.81 1.811 5.80 ≈ 2.05	[223,224] [328] [223,224] [223,224]
FeFeAl (c) (NL40)	monoclinic-I ground state (?) excited state (?) $\theta = 36.6°$ description of both lines: ($E/D \approx 0.1447$, $D = 3\,cm^{-1}$)	1/2 1/2 1/2 1/2 5/2 5/2	1.470 1.48 1.404 5.48 2.064 2.081	2.836 2.82 2.661 3.17 2.064 2.023	8.907 8.89 9.027 2.86 2.064 2.083	[329] [215] [329] [215] [329] [215]

(a) observed predominantly in n-Si.
(b) observed predominantly in p-Si.
(c) appears after one to thirty days of storage at room temperature, necessary for association of the pairs.
(d) observed in irradiated silicon.
(e) requires activation by above-band-gap light
(f) activated by illumination with light with $h\nu > 0.5$ eV.
(g) was detected in CZ-grown silicon by EDMR.
(h) unstable at slightly elevated temperatures ($T > 60\,°C$).

Appendix B

Table of electrical levels associated with iron and its complexes. Energy level positions were determined using deep level transient spectroscopy (DLTS), Hall effect (Hall), photocapacitance technique (PhCap), electron paramagnetic resonance (EPR) and photo-EPR, Fourier transform infrared spectroscopy (FTIR), and thermally stimulated capacitance

(TSCAP). Uncertainty in the energy position reflects only scatter in experimental data reported by different groups, but does not include possible uncertainty of their data (which is usually not reported). Capture cross-sections were determined from temperature dependence of emission rate (Arrhenius plot) with exception of several studies that used direct isothermal methods (see Chapt. 11 of [369] for details of the experimental techniques). These studies are indicated by (*).

Defect	Energy position /eV measurement methods	Hole capture cross-section	Electron capture cross-section
$Fe_i^{0/+}$	$E_V + (0.38 \pm 0.01)$ eV [26,75,78,80–82,88–90] DLTS, Hall, PhCap, EPR	$3.9 \times 10^{-16} \exp(-0.045\ \text{eV}/k_B T)$ cm^2 [66,80,90–93] (*)	$\sigma_n \approx 4 \times 10^{-14}$ cm^2 ($T = 300$ K) [106,107]
$(FeB)^{0/+}$, trigonal	$E_V + 0.1$ eV, [80,91,92,124] DLTS	$\sigma_p \approx 2 \times 10^{-14}$ cm^2 [80] $\sigma_p \approx 1.5 \times 10^{-13}$ cm^2 ($T = 55$ K) [92] $\sigma_p > 4 \times 10^{-15}$ cm^2 [124]	$\sigma_n \approx 4 \times 10^{-13}$ cm^2 [107]
$(FeB)^{-/0}$, trigonal	$E_C - (0.26 \pm 0.03)$ eV [90,91,167,172–174] DLTS, Hall, photoEPR, FTIR	$\sigma_p \approx 3 \times 10^{-14}$ cm^2 ($T = 300$ K) [175,176] $\sigma_p \approx 3 \times 10^{-15}$ cm^2 ($T = 90$ K) [90] (*)	$\sigma_n \approx 2.5 \times 10^{-15}$ cm^2 ($T = 300$ K) [175,176] $\sigma_n \approx 10^{-15}$ cm^2 ($T = 90$ K) [90] (*)
$(FeB)^{0/+}$, orthorhombic (tentatively)	$E_V + 0.07$ eV [86,186] Laplace Transform DLTS	?	?
$(FeB)^{-/0}$, orthorhombic (tentatively)	$E_C - 0.43$ eV [172,188] TSCAP	?	$\sigma_n \approx 3 \times 10^{-15}$ cm^2, [188]
$(FeAl)^{0/+}$, trigonal	$E_V + (0.20 \pm 0.01)$ eV [78,80,81,144,154,170,223] DLTS	$\sigma_p \approx 2 \times 10^{-14}$ cm^2 [220] $\sigma_p \approx 4 \times 10^{-14}$ cm^2 [80]	?
$(FeAl)^{0/+}$, orthorhombic	$E_V + 0.13$ eV [78,80,144,220,223] DLTS	$\sigma_p \approx 6 \times 10^{-14}$ cm^2 [220]	?
$(FeGa)^{0/+}$, trigonal	$E_V + 0.24$ eV [80,170,225] DLTS	$\sigma_p \approx 2 \times 10^{-14}$ cm^2 [80] $\sigma_p \approx 3 \times 10^{-15}$ cm^2 ($T = 120$ K) [170]	?
$(FeGa)^{0/+}$, orthorhombic	$E_V + 0.14$ eV [225] DLTS	?	?
$(FeIn)^{0/+}$, trigonal	$E_V + 0.27$ eV [225] DLTS	?	?
$(FeIn)^{-/0}$, trigonal	$E_C - 0.32$ eV [233] FTIR	?	?
$(FeIn)^{0/+}$, orthorhombic	$E_V + 0.15$ eV [225] DLTS	?	?
$(FeIn)^{-/0}$, orthorhombic	$E_C - 0.39$ eV [233] FTIR	?	?
$(FeAu)^{0/+}$	$E_V + (0.44 \pm 0.01)$ eV [157,280,282] DLTS, Hall	$\sigma_p \approx 2 \times 10^{-13}$ cm^2 [282]	?
$(FeAu)^{-/0}$	$E_C - (0.34 \pm 0.01)$ eV [280,283,284] DLTS	?	$\sigma_n \approx 3 \times 10^{-15}$ cm^2 [284] $\sigma_n \approx 2 \times 10^{-15}$ cm^2 [280] (*)
FePd	$E_C - 0.32$ eV [291,292] DLTS	?	?
FePd (tentatively)	$E_V + 0.52$ eV [292] DLTS	?	?
$(FeZn)^{0/+}$	$E_V + 0.17$ eV [295]	$\sigma_p = 5 \times 10^{-15}$ cm^2 ($T = 90$ K), [295]	?
$(FeZn)^{-/0}$	$E_C - 0.47$ eV [295]	?	$\sigma_n = 1.5 \times 10^{-16}$ cm^2 ($T = 250$ K), [295]
FeOV	$E_C - 0.36$ eV [304] DLTS	?	$\sigma_n \approx 4 \times 10^{-15}$ cm^2 [304]
Fe–O (tentatively)	$E_V + 0.33$ eV [79] DLTS	?	?

References

1. J. Wong-Leung, D.J. Eaglesham, J. Sapjeta, D.C. Jacobson, J.M. Poate, J.S. Williams: J. Appl. Phys. **83**, 580 (1998)
2. K. Honda, A. Ohsawa, T. Nakanishi: J. Electrochem. Soc. **142**, 3486 (1995)
3. E.P. Burte, W. Aderhold: Solid State Electron. **41**, 1021 (1997)
4. M. Miyazaki, S. Miyazaki, T. Kitamura, T. Aoki, Y. Nakashima, M. Hourai, T. Shigematsu: Jpn. J. Appl. Phys. **34**, 409 (1995)
5. W.B. Henley, L. Jastrzebski, N.F. Haddad: J. Non-Cryst. Solids **187**, 134 (1995)
6. W. Rieger: In *Crystalline Defects and Contamination: Their Impact and Control in Device Manufacturing*, ed. by B.O. Kolbesen, C. Claeys, P. Stallhofer, F. Tardif (The Electrochemical Society, Grenoble, France 1993) p.103
7. F. Tardif, J.P. Joly, T. Lardin, A. Tonti, P. Patruno, D. Levy, W. Sievert: In *Crystalline Defects and Contamination: Their Impact and Control in Device Manufacturing*, ed. by B.O. Kolbesen, C. Claeys, P. Stallhofer, F. Tardif (The Electrochemical Society, Grenoble, France 1993) p.114
8. G. Obermeier, D. Huber: J. Appl. Phys. **81**, 7345 (1997)
9. W.C. McColgin, J.P. Lavine, C.V. Stancampiano, J.B. Russel: In Defect & Impurity Engineered Semiconductors & Devices II, ed. by S. Ashok, J. Chevallier, W. Goetz, B. Sopori, K. Sumino (Materials Research Society, San Francisco, CA, USA 1998) p.475
10. B.O. Kolbesen, W. Bergholz, H. Wendt: Mater. Sci. Forum **38-41**, 1 (1989)
11. L. Jastrzebski: IEEE Trans. Electron Dev. ED-**29**, 475 (1982)
12. P.J. Ward: J. Electrochem. Soc. **129**, 2573 (1982)
13. H.J. Schulze, B.O. Kolbesen: In *Power Semiconductor Materials and Devices*, ed. by S.J. Pearton, R.J. Shul, E. Wolfgang, F. Ren, S. Tenconi (Materials Research Society, Warrendale, PA 1998) p.381
14. O.V. Bogorodskii, T.P. Vorontsova, O.S. Zhgutova, V.A. Zlobin, L.A. Kirdyashkina, V. A. Kuz'min, A.S. Kyuregyan, Y.M. Loktaev, L.S. Rybachuk, Y.G. Sorokin, P.N. Shlygin, V.V. Fedorov: Soviet Physics - Technical Physics **30**, 818 (1985)
15. H.H. Busta, H.A. Waggener: J. Electrochem. Soc. **124**, 1424 (1977)
16. R.H. Hopkins, A. Rohatgi: J. Cryst. Growth **75**, 67 (1985)
17. M. Ohring: *Reliability and Failure of Electronic Materials and Devices* (Academic Press, San Diego 1998)
18. M. Penn: Microelectron. J. **23**, 255 (1992)
19. E.R. Weber: Appl. Phys. A **30**, 1 (1983)
20. A.G. Milnes: *Deep Impurities in Semiconductors* (Wiley-Interscience, Chichester, Sussex, UK 1973)
21. J.W. Chen, A.G. Milnes: In *Annual Review of Materials Science*, ed. by R.A. Huggins, R.H. Bube, D.A. Vermilyea (Annual Rev. Inc., Palo Alto, CA, USA 1980) p.157
22. K. Graff: *Metal Impurities in Silicon-Device Fabrication* (Springer, Berlin 1995)
23. H.H. Woodbury, G.W. Ludwig: Phys. Rev. **117**, 102 (1960)
24. S. Greulich-Weber, J.R. Niklas, E.R. Weber, J.M. Spaeth: Phys. Rev. B **30**, 6292 (1984)
25. P. Schwalbach, S. Laubach, M. Hartick, E. Kankeleit: Phys. Rev. Lett. **64**, 1274 (1990)
26. C.B. Collins, R.O. Carlson: Phys. Rev. **108**, 1409 (1957)
27. M. Stojic, V. Spiric, D. Kostoski: Fizika (suppl. 1) **12**, 70 (1980)
28. G.W. Ludwig, H.H. Woodbury: In *Solid State Physics*, ed. by F. Seitz, D. Turnbull (Academic, New York 1962) p.223
29. S.H. Muller, G.M. Tuynman, E.G. Sieverts, C.A.J. Ammerlaan: Phys. Rev. B **25**, 25 (1982)
30. P. He, Z. You: Phys. Status Solidi A **125**, K31 (1991)
31. N.T. Bendik, L.S. Milevskii: Dokl. Akad. Nauk USSR **195**, 107 (1970)
32. H.H. Woodbury, G.W. Ludwig: Phys. Rev. Lett. **5**, 96 (1960)
33. M. Seibt, M. Griess, A.A. Istratov, H. Hedemann, A. Sattler, W. Schroeter: Phys. Status Solidi A **166**, 171 (1998)
34. A.A. Istratov, E.R. Weber: Appl. Phys. A **66**, 123 (1998)
35. D. Gilles, W. Schroter, W. Bergholz: Phys. Rev. B **41**, 5770 (1990)
36. R.N. Hall, J.H. Racette: J. Appl. Phys. **35**, 379 (1964)
37. W. Shockley, J.L. Moll: Phys. Rev. **119**, 1480 (1960)
38. F. Beeler, O.K. Andersen, M. Scheffler: Phys. Rev. Lett. **55**, 1498 (1985)
39. F. Beeler, O.K. Andersen, M. Scheffler: Phys. Rev. B **41**, 1603 (1990)
40. A. Zunger, U. Lindefelt: Phys. Rev. B **26**, 5989 (1982)
41. A. Zunger, U. Lindefelt: Phys. Rev. B **27**, 1191 (1983)
42. G. Weyer, S. Degroote, M. Fanciulli, V.N. Fedoseyev, G. Langouche, V.I. Mishin, A.M. van Bavel, A. Vantomme: Mater. Sci. Forum **258-63**, 437 (1997)
43. G. Langouche: Hyperfine Interact. **72**, 217 (1992)
44. S. Laubach, P. Schwalbach, M. Hartick, E. Kankeleit, G. Klingelhofer, R. Sielemann: Z. Physik B **75**, 173 (1989)
45. G.W. Ludwig, H.H. Woodbury: In Proc. of Int. Conf. on Semiconductor Physics (Prague 1960) p.596
46. G.W. Ludwig, H.H. Woodbury: Phys. Rev. Lett. **5**, 98 (1960)
47. H. Katayama-Yoshida, A. Zunger: Phys. Rev. B **31**, 7877 (1985)
48. F.S. Ham: Phys. Rev. **138**, A1727 (1965)
49. H. Weihrich, H. Overhof: Mater. Sci. Forum **196-201**, 677 (1995)
50. A. Thilderkvist, G. Grossman, M. Kleverman, H.G. Grimmeiss: Phys. Rev. B **58**, 7723 (1998)
51. G.W. Ludwig, H.H. Woodbury, R.O. Carlson: Phys. Rev. Lett. **1**, 295 (1958)
52. G. Feher: Phys. Rev. **114**, 1219 (1959)
53. E.G. Sieverts, S.H. Muller, C.A.J. Ammerlaan, E.R. Weber: Solid State Commun. **47**, 631 (1983)
54. M. Berke, E. Weber, H. Alexander, H. Luft, B. Elschner: Solid State Commun. **20**, 881 (1976)
55. W. Gehlhoff, K.H. Segsa: Phys. Status Solidi B **41**, K21 (1977)
56. G.W. Ludwig, H.H. Woodbury: Phys. Rev. **117**, 1286 (1960)
57. C.A.J. Ammerlaan: Solid State Phenom. **6-7**, 591 (1989)
58. J.J. van Kooten, E.G. Sieverts, C.A.J. Ammerlaan: Phys. Rev. B **37**, 8949 (1988)
59. D.A. van Wezep, T. Gregorkiewicz, E.G. Sieverts, C.A.J. Ammerlaan: Phys. Rev. B **34**, 4511 (1986)
60. J.D. Gerson, L.J. Cheng, J.W. Corbett: J. Appl. Phys. **48**, 4821 (1977)
61. K. Nakashima: Jpn. J. Appl. Phys. **24**, 1018 (1985)
62. Y. Kamiura, M. Yoneta, F. Hashimoto: Phys. Status Solidi A **120**, K11 (1990)
63. N.H. Sheng, J.L. Merz: J. Appl. Phys. **55**, 3083 (1984)
64. J.T. Borenstein, J.T. Jones, J.W. Corbett, G.S. Oehrlein, R.L. Kleinhenz: Appl. Phys. Lett. **49**, 199 (1986)
65. M.L. Swanson: Phys. Status Solidi **33**, 721 (1969)
66. H. Indusekhar, V. Kumar: Phys. Status Solidi A **95**, 269 (1986)
67. N.I. Akulovich, V.V. Petrov, V.D. Tkachev: Sov. Phys. Semicond. **16**, 969 (1982)
68. H. Feichtinger, A. Gschwandtner, J. Waltl: Phys. Status Solidi A **53**, K71 (1979)
69. W. Leskoschek, H. Feichtinger, G. Vidrich: Phys. Status Solidi A **20**, 601 (1973)
70. N.H. Sheng, J.L. Merz: Physica **116B**, 553 (1983)
71. L. Elstner, W. Kamprath: Phys. Status Solidi **22**, 541 (1967)
72. D.E. Ioannou: Phys. Status Solidi A **72**, K33 (1982)
73. M. Stojic: Phys. Status Solidi A **70**, K39 (1982)
74. H.J. Rijks, J. Bloem, L.J. Giling: J. Appl. Phys. **50**, 1370 (1979)
75. H. Feichtinger, J. Waltl, A. Gschwandtner: Solid State Commun. **27**, 867 (1978)
76. K.P. Abdurakhmanov, B.A. Kotov, J. Kreissl, A.A. Lebedev, S.B. Utamuradova: Sov. Phys. Semicond. **19**, 218 (1985)
77. H. Nakashima, T. Isobe, Y. Yamamoto, K. Hashimoto: Jpn. J. Appl. Phys. **27**, 1542 (1988)
78. K. Graff, H. Pieper: J. Electrochem. Soc. **128**, 669 (1981)
79. K. Wunstel, P. Wagner: Solid State Commun. **40**, 797 (1981)
80. K. Wunstel, P. Wagner: Appl. Phys. A **27**, 207 (1982)
81. K. Wunstel, K.H. Froehner, P. Wagner: Physica B & C **116**, 301 (1983)
82. J.W. Chen, A.G. Milnes: In Proc. of National Workshop on low cost polycrystalline silicon solar cells, ed. by T.L. Chu, S.S. Chu (Dallas, Texas 1976) p.292
83. S.A. McHugo, R.J. McDonald, A.R. Smith, D.L. Hurley, E.R. Weber: Appl. Phys. Lett. **73**, 1424 (1998)
84. S.A. McHugo, R.J. McDonald, A.R. Smith, D.L. Hurley, A.A. Istratov, H. Hieslmair, E.R. Weber: In *Defect and Impurity Engineered Semiconductors and Devices II*, ed. by S. Ashok, J. Chevallier, K. Sumino, B.L. Sopori, W. Gotz (Mat. Res. Soc., Warrendale, PA 1998) p.361
85. D.A. Porter, K.E. Easterling: *Phase transformation in metals and alloys* (Van Nostrand Reinhold, Wokingham, UK 1981)
86. L. Dobaczewski, P. Kaminski, R. Kozlowski, M. Surma: Mater. Sci. Forum **196-201**, 669 (1995)
87. K. Nakashima, M. Chijiiwa: Jpn. J. Appl. Phys. **25**, 234 (1986)
88. O.O. Awadelkarim, B. Monemar: J. Appl. Phys. **64**, 6306 (1988)
89. A. Rohatgi, J.R. Davis, R.H. Hopkins, P. Rai-Choudhury, P.G. McMullin: Solid State Electron. **23**, 415 (1980)

90. H. Lemke: Phys. Status Solidi A **64**, 215 (1981)
91. S.D. Brotherton, P. Bradley, A. Gill: J. Appl. Phys. **57**, 1941 (1985)
92. X. Gao, H. Mollenkopf, S. Yee: Appl. Phys. Lett. **59**, 2133 (1991)
93. H. Lemke: Phys. Status Solidi A **63**, 127 (1981)
94. E. Schibli, A.G. Milnes: Mater. Sci. Eng. **2**, 229 (1967/68)
95. V.B. Voronkov, A.A. Lebedev, A.T. Mamadalimov, B.M. Urunbaev, T.A. Usmanov: Sov. Phys. Semicond. **14**, 1217 (1980)
96. H.R. Szawelska, H. Feichtinger: J. Phys. C **14**, 4131 (1981)
97. M.A. Abdugafurova, A.A. Lebedev, A.T. Mamadalimov, S. Makhkamov: Sov. Phys. Semicond. **8**, 1409 (1974)
98. M. Okuyama, N. Matsunaga, J.W. Chen, A.G. Milnes: J. Electron. Mater. **8**, 501 (1979)
99. N.T. Bagraev, I.S. Polovtsev: Phys. Status Solidi B **150**, 19 (1988)
100. N.T. Bagraev, A.A. Lebedev, V.A. Mashkov, I.S. Polovtsev: Sov. Phys. Solid State **30**, 1197 (1988)
101. N.T. Bagraev, I.S. Polovtsev: Sov. Phys. Semicond. **23**, 1016 (1989)
102. N.T. Bagraev, I.S. Polovtsev: Sov. Phys. Semicond. **23**, 686 (1989)
103. A.A. Lebedev, B.M. Urunbaev: Sov. Phys. Semicond. **15**, 350 (1981)
104. J. Olajos, B. Bech Nielsen, M. Kleverman, P. Omling, P. Emanuelsson, H.G. Grimmeiss: Mater. Sci. Forum **38-41**, 397 (1989)
105. J. Olajos, B. Bech Nielsen, M. Kleverman, P. Omling, P. Emanualsson, H.G. Grimmeiss: Appl. Phys. Lett. **53**, 2507 (1988)
106. J. Lagowski, P. Edelman, A.M. Kontkiewicz, O. Milic, W. Henley, M. Dexter, L. Jastrzebski, A.M. Hoff: Appl. Phys. Lett. **63**, 3043 (1993)
107. G. Zoth, W. Bergholz: J. Appl. Phys. **67**, 6764 (1990)
108. A.B. Roitsin, L.A. Firshtein: Sov. Phys. Solid State **13**, 50 (1971)
109. G.G. DeLeo, G.D. Watkins, W.B. Fowler: Phys. Rev. B **23**, 1851 (1981)
110. G.D. Watkins, G.G. Deleo, W.B. Fowler: Physica B **116**, 28 (1983)
111. A. Zunger: In *Solid State Physics*, ed. by H. Ehrenreich, D. Turnbull (Academic Press, Orlando 1986) p. 275
112. G.G. DeLeo, G.D. Watkins, W. Beall Fowler: Phys. Rev. B **25**, 4972 (1982)
113. H. Katayama-Yoshida, A. Zunger: Phys. Rev. B **31**, 8317 (1985)
114. H. Katayama-Yoshida: Int. J. Modern Phys. B **1**, 1207 (1987)
115. H. Katayama-Yoshid, A. Zunger: Phys. Rev. Lett. **53**, 1256 (1984)
116. H. Weihrich, H. Overhof: Phys. Rev. B **54**, 4680 (1996)
117. J. Utzig: J. Appl. Phys. **65**, 3868 (1989)
118. J. Weber, P. Wagner: J. Phys. Soc. Japan (Suppl. A) **49**, 263 (1980)
119. J.A. Van Vechten: In *Handbook on Semiconductors*, ed. by T.S. Moss, S.P. Keller (North-Holland, Amsterdam 1980) p.2
120. C.J. Gallagher: J. Phys. Chem. Solids **3**, 82 (1957)
121. T. Heiser, A. Mesli: Phys. Rev. Lett. **68**, 978 (1992)
122. E.R. Weber: In *Properties of Silicon* (EMIS Datareviews Series No.4), (INSPEC, London 1988) p.421
123. J.D. Struthers: J. Appl. Phys. **27**, 1560 (1956)
124. L.C. Kimerling, J.L. Benton, J.J. RubIn: Inst. Phys. Conf. Ser. **59**, 217 (1981)
125. W.H. Shepherd, J.A. Turner: J. Phys. Chem. Solids **23**, 1697 (1962)
126. D. Gilles: Ph.D. Thesis (University of Goettingen 1987)
127. T. Isobe, H. Nakashima, K. Hashimoto: Jpn. J. Appl. Phys. **28**, 1282 (1989)
128. I.V. Antonova, K.B. Kadyrakunov, E.V. Nidaev, L.S. Smirnov: Phys. Status Solidi A **76**, K213 (1983)
129. V.A. Uskov: Inorganic Mater. **11**, 848 (1975)
130. K. Ryoo, R.K. Graupner: Mater. Sci. Eng. B **4**, 251 (1989)
131. H. Takahashi, M. Suezawa, K. Sumino: Phys. Rev. B **46**, 1882 (1992)
132. W. Wijaranakula: J. Electrochem. Soc. **140**, 275 (1993)
133. Y.H. Lee, R.L. Kleinhenz, J.W. Corbett: Appl. Phys. Lett. **31**, 142 (1977)
134. B.I. Boltaks, M.K. Bakhadyrkhanov, G.S. Kulikov: Sov. Phys. Solid State **13**, 2240 (1972)
135. S.V. Koveshnikov, G.A. Rozgonyi: Appl. Phys. Lett. **66**, 860 (1995)
136. T. Heiser, A. Mesli: Appl. Phys. Lett. **58**, 2240 (1991)
137. A.J. Tavendale, S.J. Pearton: J. Phys. C **16**, 1665 (1983)
138. L.C. Kimerling, J.L. Benton: Physica B & C **116**, 297 (1983)
139. L.C. Kimerling: In *Defects in Semiconductors*, ed. by J. Narayan, T.Y. Tan (North-Holland, Amsterdam 1981) p.85
140. P. Baruch: J. Appl. Phys. **32**, 653 (1961)
141. J.H. Reiss, R.R. King, K.W. Mitchell: Appl. Phys. Lett. **68**, 3302 (1996)
142. A. Kaniava, E. Gaubas, J. Vaitkus, J. Vanhellemont, A.L.P. Rotondaro: Mater. Sci. Technol. **11**, 670 (1995)
143. A. Kaniava, A.L.P. Rotondaro, J. Vanhellemont, U. Menczigar, E. Gaubas: Appl. Phys. Lett. **67**, 3930 (1995)
144. A. Chantre, D. Bois: Phys. Rev. B **31**, 7979 (1985)
145. T. Heiser, A. Mesli: Appl. Phys. Lett. **68**, 1868 (1996)
146. H. Reiss, C.S. Fuller, F.J. Morin: Bell Syst. Technol. J. **35**, 535 (1956)
147. A.A. Istratov, C. Flink, H. Hieslmair, E.R. Weber, T. Heiser: Phys. Rev. Lett. **81**, 1243 (1998)
148. H. Takahashi, M. Suezawa, K. Sumino: Jpn. J. Appl. Phys. **36**, 6807 (1997)
149. H. Takahashi, M. Suezawa, K. Sumino: Mater. Sci. Forum **83-7**, 155 (1992)
150. M. Hansen, K. Anderko: *Constitution of binary alloys* (McGraw-Hill, New York 1958)
151. J.H. Westbrook: *Moffatt's handbook of binary phase diagrams* (Genium Publishing Co., New York 1997)
152. T.B. Massalski, H. Okamoto, P.R. Subramanian, L. Kacprzak: *Binary Alloy Phase Diagrams* (ASM International, Materials Park, Ohio, USA 1990)
153. F.A. Trumbore: Bell Syst. Technol. J. **39**, 205 (1960)
154. H. Feichtinger: Acta Phys. Austr. **51**, 161 (1979)
155. E.R. Weber: In *Properties of Silicon* (EMIS Datareviews Series No.4), (INSPEC, London 1988) p.442
156. E. Weber, H.G. Riotte: J. Appl. Phys. **51**, 1484 (1980)
157. H. Feichtinger: Inst. Phys. Conf. Ser. **46**, 528 (1979)
158. O. Kononchuk, K.G. Korablev, N. Yarykin, G.A. Rozgonyi: Appl. Phys. Lett. **73**, 1206 (1998)
159. A.A. Istratov: (1995), unpublished
160. E. Weber: Appl. Phys. Lett. **33**, 433 (1978)
161. K. Kakishita, K. Kawakami, S. Suzuki, E. Ohta, M. Sakata: J. Appl. Phys. **65**, 3923 (1989)
162. E.G. Colas, E.R. Weber: Appl. Phys. Lett. **48**, 1371 (1986)
163. V.I. Fistul, V.A. Shmugurov: Sov. Phys. Semicond. **23**, 431 (1989)
164. W. Gehlhoff, K.H. Segsa: Phys. Status Solidi B **115**, 443 (1983)
165. W. Gehlhoff, K.H. Segsa, C. Meyer: Phys. Status Solidi B **105**, K91 (1981)
166. J.M. Spaeth, S. Martini, S. Greulich-Weber: Semicond. Sci. Technol. **13**, 725 (1998)
167. W. Gehlhoff, U. Rehse: In *Defect Engineering in Semiconductor Growth, Processing and Device Technology*, ed. by S. Ashok, J. Chevallier, K. Sumino, E. Weber (Materials Research Society, Pittsburgh, PA 1992) p.507
168. W. Gehlhoff, K. Irmscher: Solid State Phenom. **32-33**, 219 (1993)
169. E. Weber: Crystal Res. Technol. **16**, 209 (1981)
170. H. Lemke: Phys. Status Solidi A **76**, 223 (1983)
171. L. Samuelson, P. Omling: In Proc. of 18th Int. Conf. on Phys. Semicond., ed. by O. Engstrom (Stockholm, Sweden 1986) p.931
172. H. Nakashima, T. Sadoh: In *Defect Engineering in Semiconductor Growth, Processing and Device Technology*, ed. by S. Ashok, J. Chevallier, K. Sumino, E. Weber (Materials Research Society, Pittsburgh, PA 1992) p.555
173. S. Ghatnekar-Nilsson, M. Kleverman, P. Emanuelsson, H.G. Grimmeiss: Semicond. Sci. Technol. **8**, 1857 (1993)
174. S. Ghatnekar-Nilsson, M. Kleverman, P. Emanuelsson, H.G. Grimmeiss: Mater. Sci. Forum **143-7**, 171 (1994)
175. D. Walz, J.P. Joly, G. Kamarinos: Appl. Phys. A **62**, 345 (1996)
176. D. Walz, G. Le Carval, J.P. Joly, G. Kamarinos: Semicond. Sci. Technol. **10**, 1022 (1995)
177. W. Shockley, W.T. Read: Phys. Rev. **87**, 835 (1952)
178. R.N. Hall: Phys. Rev. **87**, 387 (1952)
179. Y. Hayamizu, T. Hamaguchi, S. Ushio, T. Abe, F. Shimura: J. Appl. Phys. **69**, 3077 (1991)
180. G. Zoth: In *Recombination Lifetime Measurements in Silicon*, ed. by D.C. Gupta, F.R. Bacher, W.M. Hughes (ASTM, West Conshohocken, PA 1998) p.30
181. R. Falster, G. Borionetti: In *Recombination Lifetime Measurements in Silicon*, ed. by D.C. Gupta, F.R. Bacher, W.M. Hughes (ASTM, West Conshohocken, PA 1998) p.226
182. D.K. Schroder: In *Recombination Lifetime Measurements in Silicon*, ed. by D.C. Gupta, F.R. Bacher, W.M. Hughes (ASTM, West Conshohocken, PA 1998) p.5
183. M.L. Polignano, F. Cazzaniga, A. Sabbadini, G. Queirolo, A. Cacciato, A. Di Bartolo: Mater. Sci. Eng. B **42**, 157 (1996)
184. T. Pavelka: In *Recombination Lifetime Measurements in Silicon*, ed. by D.C. Gupta, F.R. Bacher, W.M. Hughes (ASTM, West Conshohocken, PA 1998) p.206

185. J. Lagowski, P. Edelman, V. Faifer: In *Recombination Lifetime Measurements in Silicon*, ASTM STP 1340, ed. by D.C. Gupta, F.R. Bacher, W.M. Hughes (ASTM, West Conshohocken, PA 1998)
186. L. Dobaczewski, M. Surma: Acta Phys. Pol. A **90**, 613 (1996)
187. H. Nakashima, T. Sadoh, T. Tsurushima: J. Appl. Phys. **73**, 2803 (1993)
188. H. Nakashima, T. Sadoh, T. Tsurushima: Phys. Rev. B **49**, 16983 (1994)
189. H. Nakashima, T. Sadoh, T. Tsurushima: Mater. Sci. Forum **143-7**, 1191 (1994)
190. H. Hieslmair, A.A. Istratov, T. Heiser, E.R. Weber: J. Appl. Phys. **84**, 713 (1998)
191. F.S. Ham: J. Phys. Chem. Solids **6**, 335 (1958)
192. S.S. Ostapenko, R.E. Bell: J. Appl. Phys. **77**, 5458 (1995)
193. R.E. Bell, II, S. Ostapenko, J. Lagowski: In *Defect and Impurity Engineered Semiconductors and Devices*, ed. by S. Ashok, J. Chevallier, I. Akasaki, N.M. Johnson, B.L. Sopori (Materials Research Society, Pittsburgh, PA 1995) p.647
194. L.C. Kimerling: Solid State Electron. **21**, 1391 (1978)
195. J.R. Troxell, A.P. Chatterjee, G.D. Watkins, L.C. Kimerling: Phys. Rev. B **19**, 5336 (1979)
196. T. Takahashi, M. Suezawa: Mater. Sci. Forum **258-63**, 443 (1997)
197. S. Sakauchi, M. Suezawa, K. Sumino, H. Nakashima: J. Appl. Phys. **80**, 6198 (1996)
198. S. Sakauchi, M. Suezawa, K. Sumino: Mater. Sci. Forum **196-201**, 1345 (1995)
199. D.V. Lang, L.C. Kimerling: Phys. Rev. Lett. **33**, 489 (1974)
200. D.V. Lang, L.C. Kimerling, S.Y. Leung: J. Appl. Phys. **47**, 3587 (1976)
201. K. Maeda, M. Sato, A. Kubo, S. Takeuchi: J. Appl. Phys. **54**, 161 (1983)
202. D.V. Lang, L.C. Kimerling: Appl. Phys. Lett. **28**, 248 (1976)
203. R.M. Feenstra, T.C. McGill: Phys. Rev. B **25**, 6329 (1982)
204. J. Shirafuji, T. Kakiuchi, K. Oka, Y. Inuishi: Jpn. J. Appl. Phys. **22**, 1368 (1983)
205. J.D. Weeks, J.C. Tully, L.C. Kimerling: Phys. Rev. B **12**, 3286 (1975)
206. C.H. Henry, D.V. Lang: Phys. Rev. B **15**, 989 (1977)
207. H. Sumi: Phys. Rev. B **27**, 2374 (1983)
208. A.M. Stoneham: Rep. Progr. Phys. **44**, 1251 (1981)
209. H. Sumi: Physica B & C **117-118**, 197 (1983)
210. H. Sumi: Phys. Rev. B **29**, 4616 (1984)
211. W. Wijaranakula: In *Defect Engineering in Semiconductor Growth, Processing and Device Technology*, ed. by S. Ashok, J. Chevallier, K. Sumino, E. Weber (Materials Research Society, Pittsburgh, PA 1992) p.561
212. E. Rotsaert, P. Clauws, E. Simoen, J. Vennik: Solid State Commun. **77**, 415 (1991)
213. J.J. van Kooten, G.A. Weller, C.A.J. Ammerlaan: Phys. Rev. B **30**, 4564 (1984)
214. W. Gehlhoff, K. Irmscher, J. Kreissl: In *New Developments in Semiconductor Physics* (Lecture Notes in Physics 301), ed. by G. Ferenczi, F. Beleznay (Springer-Verlag, Berlin 1988) p.262
215. K. Irmscher, T. Kind, W. Gehlhoff: Phys. Rev. B **49**, 7964 (1994)
216. W. Gehlhoff, K. Irmscher, U. Rehse: Mater. Sci. Forum **143-7**, 1233 (1994)
217. S. Greulich-Weber, A. Gorger, J.M. Spaeth, H. Overhof: Appl. Phys. A **53**, 147 (1991)
218. S. Greulich-Weber, A. Gorger, J.-M. Spaeth, H. Overhof: Mater. Sci. Forum **83-7**, 149 (1992)
219. K. Nakashima: Jpn. J. Appl. Phys. **24**, 785 (1985)
220. A. Chantre: Appl. Phys. Lett. **46**, 263 (1985)
221. P.A. Martin, B.G. Streetman, K. Hess: J. Appl. Phys. **52**, 7409 (1981)
222. H. Weihrich, H. Overhof: Mater. Sci. Forum **143-7**, 177 (1994)
223. W. Gehlhoff, K. Irmscher, U. Rehse: Mater. Sci. Forum **38-41**, 373 (1989)
224. W. Gehlhoff, U. Rehse: Solid State Phenom. **6-7**, 257 (1989)
225. A. Chantre, L.C. Kimerling: Mater. Sci. Forum **10-12**, 387 (1986)
226. W. Gehlhoff, P. Emanuelsson, P. Omling, H.G. Grimmeiss: Phys. Rev. B **41**, 8560 (1990)
227. W. Gehlhoff, P. Emanuelsson, P. Omling, H.G. Grimmeiss: Solid State Phenom. **19-20**, 207 (1991)
228. P. Omling, P. Emanuelsson, H.G. Grimmeiss: Mater. Sci. Forum **38-41**, 445 (1989)
229. P. Omling, P. Emanuelsson, W. Gehlhoff, H.G. Grimmeiss: Solid State Commun. **70**, 807 (1989)
230. W. Gehlhoff, P. Emanuelsson, P. Omling, H.G. Grimmeiss: Phys. Rev. B **47**, 7025 (1993)
231. P. Emanuelsson, W. Gehlhoff, P. Omling, H.G. Grimmeiss: In *Impurities, Defects and Diffusion in Semiconductors: Bulk and Layered Structures*, ed. by D.J. Wolford, J. Bernholc, E.E. Haller (Mater. Res. Soc., Pittsburgh, PA 1990) p.307
232. P. Emanuelsson, P. Omling, H.G. Grimmeiss, W. Gehlhoff, J. Kreissl, K. Irmscher, U. Rehse: Mater. Sci. Forum **83-7**, 137 (1992)
233. P. Tidlund, M. Kleverman, H.G. Grimmeiss: Semicond. Sci. Technol. **11**, 748 (1996)
234. M. Kleverman, P. Tidlund: Phys. Rev. B **56**, 15685 (1997)
235. P. Tidlund, M. Kleverman: Mater. Sci. Forum **258-263**, 455 (1997)
236. U. Reislohner, W. Witthuhn: Mater. Sci. Forum **65-6**, 281 (1990)
237. H.H. Rinneberg: Atomic Energy Rev. **17**, 477 (1979)
238. L.C. Kimerling, M.T. Asom, J.L. Benton, P.J. Drevinsky, C.E. Caefer: Mater. Sci. Forum **38-41**, 141 (1989)
239. C.A.J. Ammerlaan, T. Gregorkiewicz: In *New Developments in Semiconductor Physics* (Lecture Notes in Physics 301), ed. by G. Ferenczi, F. Beleznay (Springer-Verlag, Berlin 1988) p.244
240. M.A. Vouk, E.C. Lightowlers: J. Luminesc. **15**, 357 (1977)
241. M.L.W. Thewalt, U.O. Ziemelis, R.R. Parsons: Phys. Rev. B **24**, 3655 (1981)
242. M.L.W. Thewalt, U.O. Ziemelis, S.P. Watkins, R.R. Parsons: Can. J. Phys. **60**, 1691 (1982)
243. S.P. Watkins, M.L.W. Thewalt, T. Steiner: Phys. Rev. B **29**, 5727 (1984)
244. R. Sauer, J. Weber: Physica B **116**, 195 (1983)
245. S.P. Watkins, M.L.W. Thewalt: Can. J. Phys. **63**, 1074 (1985)
246. H. Conzelmann, A. Hangleiter, J. Weber: Phys. Status Solidi B **133**, 655 (1986)
247. M.L.W. Thewalt, U.O. Ziemelis, R.R. Parsons: Solid State Commun. **39**, 27 (1981)
248. T.E. Schlesinger, T.C. McGill: Phys. Rev. B **25**, 7850 (1982)
249. M. Suezawa, K. Sumino: In *Impurities, Defects and Diffusion in Semiconductors: Bulk and Layered Structures*, ed. by D.J. Wolford, J. Bernholc, E.E. Haller (Mat. Res. Soc., Pittsburgh, PA 1990) p.233
250. E.R. Weber: In *Impurity Diffusion and Gettering in Silicon*, ed. by R.B. Fair, C.W. Pearce, J. Washburn (Mater. Res. Soc., Pittsburghh, PA, USA 1985) p.3
251. J.R. Leite, L.V.C. Assali, V.M.S. Gomes: In *New Developments in Semiconductor Physics*, ed. by G. Ferenczi, F. Beleznay (Springer-Verlag, Berlin 1988) p.75
252. L.V.C. Assali, J.R. Leite: Phys. Rev. B **36**, 1296 (1987)
253. L.V.C. Assali, J.R. Leite: Mater. Sci. Forum **83-7**, 143 (1992)
254. L.V.C. Assali, J.R. Leite: Mater. Sci. Forum **10-12**, 55 (1986)
255. L.V.C. Assali, J.R. Leite: Int. J. Quantum Chem. **21**, 89 (1987)
256. L.V.C. Assali, J.R. Leite: Mater. Sci. Forum **38-41**, 409 (1989)
257. L.V.C. Assali, J.R. Leite: In Proc. of 20th International Conference on the Physics of Semiconductors, ed. by E.M. Anastassakis, J.D. Joannopoulos (Thessaloniki, Greece 1990) p.597
258. M. Sugimoto, A. Seki: Mater. Sci. Forum **196-201**, 1339 (1995)
259. H. Overhof, H. Weihrich: Phys. Rev. B **55**, 10508 (1997)
260. H. Weihrich, H. Overhof: Mater. Sci. Forum **196-201**, 1327 (1995)
261. H. Weihrich, H. Overhof: Semicond. Sci. Technol. **13**, 1374 (1998)
262. G.D. Watkins: Mater. Sci. Forum **38-41**, 39 (1989)
263. J.L. Benton: J. Electron. Mater. **18**, 199 (1989)
264. A. Chantre: In *Defects in Electronic Materials*, ed. by M. Stavola, S.J. Pearton, G. Davies (Mat. Res. Soc., Pittsburgh, PA 1988) p.37
265. M. Levinson: J. Appl. Phys. **58**, 2628 (1985)
266. J.A. Dean: *Lange's handbook of chemistry* (McGraw-Hill, Inc., New York 1992)
267. *CRC Handbook of Chemistry and Physics*, ed. by D.R. Lide (CRC Press, Boca Raton 1998)
268. S. Zhao, L.V.C. Assali, L.C. Kimerling: Mater. Sci. Forum **196-201**, 1333 (1995)
269. D. Lecrosnier, J. Paugam, G. Pelous, F. Richou, M. Salvi: J. Appl. Phys. **52**, 5090 (1981)
270. H. Takahashi, M. Suezawa, K. Sumino: J. Appl. Phys. **78**, 3077 (1995)
271. H. Takahashi, M. Suezawa, K. Sumino: Mater. Sci. Forum **143-7**, 1257 (1994)
272. Y.H. Lee, R.L. Kleinhenz, J.W. Corbett: Inst. Phys. Conf. Ser. **46**, 521 (1979)
273. M. Hohne, U. Juda, H. Riemann, J.M. Spaeth, S. Greulich-Weber: Phys. Rev. B **49**, 16999 (1994)
274. S.F. Cagnina: J. Electrochem. Soc. **116**, 498 (1969)

275. N.T. Bagraev, L.S. Vlasenko, Y.A. Karpov, V.M. Turovskii: Sov. Phys. Semicond. **17**, 175 (1983)
276. H. Zimmermann: Mater. Sci. Forum **143-147**, 1647 (1994)
277. H. Zimmermann, N.Q. Khanh, G. Battistig, J. Gyulai, H. Ryssel: Appl. Phys. Lett. **60**, 748 (1992)
278. R.L. Kleinhenz, Y.H. Lee, J.W. Corbett, E.G. Sieverts, S.H. Muller, C.A.J. Ammerlaan: Phys. Status Solidi B **108**, 363 (1981)
279. E.G. Sieverts, S.H. Muller, C.A.J. Ammerlaan, R.L. Kleinhenz, J.W. Corbett: Phys. Status Solidi B **109**, 83 (1982)
280. S.D. Brotherton, P. Bradley, A. Gill, E.R. Weber: J. Appl. Phys. **55**, 952 (1984)
281. S.D. Brotherton: J. Appl. Phys. **55**, 3636 (1984)
282. N.F. Will, K. Hofmann, M. Schulz: Appl. Phys. A **41**, 107 (1986)
283. E.R. Weber, N. Wiehl: In *Defects in Semiconductors II*, ed. by S. Mahajan, J.W. Corbett (North-Holland, New York 1983) p.19
284. H. Lemke: Phys. Status Solidi A **75**, 473 (1983)
285. L.V.C. Assali, J.R. Leite, A. Fazzio: Phys. Rev. B **32**, 8085 (1985)
286. L.V. Assali, J.F. Justo: Phys. Rev. B **58**, 3870 (1998)
287. H. Overhof, H. Weihrich: Mater. Sci. Forum **196-201**, 1357 (1995)
288. S.D. Brotherton, P. Bradley, A. Gill: J. Appl. Phys. **57**, 1783 (1985)
289. A.B. van Oosten, N.T. Son, L.S. Vlasenko, C.A.J. Ammerlaan: Mater. Sci. Forum **38-41**, 355 (1989)
290. E. Alves, J. Bollmann, M. Deicher, M.C. Carmo, M.O. Henry, M.H.A. Knopf, J.P. Leitao, R. Magerle, C.J. McDonagh: Mater. Sci. Forum **258-263**, 473 (1997)
291. R. Czaputa: Appl. Phys. A **49**, 431 (1989)
292. R. Czaputa, M. Midl, H. Feichtinger, A. Bauer: Mater. Sci. Forum **38-41**, 415 (1989)
293. M. Hohne, U. Juda: Mater. Sci. Technol. **11**, 680 (1995)
294. M. Hohne, U. Juda: J. Appl. Phys. **72**, 3095 (1992)
295. H. Lemke: Phys. Status Solidi A **72**, 177 (1982)
296. G.W. Ludwig: Phys. Rev. **137**, A1520 (1965)
297. O.F. Schirmer: Physica B & C **116**, 306 (1983)
298. B. Hackl, K.J. Range, L. Fabry, P. Stallhofer: J. Electrochem. Soc. **139**, 3250 (1992)
299. X. Zhang, D. Yang, R. Fan, J. Zhang, D. Que: J. Appl. Phys. **84**, 5502 (1998)
300. B. Shen, J. Jablonski, T. Sekiguchi, K. Sumino: Jpn. J. Appl. Phys. **35**, 4187 (1996)
301. J. Jablonski, B. Shen, T.R. McHedlidze, M. Imai, K. Sumino: Mater. Sci. Forum **196-201**, 1859 (1995)
302. M. Hourai, K. Murakami, T. Shigematsu, N. Fujino, T. Shiraiwa: Jpn. J. Appl. Phys. **28**, 2413 (1989)
303. S. Sadamitsu, A. Sasaki, M. Hourai, S. Sumita, N. Fujino: Jpn. J. Appl. Phys. **30**, 1591 (1991)
304. Z. You, M. Gong, Y. Chen, J.W. Corbett: J. Appl. Phys. **63**, 324 (1988)
305. G.D. Watkins, J.W. Corbett: Phys. Rev. **121**, 1001 (1961)
306. J.W. Corbett, G.D. Watkins, R.M. Chrenko, R.S. McDonald: Phys. Rev. **121**, 1015 (1961)
307. L.C. Kimerling: In *International Conference on Radiation Effects in Semiconductors*, ed. by N.B. Urli, J.W. Corbett (IOP, London 1977) p. 221
308. V.E. Kustov, Y.N. Bagrin, N.A. Tripachko, V.I. Shakhovtsov, L.I. Spinar: Phys. Status Solidi A **129**, 337 (1992)
309. T. Mchedlidze, K. Matsumoto: J. Appl. Phys. **83**, 4042 (1998)
310. S.J. Pearton, J.W. Corbett, T.S. Shi: Appl. Phys. A **43**, 153 (1987)
311. J. Meier, S. Dubail, R. Platz, P. Torres, U. Kroll, J.A.A. Selvan, N.P. Vaucher, C. Hof, D. Fischer, H. Keppner, R. Flueckiger, A. Shah, V. Shklover, K.D. Ufert: Solar Energy Mater. Solar Cells **49**, 35 (1997)
312. R. Plieninger, H.N. Wanka, J. Kuhnle, J.H. Werner: Appl. Phys. Lett. **71**, 2169 (1997)
313. O.V. Feklisova, N.A. YarykIn: Semicond. Sci. Technol. **12**, 742 (1997)
314. Y. Tokuda: Jpn. J. Appl. Phys. **37**, 1815 (1998)
315. J.U. Sachse, E.O. Sveinbjornsson, W. Jest, J. Weber, H. Lemke: Phys. Rev. B **55**, 16176 (1997)
316. W. Jost, J. Weber: Phys. Rev. B **54**, R11038 (1996)
317. N. Yarykin, J.U. Sachse, J. Weber, H. Lemke: Mater. Sci. Forum **258-263**, 301 (1997)
318. W. Jost, J. Weber, H. Lemke: Semicond. Sci. Technol. **11**, 525 (1996)
319. S.J. Pearton, A.J. Tavendale: J. Phys. C **17**, 6701 (1984)
320. J. Weber: (1998) private communications
321. M. Kouketsu, S. Isomae: J. Appl. Phys. **80**, 1485 (1996)
322. M. Kouketsu, K. Watanabe, S. Isomae: Mater. Sci. Forum **196-201**, 861 (1995)
323. E.B. Yakimov, A.L. Parakhonsky: Solid State Phenom. **57-58**, 383 (1997)
324. M. Kaniewska, J. Kaniewski, L. Ornoch, T. Sekiguchi, K. Sumino: Mater. Sci. Forum **258-63**, 325 (1997)
325. T. Sadoh, A.K. Tsukamoto, A. Baba, D. Bai, A. Kenjo, T. Tsurushima, H. Mori, H. Nakashima: J. Appl. Phys. **82**, 3828 (1997)
326. J.J. van Kooten, E.G. Sieverts, C.A.J. Ammerlaan: Solid State Commun. **64**, 1489 (1987)
327. G.W. Ludwig, H.H. Woodbury, R.O. Carlson: Phys. Chem. Solids **8**, 490 (1959)
328. A.A. Ezhevskii, C.A.J. Ammerlaan: Sov. Phys. Semicond. **24**, 851 (1990)
329. A.A. Ezhevskii, N.T. Son, C.A.J. Ammerlaan: Solid State Commun. **81**, 955 (1992)
330. H.G. Riotte, U. Herpers, E.R. Weber: Radiochim. Radioanal. Lett. **30**, 311 (1977)
331. P.F. Schmidt, C.W. Pearce: J. Electrochem. Soc. **128**, 630 (1981)
332. P.F. Schmidt: Solid State Technol. **26**, 147 (1983)
333. G. Borchardt, E. Weber, N. Wiehl: J. Appl. Phys. **52**, 1603 (1981)
334. M. Stojic: Fizika **15**, 353 (1983)
335. C. Schmidt: Appl. Phys. **17**, 137 (1978)
336. A.O. Evwaraye: Inst. Phys. Conf. Ser. **46**, 533 (1979)
337. M. Singh, W.M. Chen, N.T. Son, B. Monemar, E. Janzen: Solid State Commun. **93**, 415 (1995)
338. M.C. do Carmo, M.I. Calao, G. Davies, E.C. Lightowlers: Mater. Sci. Forum **38-41**, 421 (1989)
339. M.I. Calao, M.C. do Carmo: Physica Scr. **38**, 455 (1988)
340. T.E. Schlesinger, R.J. Hauenstein, R.M. Feenstra, T.C. McGill: Solid State Commun. **46**, 321 (1983)
341. H.D. Mohring, J. Weber, R. Sauer: Phys. Rev. B **30**, 894 (1984)
342. T.E. Schlesinger, T.C. McGill: Phys. Rev. B **28**, 3643 (1983)
343. J. Kluge, W. Gehlhoff, J. Donecker: Acta Phys. Pol. A **73**, 207 (1988)
344. M.O. Henry, E. Alves, J. Bollmann, A. Burchard, M. Deicher, M. Fanciulli, D. Forkel-Wirth, M.H. Knopf, S. Lindner, R. Magerle, E. McGlynn, K.G. McGuigan, J.C. Soares, A. Stotzler, G. Weyer: Phys. Status Solidi B **210**, 853 (1998)
345. G.S. Mitchard, S.A. Lyon, K.R. Elliott, T.C. McGill: Solid State Commun. **29**, 425 (1979)
346. D.H. Brown, S.R. Smith: J. Luminesc. **21**, 329 (1980)
347. J. Weber, R. Sauer, P. Wagner: J. Luminesc. **24&25**, 155 (1981)
348. R.E. Stahlbush, R.A. Forman: J. Luminesc. **26**, 227 (1982)
349. A. Ourmazd: In Proc. of Int. Conf. Electrical Properties of Dislocations in Semiconductors (France 1984) p.315
350. A.G. Shaikh, W. Schroter, W. Bergholz: J. Appl. Phys. **58**, 2519 (1985)
351. R. Falster: Appl. Phys. Lett. **46**, 737 (1985)
352. W. Schroter, R. Kuhnapfel: Appl. Phys. Lett. **56**, 2207 (1990)
353. E. Spiecker, M. Seibt, W. Schroter: Phys. Rev. B **55**, 9577 (1997)
354. S.V. Joshi, M.C. Joshi: Phys. Status Solidi A **64**, K7 (1981)
355. O. Kumagai, K. Kaneko: J. Appl. Phys. **51**, 5430 (1980)
356. L. Bischoff, T. Gessner, H. Morgenstern: Phys. Status Solidi A **70**, K35 (1982)
357. O. Kumagai, K. Kaneko: J. Appl. Phys. **52**, 5143 (1981)
358. A.A. Zolotukhin, L.S. Milevskii, I. L. Smol'skii, Y.A. Sidorov: Sov. Phys. Semicond. **6**, 1679 (1973)
359. W. Fahrner, A. Goetzberger: Appl. Phys. Lett. **21**, 329 (1972)
360. M.A. Abdugafurova, L.M. Kapitonova, L.S. Kostina, A.A. Lebedev, S. Makhkamov: Sov. Phys. Semicond. **9**, 450 (1975)
361. A.I. Dyatlov, L.M. Kapitonova, A.A. Lebedev, M.A. Pogarskii, T.A. Shaposhnikova: Sov. Phys. Semicond. **11**, 559 (1977)
362. S. Tanaka, H. Kitagawa: Jpn. J. Appl. Phys. (Letters) **34**, L721 (1995)
363. H. Kitagawa, S. Tanaka, B. Ni: Jpn. J. Appl. Phys. (Letters) **32**, L1645 (1993)
364. H. Kitagawa, L.C. Kimerling, S. Tanaka: J. Electron. Mater. **21**, 863 (1992)
365. H. Kitagawa, S. Tanaka: In *Defect and Impurity Engineered Semiconductors and Devices*, ed. by S. Ashok, J. Chevallier, I. Akasaki, N.M. Johnson, B.L. Sopori (Mat. Res. Soc., Pittsburgh, PA 1995) p.983
366. S. Tanaka, H. Kitagawa: Jpn. J. Appl. Phys. (Letters) **37**, L4 (1998)
367. S. Tanaka, H. Kitagawa: Jpn. J. Appl. Phys. **37**, 4656 (1998)
368. A. Mesli, T. Heiser, N. Amroun, P. Siffert: Appl. Phys. Lett. **57**, 1898 (1990)
369. P. Blood, J.W. Orton: *The Electrical Characterization of Semiconductors: Majority Carriers and Electron States* (Academic press, London 1992)

Purity

Dopants in deposited copper in *ppm* depending on bath age measured after 2000 wafers throughput

Element	0 wafers/liter	50 wafers/liter	100 wafers/liter
H	1.183	1.183	1.183
S	0.095	0.047	0.071
C	0.828	0.710	0.710
N	7.101	8.284	9.467
O	2.367	2.367	2.367
Cl	0.178	0.118	0.071
P	0.095	0.107	0.095
Total	16.69	17.67	18.82

Fe, Sb,K,Li,Na,Ca,Ni, Ti,Pb,Cr are below the detection limit